Muon Studies of Low-Dimensional Solid State Systems

Thomas Jestädt
St. John's College

A thesis submitted for the degree of
Doctor of Philosophy
at the
University of Oxford
April 1999

Muon Studies of Low-Dimensional Solid State Systems

Thomas Jestädt
St. John's College, Oxford University
Trinity Term 1999

Abstract of Thesis Submitted for the Degree of Doctor of Philosophy

This thesis concerns the use of the technique of μSR, an abbreviation which stands for three separate types of experiments: muon spin rotation, muon spin relaxation and muon spin resonance. The experiments presented here were performed on beamlines at the ISIS facility at the Rutherford Appleton Laboratory (U.K.) and at the Paul Scherrer Institut (Villigen, Switzerland). The systems studied are linked by the common theme of reduced dimensionality.

Results of μSR measurements on $La_{2-x}Sr_xNiO_{4+\delta}$ (nickelates) are presented. In these systems the lattice constants are much smaller in two of the dimensions as compared to the third, leading to two dimensional magnetism. Earlier experiments using techniques other than μSR concentrated mainly on materials with $x = 0$ and $\delta \neq 0$. The work that I describe on $La_{2-x}Sr_xNiO_{4+\delta}$ shows that there are interesting magnetic features as a function of strontium doping, and the details of this dependence are examined. In each of the samples oscillations of the muon spin polarization were observed below a sample dependent temperature, showing that low temperature magnetic order occurs.

μSR is also used to study $Sr_2LnMn_2O_7$ (the Ruddlesden-Popper phases), where Ln are various ions of the lanthanide series. These manganates have a layered structure, leading to a reduced dimensionality as compared to the related perovskite compounds of the MnO_3 series. Like the doped MnO_3 compounds, some of the Ruddlesden-Popper phases exhibit colossal magnetoresistance (CMR), an effect which initially stirred interest in the MnO_3 systems. In contrast to the MnO_3 systems, the relevant Mn_2O_7 materials show this CMR effect over an extended temperature range. The μSR work is consistent with the existence of magnetic clusters in some of the Mn_2O_7 materials and these clusters appear to be associated with the observation of CMR.

The compound CaV_4O_9 is the first known two-dimensional compound to exhibit a spin-gap and the effects of this spin-gap on the magnetic properties are investigated here.

I also describe results of measurements on a material with even more reduced dimensionality, polybutadiene (PB). This is a non-conducting polymer without side-chains. Muons in this system can either be in a paramagnetic or a diamagnetic state (with a polymer radical state produced by reaction of muonium with a polymer bond). The nature of these states has been examined with a variety of μSR techniques, and the influence of the polymer dynamics and the glass transition in PB is discussed.

For Ortrud, Willi, Heike and Sepp

Die Welt ist alles, was der Fall ist.
Wittgenstein

"So it does!" said Pooh. "It goes in!"
Winnie-the-Pooh

Acknowledgements

I am greatly indebted to the following people and institutions, and I wish to thank them:

- Bill Hayes for his thoughtful advice and guidance as supervisor of this thesis and Steve Cox, my external supervisor, for his help and for sharing his wisdom with me.
- Steve Blundell, for his proof-reading and proof-thinking, many discussions, invaluable help and also for the friendly atmosphere in the group that is due to him.
- Francis Pratt, who has greatly contributed to this thesis and has always been a reliable source of information. John Singleton was helpful and encouraging.
- Kim Chow, for constant support, proof-reading, an abundance of suggestions and help, and his friendship.
- Holger Kaufmann, for his friendship over so many years.
- St. John's College, which was my home for more than 3 years, for financially supporting conference attendances and the purchase of books.
- Philip King for help with the preparation of some of the figures and, together with Steve Cottrell and Chris Scott, for technical assistance at ISIS. Alex Amato, Chris Baines, Ivan Reid and Uli Zimmermann for technical assistance at PSI. Phil Wiseman and Simon Carling, for technical assistance with the magnetization measurements at the ICL, Oxford, and at the Royal Institution. I had many enjoyful conversations with Mo Kurmoo about organic and molecular materials and their magnetic properties. Donald Arseneau gave me expert advice on LaTeX.
- The guys in the group: Arzhang Ardavan, Rob Bewley, Ann-Katrin Klehe, Anke Husmann (with special thanks for her proof-reading), Brendon Lovett, Ishbel Marshall, Johannes Stiessberger and all the others. It was great working with them.
- My parents, Willi and Ortrud, and Heike and Sepp, to whom this work is dedicated.

I would like to add those friends whom I have not mentioned so far and who have supported me in many different ways during my project. I would like to thank: Girgl Eska, for moral support, Helmut Fink, the driving force behind the "Erlangen Circle", Bernhard Fulda, for this and that, Bärbel Hacker, for her friendship, Uli Hillenbrand (I have to admit that I envy his distinct humour), Helga Knauer for her special way of helping me through life, Markus Laimer, just do it!, Sabine Matthäus, who will prove that career *and* a family life are possible, Barbara Navé, for constant encouragement, Matthew Robinson, who will give Shostakovich another chance (some time), Andreas Strobel, for 10 years of friendship, Chris Waigl, who showed me that one can do the right things, and Birgit Welker, for phone calls at the right time.

I add with special affection Renela, for her love, care and tenderness over three years, for letting me be her sous-chef, and for loads of gweat adventures and twaditions.

I am indebted to EPSRC and the Rutherford Appleton Laboratory for financial support during part of my research studies, and the European Union, which has provided me with a Marie-Curie-Fellowship. The Siemens International Doctorate Programme has given me long-standing material and non-material support.

Table of Symbols & Abbreviations

A, A_μ	hyperfine tensor or constant
A_μ^{iso}	isotropic component of hyperfine tensor or constant
AFM	antiferromagnet(ic)
B_0	magnetic field characteristic for A_μ, $B_0 = A_\mu/(\gamma_e + \gamma_\mu)$
CMR	colossal magnetoresistance
D_μ	anisotropic part of hyperfine tensor
$D_\mu^{\parallel}$, $D_\mu^{\perp}$	principal values of anisotropic part of hyperfine tensor for axial symmetric case
dKT	dynamic Kubo-Toyabe (function)
FM	ferromagnet(ic)
γ_e	electron gyromagnetic ratio = $2\pi \times 2.799248 \times 10^{10}$ Hz/T
γ_μ	muon gyromagnetic ratio = $2\pi \times 1.355 \times 10^{8}$ Hz/T
γ_p	proton gyromagnetic ratio = $2\pi \times 0.4258 \times 10^{8}$ Hz/T
$\mathbf{I}$ ($\mathbf{I}^k$)	electron (nuclear) spin-operator
k_B	Boltzmann constant
LF	longitudinal (magnetic) field
LF-sKT	longitudinal field static Kubo-Toyabe (function)
m_μ	mass of the muon (≈ 105.66 MeV/c^2)
μ^+ (μ^-)	positive (negative) muon
μ_N	nuclear magnetic unit = 5.0508×10^{-27} J/T
NMR	Nuclear Magnetic Resonance
RK	"Risch-Kehr", see section 6.5, page 118
$\lvert\mathbf{S}_\mu\rvert$	muon spin = $\hbar/2$
$\mathbf{S}_\mu, \mathbf{S}$	muon spin operator
TF	transverse (magnetic) field
WLF	Williams-Landel-Ferry (law), see Equation 6.19 on page 123
ZF	zero (magnetic) field
ZF-sKT	zero field static Kubo-Toyabe (function)

Contents

List of Figures

Chapter 1

Introduction

Contents

1.1 Introductory remarks

The discovery of the parity violation of the muon decay [Garw57] in 1957 gave rise to a wealth of experiments with muons. The decay products of muons which were brought to rest in some target material were studied and the interaction of this target with the muon was seen as an annoying but unavoidable effect. However, in the course of these studies it became clear that muons in matter can be used as a good spectroscopic probe to elucidate magnetic and dynamic interactions in the target material.

This thesis concerns the use of the technique of μSR, an abbreviation which stands for three separate types of experiments: muon spin rotation, muon spin relaxation and muon spin resonance. The technique has been applied to a variety of problems [Sche85, Cox87, Blun99], including:

- **Muons in semiconductors**: The behaviour of the muons in semiconductors is of great interest. Muons can pick up electrons, thus forming muonium (μ^+e^-), which can be considered as a light isotope of the hydrogen atom. These muonium states [Patt88] can be of interest since one can draw conclusions about the behaviour of hydrogen in semiconductors.

- **Superconductivity**: μSR has been used to study the behaviour of flux lines in type-II superconductors [Uemu88, Aege97]. In these experiments, the relaxation of a transverse field oscillatory muon spin signal is measured as a function of temperature, and the results can be linked to the flux lattice and the penetration depth in these materials [Uemu85].

- **Muon chemistry**: The chemistry of the muon (or muonium) has been the subject of very much interest. For example, muon addition to organic materials can lead to the existence of a radical electron, which itself can interact with the muon(ium). The form of the final state is hard to predict from first principles, and experiments have been performed on a variety of materials [Rodu93].

- **Magnetism**: One of the main avenues in muon spin research is the use of the muon as a magnetic test particle. Muons can detect very small magnetic fields and magnetic moments (e.g. 10^3 times smaller than electronic magnetic moments). As a local probe of magnetism it can be a hyperfine

method related to Nuclear Magnetic Resonance (NMR), Perturbed Angular Correlation (PAC) and Mössbauer spectroscopy. The study of magnetic phase transitions has become an important field in muon spin research in recent years [Sche95]. Some of the results presented here are devoted to this area of μSR.

Muon experiments have to be performed at muon beamlines, which are part of large-scale research facilities. Often muons are just a "by-product" of the production of neutrons. This also means that these experiments have to be well-planned, since beam time on these facilities is limited and expensive. The experiments presented here were performed on beamlines at the ISIS facility at the Rutherford Appleton Laboratory (U.K.) and at the Paul Scherrer Institut (Villigen, Switzerland).

1.2 Plan of the thesis

The systems studied in this thesis are linked by the common theme of reduced dimensionality. In the oxides of Chapters 3, 4 and 5 the crystal structure and dimensions of the systems are such that two dimensional effects are important. Polymers like polybutadiene (Chapter 6) are one-dimensional. In addition to that, the systems studied show or are related to interesting physical properties: the nickelates of Chapter 3 exhibit two-dimensional magnetism and stripe ordering, and are isostructural to the superconducting cuprates. The manganates show colossal magnetoresistance, and CaV_4O_9 is a two-dimensional spin-gap system. Polybutadiene possesses a glass-transition and can be related to conducting polymers. In the following I briefly describe the contents of each chapter.

In Chapter 2, I introduce some basic features of muons and μSR with special emphasis on the tools used in later chapters. I do not elaborate on μSR methods in fields not covered in this thesis.

In Chapter 3, I present results of μSR measurements on $La_{2-x}Sr_xNiO_{4+\delta}$ (nickelates). In these systems the lattice constants are much smaller in two of the dimensions as compared to the third, leading to two dimensional magnetism. The nickelates have stirred interest recently because of the discovery of a "stripe" structure. However, earlier experiments using techniques other than μSR concentrated mainly on materials with $x = 0$ and $\delta \neq 0$. The work that I describe on

$La_{2-x}Sr_xNiO_{4+\delta}$ shows that there are interesting magnetic features as a function of strontium doping, and the details of this dependence is the topic of Chapter 3. In each of the samples oscillations of the muon spin polarization were observed below a sample dependent temperature, showing that low temperature magnetic order occurs in these systems.

Chapter 4 describes results of a study on $Sr_2LnMn_2O_7$ (the Ruddlesden-Popper phases), where Ln are various ions of the lanthanide series. These manganates have a layered structure, leading to a reduced dimensionality as compared to the related compounds of the MnO_3 series. Like the MnO_3 compounds, some of the Ruddlesden-Popper phases exhibit colossal magnetoresistance (CMR), an effect which initially stirred interest in the MnO_3 systems. In contrast to the MnO_3 systems, the relevant Mn_2O_7 materials show this CMR effect over an extended temperature range. The μSR work (also neutron and magnetization measurements by others) is consistent with the existence of magnetic clusters in some of the Mn_2O_7 materials and these clusters appear to be associated with the observation of CMR.

Chapter 5 is dedicated to the compound CaV_4O_9. This system has, again, a two-dimensional structure. It is the first known two-dimensional compound to exhibit a spin-gap and the effects of this spin-gap on the magnetic properties are investigated here.

In the chapters presented so far we have looked at oxides, all of which have a low-dimensional character. In the following Chapter 6, I describe results of measurements on a material with even more reduced dimensionality, polybutadiene (PB). This is a one-dimensional non-conducting polymer without side-chains. When muons enter this system, they form muonium (μ^+e^-), which is added to the polymer chain. This can produce paramagnetic muons or diamagnetic muons (with a polymer radical state produced by reaction of muonium with a polymer bond). The nature of these states has been examined with a variety of μSR techniques, and the influence of the polymer dynamics and the glass transition in PB is discussed. These results are also interesting in the context of previous studies on conducting polymers, where the radical was free to move in the polymer chain. In order to correctly interpret the results, I also give a short introduction to those aspects of μSR in polymers and organic molecules which are relevant for the understanding of the experiments. In particular I introduce the concept of avoided level crossing (ALC) resonance experiments and transverse field experiments on

radicals.

1.3 General comments

Vectors are usually printed in boldface ($\mathbf{a}$), operators, tensors and scalars are printed in normal fonts (a). I do not always discriminate between a function and its value at a certain point (e.g. $f(x)$).

For the analysis of some of the muon data as well as for some non-muon data I used commercially available computer programs and programs written in the Oxford Muon Group. For the analysis of most of the muon data, I used the WiMDA program by Francis Pratt [Prat98]. Some of the muon data were fitted with several programs by or based on other programs by Steve Blundell.

There is a list of symbols and abbreviations at the beginning, and an index at the end of this thesis.

Chapter 2

The method: μSR

Contents

The aim of this chapter is to give an introduction to those aspects of μSR that are needed for the work described in this thesis.

The abbreviation μSR stands for muon spin rotation, relaxation, resonance, or more generally, for muon spin research. It is a method for the investigation of, for example, the structure and dynamics of magnetism in condensed matter.

In μSR experiments spin polarized muons are implanted in a sample and the effect of the local environment is observed: the muon is used as a probe for the investigation of magnetic and hyperfine fields in the sample. Information on the local magnetic field is obtained by studying the precession frequency of the spin-polarization of the muons, whereas the observed relaxation of the muon ensemble polarization gives information about the spatial and temporal variations of the internal fields (such as field distributions, fluctuation of fields etc.).

Muons and their properties, especially in the context of muon production for μSR, are discussed in 2.1. In the following section 2.2 I give information on the two possible kinds of muon sources: continuous and pulsed sources. In section 2.3 I describe how muons interact with matter. In particular I describe the muon implantation process, possible muon sites, and the aspect most relevant to this work: the muon spin interaction with the host. In the last section 2.4, details of the spectroscopic method(s) are introduced. For further details see [Chap84, Cox87, Sche85, Sche95, Smil94, deRe97].

2.1 Muons

2.1.1 Properties

Muons are charged leptons of the second family of elementary particles (in the picture of the currently widely used "standard model"). According to this classification they could be called the bigger brother(s) of the electron and positron. Some physical properties of muons are given in Table 2.1. The essential features for μSR are: a) the lifetime of 2.2 μs, which is relatively long, especially when compared with typical condensed matter processes, and b) the sizeable gyromagnetic ratio, which determines the interaction between the muon spin and the magnetic fields at the muon site.

Mass m_μ	105.6584389(34) MeV/c^2
	$= 206.7682\ m_\mathrm{e}$
	$\approx 1/9\ m_p$
Charge	$\pm e$
Spin $\lvert\mathbf{S}_\mu\rvert$	$\hbar/2$
Lifetime τ_μ	2.19703(4) μs
Gyromagnetic ratio γ_μ	$2\pi\times1.355\times10^8$ Hz/T

Table 2.1: Muon Properties, taken from [Part96]. m_e and m_p are the masses of the electron and proton, respectively.

2.1.2 Muon Production, Kinematics and Spin Polarization

Muon production occurs in several stages. For a schematic representation of the production and use of muons, see Figure 2.1. For an outline of a real muon facility, see Figure 2.2. In muon facilities like ISIS (at the Rutherford Appleton Laboratory, U.K.) or PSI (Paul Scherrer Institut, Switzerland), pions are produced in proton collisions. Accelerated protons with energies around 590 MeV (PSI) or 800 MeV (ISIS) hit a target such as graphite or beryllium to produce pions in the processes

$$p + n \longrightarrow n + n + \pi^+, \tag{2.1}$$

$$p + p \longrightarrow p + n + \pi^+, \quad \text{and} \tag{2.2}$$

$$p + n \longrightarrow p + p + \pi^-. \tag{2.3}$$

Since *positive* muons are the dominant species used in μSR, I concentrate in the following on *positive* pions, which produce them. Pions have a lifetime of $\tau_\pi = 26.03$ ns and a spin of zero. Spin-polarized positive muons are produced in the pion decay

$$\pi^+ \overset{\tau_\pi=26\mathrm{ns}}{\longrightarrow} \mu^+ + \nu_\mu. \tag{2.4}$$

(Other pion decay channels are negligible at the 10^{-4} level.) The two-body decay of the pion (mass $m_{\pi^+} = 139.5679$ MeV/c^2) into a muon ($m_\mu = 105.66$ MeV/c^2) and a neutrino (negligible mass) results in the muon having a unique momentum in the pion rest-frame. It is $p_\mu = 29.7877$ MeV/c, and the corresponding energy

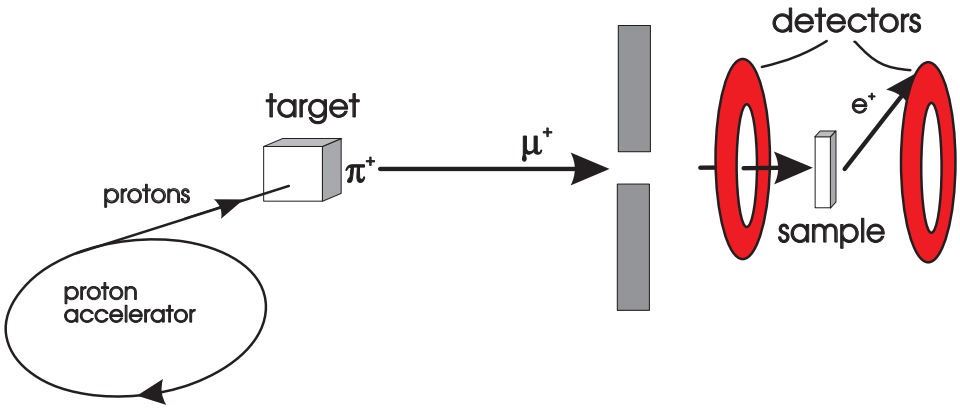

Figure 2.1: Production and use of "surface" muons: protons are accelerated and they hit a target to produce pions. Pions which come to rest close to the surface of the target decay into muons, which are being focused on the sample. When the muon(s) enter the sample the clock starts, and when the decay positrons are detected in the scintillation detectors the clock stops.

is 4.2 MeV/c^2. There are two different ways in use to obtain muon beams:

- A fraction of the pions come to rest at the surface of the proton target and muons emitted from these pions are used for the muon beam ("surface muons"). (It is not possible to produce surface beams of negative muons, since negative pions at rest will be captured by the target nuclei. This then induces a nuclear reaction with the pion without muon formation.)

- In some cases one uses beamlines that make use of pions which decay in flight and therefore produce muons of higher energy.

The muon neutrino ν_μ (see Equation 2.4) has negative helicity, i.e. its spin is antiparallel to its momentum in the pion restframe. Hence, to conserve angular momentum, the muon spin is also antiparallel to its momentum, see Figure 2.3. Thus, in the pion rest frame the produced muons are 100% spin polarized. The polarized muons are transported to the sample through a combination of dipole steering magnets and quadrupole focusing magnets. Wien filters, which consist of a combination of electric and magnetic fields, are used for a momentum/mass selection of the particles in order to eliminate contaminating positrons in the beam [Eato98].

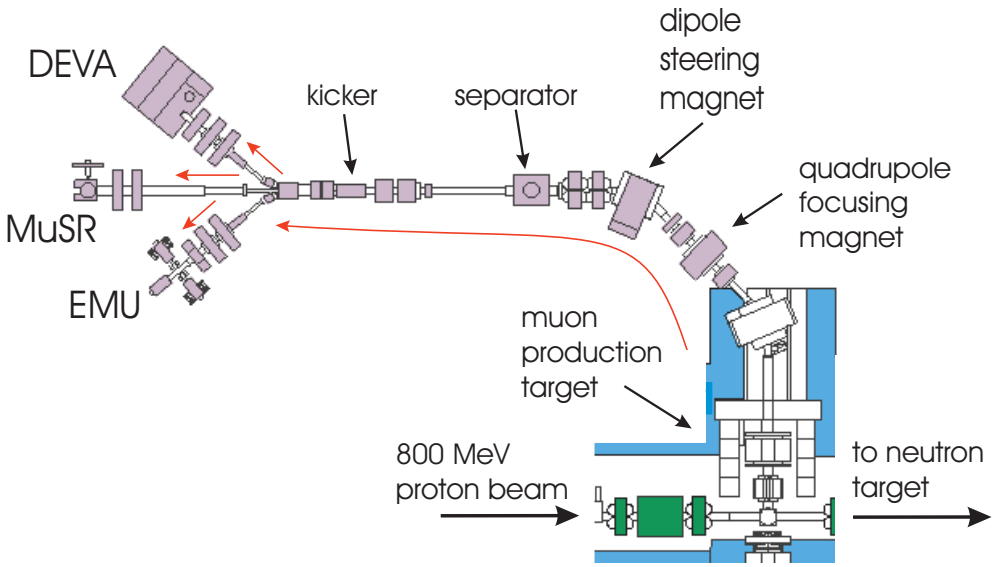

Figure 2.2: Schematic outline of the ISIS beamline(s): The "separator" removes contaminating particles (see text) and the "kicker" feeds muons to the three instruments DEVA, MuSR and EMU. (The majority of the figure is by courtesy of ISIS.)

By the direction of the muon spin we mean, in most cases, the ensemble average of the muon spin direction. The meaning should usually be clear from the context.

2.1.3 Muon Decay

The muons decay via the weak interaction at a time t after implantation in a sample with probability $1/\tau_\mu \times e^{-t/\tau_\mu}$, where the lifetime $\tau_\mu = 2.197$ μs (see Table 2.1). The dominant process is the decay into one positron and two neutrinos (see Table 2.2). Since the muon decay is a three body decay the positrons have an energy distribution. The energy of the emitted positron can vary continuously from zero (when the two neutrinos carry away all the kinetic energy) to the maximum positron energy of $E_{max} = 52.8$ MeV (when the two neutrinos are emitted antiparallel to the muon), the average energy is 36 MeV.

The decay is anisotropic: the positron e^+ is emitted preferentially in the direction of the muon spin. The decay probability of the muon can be calculated from the electroweak theory, which involves parity violating interactions. The probability per unit time for positron emission at an angle θ to the muon spin is

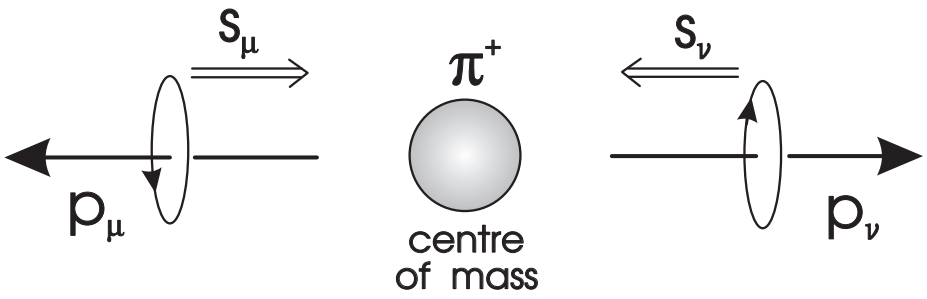

Figure 2.3: Decay of the pion: the muon neutrino ν_μ (right hand side) has a negative helicity in the pion rest frame. Because of conservation of angular momentum, the muon will also have its spin S_μ antiparallel to its momentum.

μ^+ decay mode	Fraction
$e^+\overline{\nu}_e\nu_\mu$	$\approx$99%
$e^+\overline{\nu}_e\nu_\mu\gamma$	1.4(4)%
$e^+\overline{\nu}_e\nu_\mu e^+e^-$	0.0034(4)%

Table 2.2: μ^+ decay modes, taken from [Part96]. μ^- modes are charge conjugates of the modes given.

given by

$$dW(\epsilon,\theta) = d\epsilon\; d\cos\theta\; \frac{n(\epsilon)}{\tau_\mu}\; \{1 + a(\epsilon)\cos(\theta)\}\,. \tag{2.5}$$

Here ϵ is the normalised positron energy E/E_{max}, $a(\epsilon) = (2\epsilon - 1)/(3 - 2\epsilon)$ is the asymmetry factor and $n(\epsilon) = \epsilon^2(3 - 2\epsilon)$. The expression in the brackets in Equation 2.5 is visualised in Figure 2.4 a) for various values of the normalized positron energy ϵ. The asymmetry factor $a(\epsilon)$ is particularly large for high positron energies (ϵ close to 1), see Figure 2.4 b). For $\epsilon = 1$, positrons are emitted preferentially in the direction of the muon spin and no positrons are emitted antiparallel, whereas for low energies there is a preference for positrons being emitted antiparallel to the muon spin. Averaging over all positron energies (i.e. integrating from $\epsilon = 0$

to $\epsilon = 1$) gives

$$dW(\theta) = d\cos\theta \, \frac{1}{2\tau_\mu} \, \{1 + a_0 \cos(\theta)\} \, , \quad a_0 = \frac{1}{3} \, . \tag{2.6}$$

This relation is depicted in Figure 2.4 a) as the thick line. It should be noted that the fact that the positrons are emitted anisotropically, with preference in the muon spin direction, is the underlying physical reason why muon spin research is possible. The positron emission probability distribution precesses with the muon spin. Hence recording of the positron intensity at a defined angle gives information about the precession of the spin. The time dependence of the positron emission direction is detected with scintillation detectors surrounding the sample environment. Low energy positrons are usually excluded in a practical μSR setup, and this leads to an improved anisotropy. However, since muon beams are usually not completely spin polarized and since there are other influences (like limited solid angle of the detectors) a typical experimental value of a_0 is about 0.25.

2.2 Muon Facilities

There are two distinct methods used to produce muons, resulting in continuous and pulsed muon beams. The two types of muon sources allow for complementary measurements. While the pulsed sources are best suited for slow relaxation processes and for the observation of relevant features at longer times, the continuous sources are best for determination of fast muon spin rotation frequencies or relaxations. This is explained in more detail in the following two subsections. In the work reported in this thesis use was made of both types of beamlines.

2.2.1 Pulsed Sources: ISIS

In pulsed sources, like ISIS, proton pulses from a synchrotron are fired at the proton target at regular intervals (typically 50 Hz), see Figure 2.5. Consequently, the resulting muons are also pulsed, at the same frequency. However, since a) the proton pulse has a finite width and b) the pions have a finite decay time (see above), the muon pulse has a finite width as well. When the pulse of muons is implanted in the sample, a detector starts a clock, and the time until decay positrons are detected is stored in a histogram format. A typical order of mag-

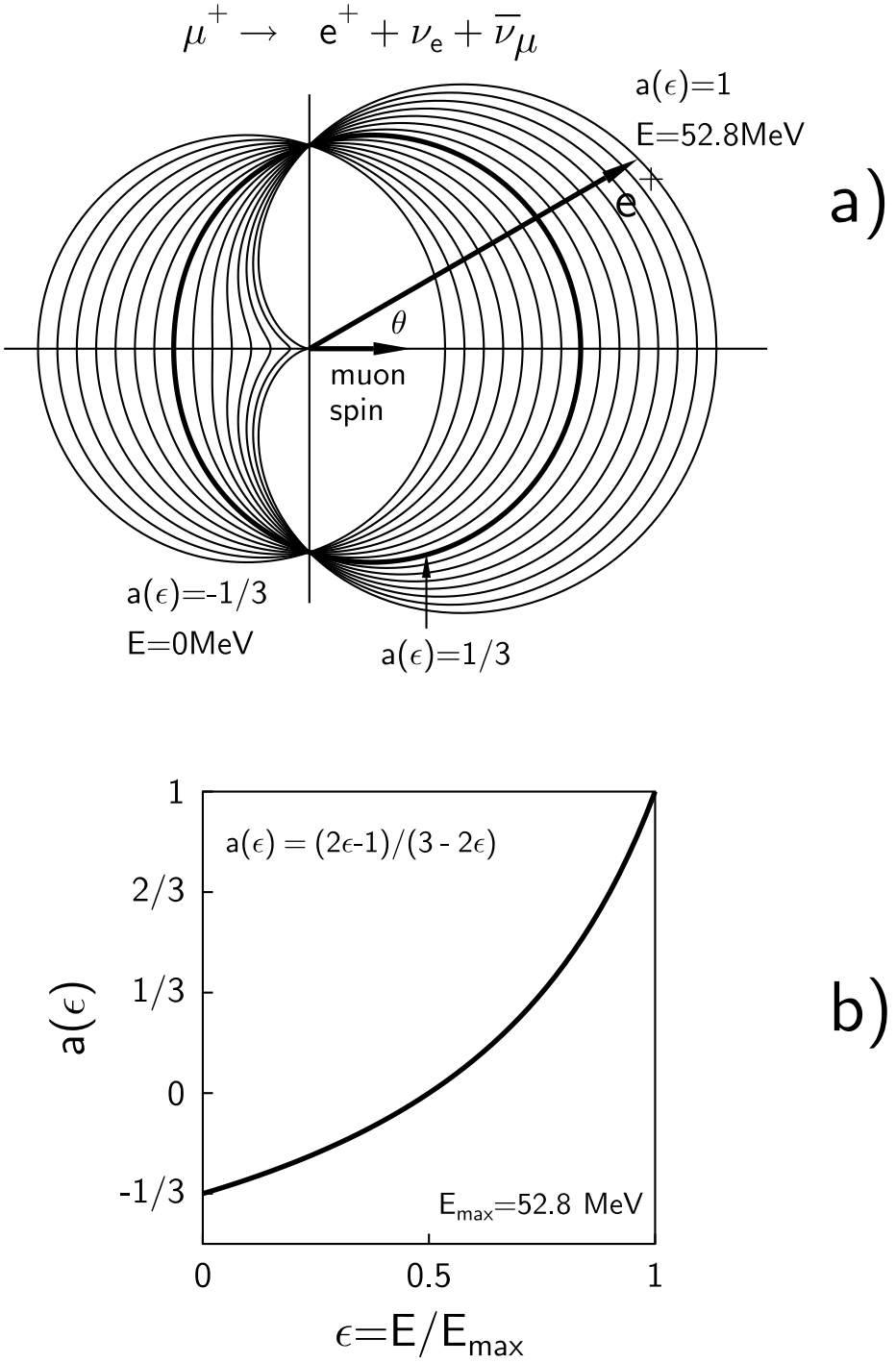

Figure 2.4: a) The muon decay is asymmetric. The lines about the muon position at the centre of the co-ordinate cross indicate the probability density for emission of the positron in the relevant direction. For different energies there are different distributions, with a maximum forward/backward asymmetry for the maximum energy of E = 52.8 MeV, which corresponds to a(ϵ) = 1. b) Energy dependence of the asymmetry factor a(ϵ).

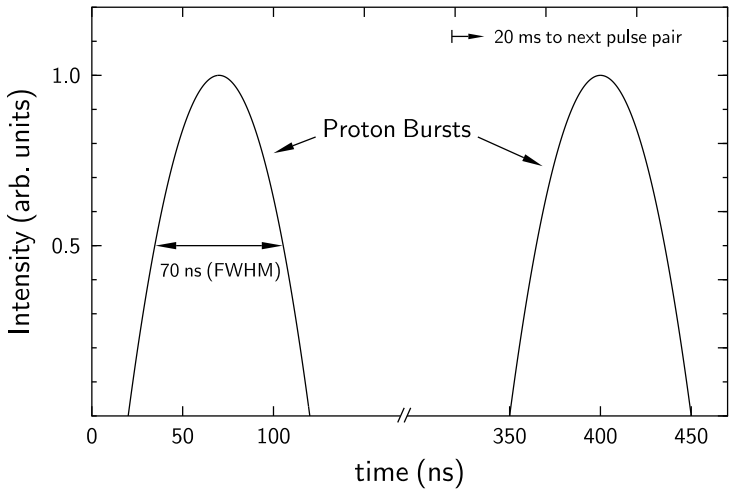

Figure 2.5: Proton pulse structure at the pulsed muon facility ISIS (Rutherford Appleton Laboratory, U.K.). The muon beams have essentially the same time structure as the proton beam, i.e. pulsed at 50 Hz with a double pulse of muons. The two pulses are utilized for different facilities at ISIS. After [Eato98].

nitude of muons in one muon pulse is 100. This results in typical muon rates of 20 to 40 million/hour. The rate is limited by the dead time of the detectors: errors occur if a second positron arrives before the detector has recovered from the previous positron detection. This dead time error can be reduced by segmenting the detector. Two of the ISIS beamline instruments have 32 detectors in total, the third one (RIKEN) has 192 detectors (see Table 2.3). The DIZITAL detector at ISIS is depicted in Figure 2.6.

The detectors have to be active only for a certain time after the muons pulse has arrived. Since the muon pulse frequency at ISIS is 50 Hz, and the active time of the detectors may be around 20 μs, the detectors are inactive most of the time, and thus less susceptible to random, time independent background noise. Because of the relatively low random background positron counts, experiments at pulsed sources are able to measure data reliably to longer times ($\sim$ 16 μs) than at continuous sources, see below.

The width (FWHM) of the muon pulse is $\Delta w \approx 70$ ns for the ISIS facility. Because of this distribution of muon implantation times, the maximum observable muon spin rotation frequency at pulsed sources is smaller than at continuous sources, where only one muon is in the sample at any time. This maximum frequency can be estimated as $\nu_{max} = \pi/(4\Delta w) \approx 10$ MHz.

Facility	PSI		ISIS		
Instrument	GPS	GPD	MuSR	EMU	RIKEN
type	continuous		pulsed (50 Hz)		
beam	μ^+ (sf*, ssf*)	μ^+, μ^-	μ^+ (sf*)		μ^+, μ^-
μ energy (MeV)	0.1–4.2	4.2–58	3.2		3.2 (μ^+)
beam size (fwhm)					
vertical(mm)	5.8	17	8	10	∼20
horizontal(mm)	5.3	28	7–15	9–27	∼10-20
data rate (10^6/hr)	10		20		40
muon polarization	> 95%	75%	100%		
detectors	5	2	32		192
ext. mag. field (mT)					
longitudinal	0–600	0–500	0–200	0–400	0–400
transversal	0–10	0–10	0–200	0–10	0–10
histogram width (ns)	1.25, 0.625		8, 16, 24, 32		16
typical spectrum size (bins)	8000		1000-1500		2000
temperature range (K)	2.5–300	0.3–300	0.050–1000	0.350–1000	0.300–480
other	spin-rotator				

Table 2.3: Characteristics of muon beamlines [User94, Eato98]. *sf stands for surface beam, ssf for subsurface beam.

2.2.2 Continuous Sources: PSI

At PSI, the proton source is a cyclotron and the muons are produced continuously. When a muon is implanted in the sample, which happens at random times, a detector starts a clock. The clock is stopped when the decay positron is detected (this is called one "event"). If during this time a second muon enters the sample, the two events are discarded. This is necessary since two expected decay positrons in the sample cannot be attributed uniquely to the two muons which were implanted at different times. This rejection algorithm has one distinct disadvantage: since the rejected events stem mostly from long-lived muons, the long-time behaviour (on the muon decay timescale) of continuous muons sources is not optimal. The other disadvantage of continuous sources as compared to pulsed sources is, that the detectors have to be active for a longer time and are thus subject to a higher background and false correlations. This again affects especially the long-time histograms, so that data can be taken reliably only at smaller times ($\lesssim 7\ \mu$s). There is also a limitation to the number of events one can have per time unit. In contrast, fast precession frequency measurements are limited only by electronics

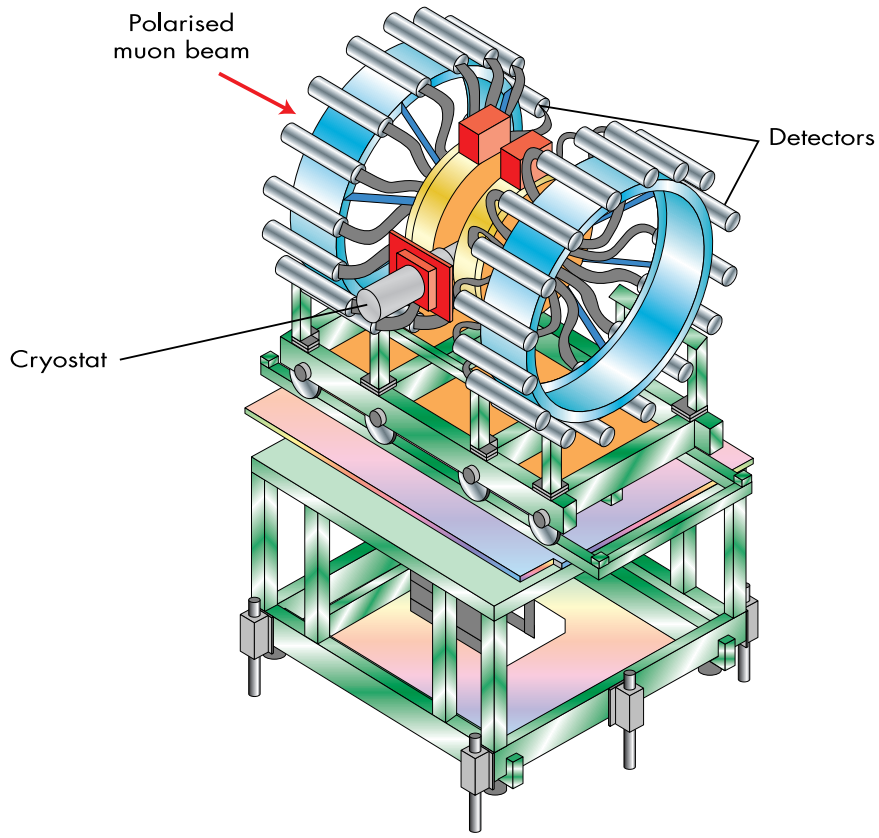

Figure 2.6: The DIZITAL spectrometer at ISIS (MuSR).

and detector response times, and frequencies up to several hundred MHz can be measured at PSI.

2.3 Muons in Matter

2.3.1 Implantation Process and Muon Sites

The muons come to rest in a sample in a time which is typically much shorter than τ_μ, and without significant change of the initial polarization. The details of the implantation process are described in this section. Most of the information given here can be found in [Chap84].

Surface muons are implanted into the specimen of interest with an energy of around 4 MeV. The stopping range of surface muons is typically 110mg/cm^2, and the range width is about 20 % [Eato98]. The typical range in materials of interest

is of the order of 1 mm. For decay beams, which might have much higher energies, sample containers with thicker walls may be used, or degraders to slow the muons down might be necessary. Muons lose energy through displacement and ionization of atoms and scattering with electrons, until their energy is of the order of 2 MeV. Then the muon captures and loses electrons rapidly (i.e. it forms muonium). At an energy of a few hundred eV inelastic collisions with the host atoms take place. All these deceleration processes happen on a time scale of $\sim 10^{-10}$ s, much smaller than τ_μ. Since the muon is positively charged, its equilibrium position will often be an interstitial site with minimum electrostatic potential in the specimen. In some materials, paramagnetic states will be formed, i.e. states with a non-zero electron-spin density at the muon site. In others, diamagnetic states (where there is no electron spin density at the muon site) are stable. In some materials, both charge states (and even $\mu^+e^-e^-$) can coexist. Muonium has never been observed in metals, and muons in oxides usually bond to one of the oxygen atoms, with a typical bonding length of 1 Å, see also Chapter 3.4.4. In many materials one finds only one unique crystallographic site for the muon, an issue that we will return to later.

The muon spin depolarization produced by Coulomb scattering is negligible. Therefore the positive muons are implanted into the sample without appreciable depolarization of the spin.

Only the initial part of the muon path is damaged through vacancy creation, since there is a threshold energy for this process. The muon comes to rest of the order of 1 μm away from the last produced vacancy, and reports of muon interaction with its track are very rare. Since there is only one muon (for continuous muon sources) or a few hundred muons (for pulsed sources) in the sample at any time, there will also be negligible muon-muon interaction.

2.3.2 Muon Spin interaction

We are interested in the evolution of the muon spin in time and how it is influenced by the local environment of the muon in our sample. We can, as mentioned above, discriminate between two cases: The muon might be in a *diamagnetic state*, and thus interact with its surroundings through magnetic fields (e.g. dipolar fields, or externally applied fields) only. This possibility is encountered in some of the later chapters when muons are used to study oxides (Chapters 3, 4 and 5). Or

	eigenvector	eigenvalue
$\|\Psi_1\rangle =$	$\|\uparrow_\mu\uparrow_e\rangle$	$E_1 = A\hbar^2/4\,(1+2mB/B_0)$
$\|\Psi_2\rangle =$	$\alpha\|\uparrow_\mu\downarrow_e\rangle + \beta\|\downarrow_\mu\uparrow_e\rangle$	$E_2 = -A\hbar^2/4\left(1-2\sqrt{1+(B/B_0)^2}\right)$
$\|\Psi_3\rangle =$	$\|\downarrow_\mu\downarrow_e\rangle$	$E_3 = A\hbar^2/4\,(1-2mB/B_0)$
$\|\Psi_4\rangle =$	$\beta\|\uparrow_\mu\downarrow_e\rangle - \alpha\|\downarrow_\mu\uparrow_e\rangle$	$E_4 = -A\hbar^2/4\left(1+2\sqrt{1+(B/B_0)^2}\right)$

$$B_0 = A\hbar/\{\gamma_\mu+\gamma_e\}\ \ ,\ m=(\gamma_e-\gamma_\mu)/(\gamma_e+\gamma_\mu)\approx 0.990,$$

$$\alpha = \tfrac{1}{\sqrt{2}}\sqrt{1-\tfrac{B/B_0}{\sqrt{1+(B/B_0)^2}}}\ \ ,\ \beta = \tfrac{1}{\sqrt{2}}\sqrt{1+\tfrac{B/B_0}{\sqrt{1+(B/B_0)^2}}}$$

Table 2.4: Eigenstates and eigenvalues of Muonium. For free muonium, B_0 = 0.1585 T.

the muon might combine with an electron to form muonium, and therefore in addition to the diamagnetic interactions there will be a non-zero spin density at the muon site, which results in additional hyperfine interactions (i.e. the muon is in a *paramagnetic state*). These two cases are now dealt with in more detail.

Diamagnetic Muon States

If the muon is in a diamagnetic state and there is a local magnetic field $\mathbf{B}$, the Hamiltonian of interest is

$$H = -\gamma_\mu\,\mathbf{S}\cdot\mathbf{B} = -\gamma_\mu\,S_z B,\ . \tag{2.7}$$

where $\mathbf{S}$ is the muon-spin operator, with S_z being the z-component (we are neglecting possible quadrupolar interaction). This is the Zeeman interaction, and the eigenstates can be taken as spin parallel and antiparallel to $\mathbf{B}$. The energy splitting between the two states is $\hbar\gamma_\mu B$, where $B = |\mathbf{B}|$.

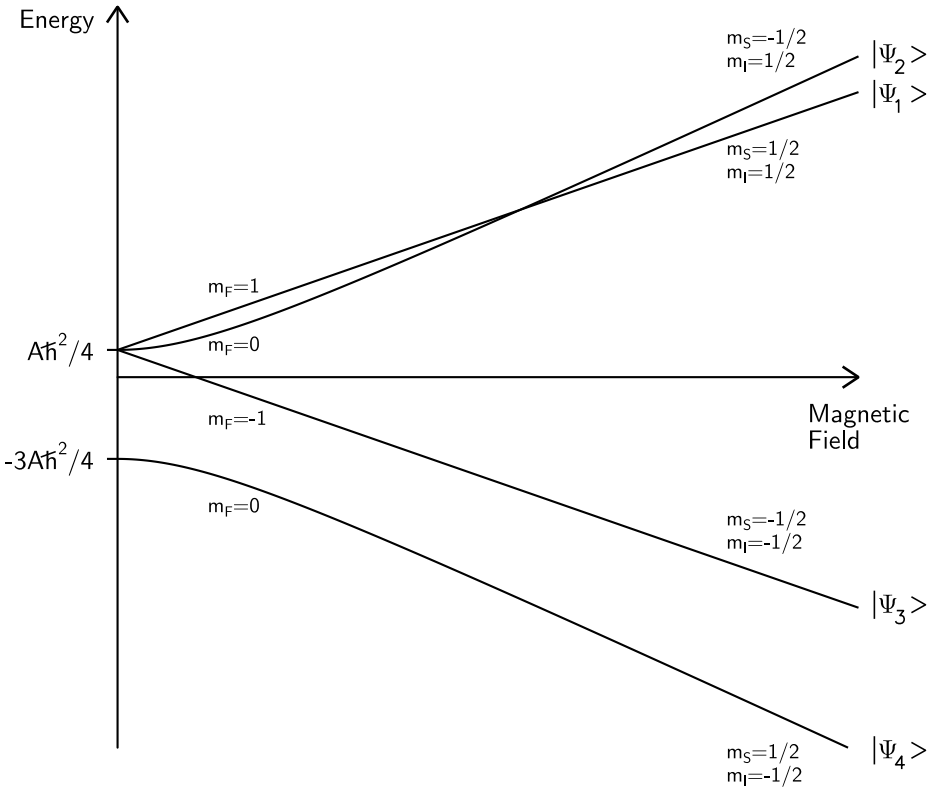

Figure 2.7: Breit-Rabi diagram for muonium.

Muonium States

Muonium (Mu = μ^+e^-) can be considered as an isotope of hydrogen, with a Bohr radius and Bohr energy close to the value of hydrogen. If we consider a free, isotropic muonium state, we can write the relevant Hamiltonian as

$$H = -\gamma_\mu \mathbf{S}\cdot\mathbf{B} + \gamma_e \mathbf{I}\cdot\mathbf{B} + A\,\mathbf{S}\cdot\mathbf{I} = -\gamma_\mu S_z B + \gamma_e I_z B + A\,\mathbf{S}\cdot\mathbf{I} \qquad (2.8)$$

where $\mathbf{I}$ is the electron spin-operator, $\gamma_e = 2\pi \times 2.80247 \times 10^{10}$ Hz/T the electron gyromagnetic ratio and A the (isotropic) hyperfine coupling constant. The eigenvalues and eigenvectors of this Hamiltonian can be calculated, and the results are shown in Table 2.4. As a basis of the spin Hilbert-space we use the product of the muon and electron spin up and down vectors, $|\Psi\rangle = |\chi_\mu\rangle \otimes |\chi_e\rangle = |\chi_\mu\chi_e\rangle$.

As can be seen from Figure 2.7, the eigenstates at low fields are one triplet state and one singlet state. The eigenstates in this regime are given by the basis

vectors of the $|\mathbf{F} = \mathbf{S}+\mathbf{I}, m_F\rangle$ basis. At high fields (the Paschen-Back regime), the eigenstates are given by the basis vectors of the $|m_S, m_I\rangle$ basis, where m_i (i = F, S, I) is the eigenvalue of the z-component of $\mathbf{F}$, $\mathbf{S}$, $\mathbf{I}$. In this regime ($\gamma_e B \gg A\hbar^2$) the electron and muon spins are decoupled.

Suppose we implant muons in a sample and apply a magnetic field in the direction of the spin polarization. It then can be shown (see Appendix A.1) that the muon spin polarization

$$P_z(t) = \frac{1 + 2(B/B_0)^2}{2\{1 + (B/B_0)^2\}} + \frac{1}{2\{1 + (B/B_0)^2\}} \cos(\omega_{24} t) \tag{2.9}$$

where $\omega_{24} = A\hbar\sqrt{1 + (B/B_0)^2}$. For free muonium, $B_0 = 0.1585$ T. The incoming muons are spin polarized, while the electrons which are picked up to form the muonium are not spin-polarized. Therefore the initial states will be a combination of $|\uparrow_\mu\uparrow_e\rangle$ and $|\uparrow_\mu\downarrow_e\rangle$, see Table 2.4. The oscillating term results from the fact that some of the spin-polarized muons will not form eigenstates of the muonium.

Physical consequences will be considered below (Section 2.4.4) and later.

2.4 Muon Spectroscopy

In a μSR experiment one measures the time evolution of the muon spin polarization $\mathbf{P}(t)$ of the muon ensemble implanted into the sample. The muon is a dilute probe, and since muons are "naturally" spin polarized, no external fields need to be applied. However, external fields may be applied to elucidate the underlying physics, see below. Since the direction of the positron emission is correlated with the muon spin at the time of the muon decay, recording emitted positrons as a function of time after the muon was implanted will give $\mathbf{P}(t)$. A typical μSR setup consists of the sample and a number of detectors i (see e.g. Figure 2.6). The number of detected positrons for each detector i is stored in histograms $N_i(t)$, with

$$N_i(t) = N_i\, e^{-t/\tau_\mu} \{1 + a_i P_i(t)\} + b_i\ , \tag{2.10}$$

where b_i is a time independent random background counting rate, $P_i(t)$ is the projection of the polarization vector function $\mathbf{P}(t)$ on the axis connecting the centre of the sample with the centre of the detector and N_i is a calibration factor. The time t is measured from the time of the muon implantation. For ISIS, the typical

number of histograms channels is 1000–2000 for a channel width of 16 ns, see also Table 2.3. The number of total events taken per spectrum varies, depending on the desired accuracy, and it is typically between 3 million and 20 million.

I now explain how to obtain $\mathbf{P}(t)$ or a Cartesian component of it. We call the detector in the direction (as seen from the sample) of the spin polarization of the incoming muons "forward" ($i = F$) detector and the opposing one "backward" ($i = B$) detector. We rename $N_F(t) \rightarrow F(t)$ and $N_B(t) \rightarrow B(t)$. If there is more than one detector in the forward and backward direction, we obtain $F(t)$ and $B(t)$ by summing up the histograms of the relevant detectors, i.e. $F(t) = \sum_{i \in \mathcal{F}} N_i(t)$ and $B(t) = \sum_{i \in \mathcal{B}} N_i(t)$, where $\mathcal{F}$ and $\mathcal{B}$ are the sets of forward and backward detectors, respectively. By looking at these opposing detectors, i.e. $P_F(t) = -P_B(t) = P(t)$, defining the calibration parameter $\alpha = N_F/N_B$ and assuming $a_F = a_B = a_0$ we get

$$a_0 P(t) = \frac{F(t) - \alpha B(t)}{F(t) + \alpha B(t)}. \tag{2.11}$$

Here we treat b_F and b_B (see Equation 2.10) as negligible (in the case of a pulsed muons source) or as corrected for (by fitting appropriately, in the case of a continuous muon source). The parameter α accounts for different detector efficiencies of the F and B detectors, and is of the order of 1.

The polarization function $\mathbf{P}(t)$ is determined by various physical parameters:

- The external (=applied) magnetic fields B_{ext},
- the internal (microscopic) magnetic fields and hyperfine interactions in the sample, and their spatial distribution, and
- the temporal variations of these fields.
- The possible occurrence of muon hopping within the sample, which would influence $\mathbf{P}(t)$ in a similar way as temporal variations of the internal fields do.

Suppose that there is a static magnetic field $(B_x, B_y, B_z) = \mathbf{B}_\mu = \boldsymbol{\omega}_\mu/\gamma_\mu$ at an angle θ to the muon (ensemble) spin polarization. Then the Larmor equation yields

$$P(t) = \cos^2\theta + \sin^2\theta \cos(\omega_\mu t)\ , \tag{2.12}$$

where $\omega_\mu = |\boldsymbol{\omega}_\mu|$. This is the basic equation of muon spectroscopy of magnetic materials, and much of the following will be based on it.

2.4.1 Detectors, Geometries, Definitions and Notations

One can classify experimental geometries according to the applied external fields (see Figure 2.8): in a transverse field (TF) setup, the applied field is perpendicular to the initial muon spin direction. In a longitudinal field (LF) setup the applied field is parallel to the initial muon spin direction. A zero field (ZF) setup is the limiting case of a LF setup with no applied field. In the following I will call the relevant Cartesian component of the polarization function for cases in transverse field P_x, and for cases in zero field or longitudinal field P_z. In each case, the initial spin of the muon ensemble is taken to be along the z-axis.

2.4.2 Transverse Fields (TF)

If we apply a magnetic field perpendicular to both the spin polarization of the incoming muons and the axis connecting the centres of the two detectors we will get a polarization function

$$P_x(t) = \cos(\omega_\mu t + \varphi) \,, \tag{2.13}$$

see Equation 2.12 (φ is a phase factor). However, in most experiments there will be a distribution of fields at the muon site, caused by the surroundings (dipolar interactions, hyperfine interactions etc.). This will also lead to a distribution function $p(\omega)$ of frequencies in Equation 2.13, resulting in a dephasing of the muon spins. As a result, one will observe a damping of the oscillations. By modifying the right hand side of Equation 2.13 we get

$$P_x(t) = \int d\omega \; p(\omega) \cos(\omega t + \varphi) = G_x(t) \cos(\omega_\mu t + \varphi). \tag{2.14}$$

We call G_x the transverse relaxation or depolarization function. If we assume a Gaussian distribution of *static* magnetic fields,

$$p(B_i) = \frac{\gamma_\mu}{\sqrt{2\pi}\Delta} \; \exp\left\{ \frac{-(\gamma_\mu B_i)^2}{2\Delta^2} \right\} \tag{2.15}$$

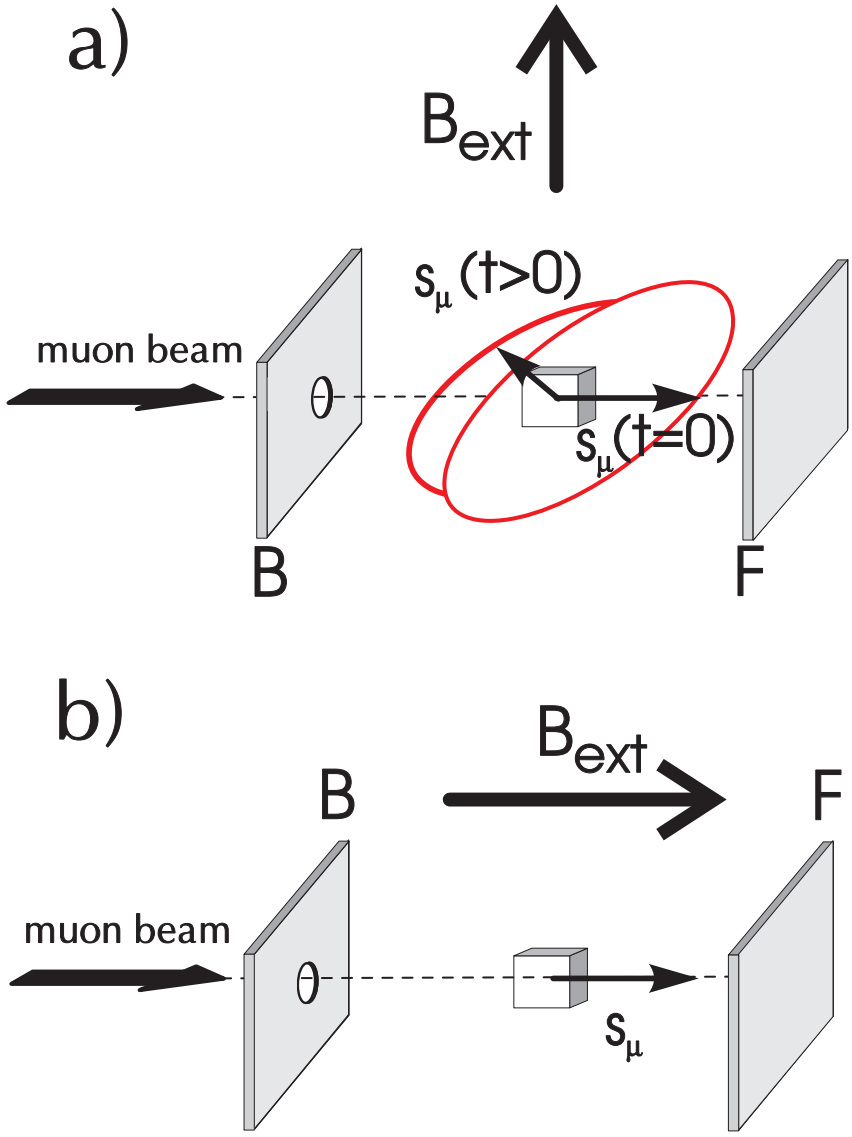

Figure 2.8: a) Transverse Field (TF) setup. The incoming muons experience a field perpendicular to their spin. Therefore the pattern of Figure 2.4 a) rotates in time with the frequency $\nu_\mu = \gamma_\mu B_{ext}/(2\pi)$. b) Longitudinal Field (LF) setup. The spin polarization of the muon spin and the applied external field are parallel.

with $i = x$, then we get a Gaussian depolarization function

$$G_x(t) = e^{-\frac{1}{2}\Delta^2 t^2}. \tag{2.16}$$

Here Δ is the width of the field distribution. If we extend the model to include fluctuations of the local random fields with a correlation time $1/\nu$, i.e.

$$\frac{\langle B(t)B(0)\rangle}{\langle B^2(0)\rangle} = e^{-\nu t} \ , \tag{2.17}$$

then we get [Chap84]

$$G_x(t) = \exp\left\{-\Delta^2/\nu^2\left[e^{-\nu t} - 1 + \nu t\right]\right\} \ . \tag{2.18}$$

In the fast fluctuation limit the observable relaxation function becomes exponential, $G_x(t) = \exp\{-\Delta^2 t/\nu\}$.

In the context of this thesis, TF experiments are mainly used in "T20" measurements in order to obtain the parameter α (see Equation 2.11). In such measurements a transversal magnetic field (of the order of 2 mT = 20 Gauss) is applied. From the data count in the forward and backward detectors one can arrive at the polarization function by fitting the data from Equation 2.11 by Equation 2.14, where G_x is taken as a decaying function. An example for such a procedure is shown in Figure 2.9. In Chapter 6 TF experiments are also used to elucidate the properties of a muon state in a polymer. The relevant background information is given in Chapter 6.1.

2.4.3 Zero Field (ZF) and Longitudinal Field (LF)

We now look at the depolarization functions for situations in zero applied field with static internal fields present, then extend the results to situations with applied LFs, and finally introduce fluctuations of the internal fields.

In μSR, measurements can be performed in zero applied field, since in contrast to NMR the probe spins are intrinsically polarized. If the *direction* of the internal magnetic fields is random but their magnitudes take on only one single value (such as in a polycrystalline magnet), one has to average over the possible angles θ in

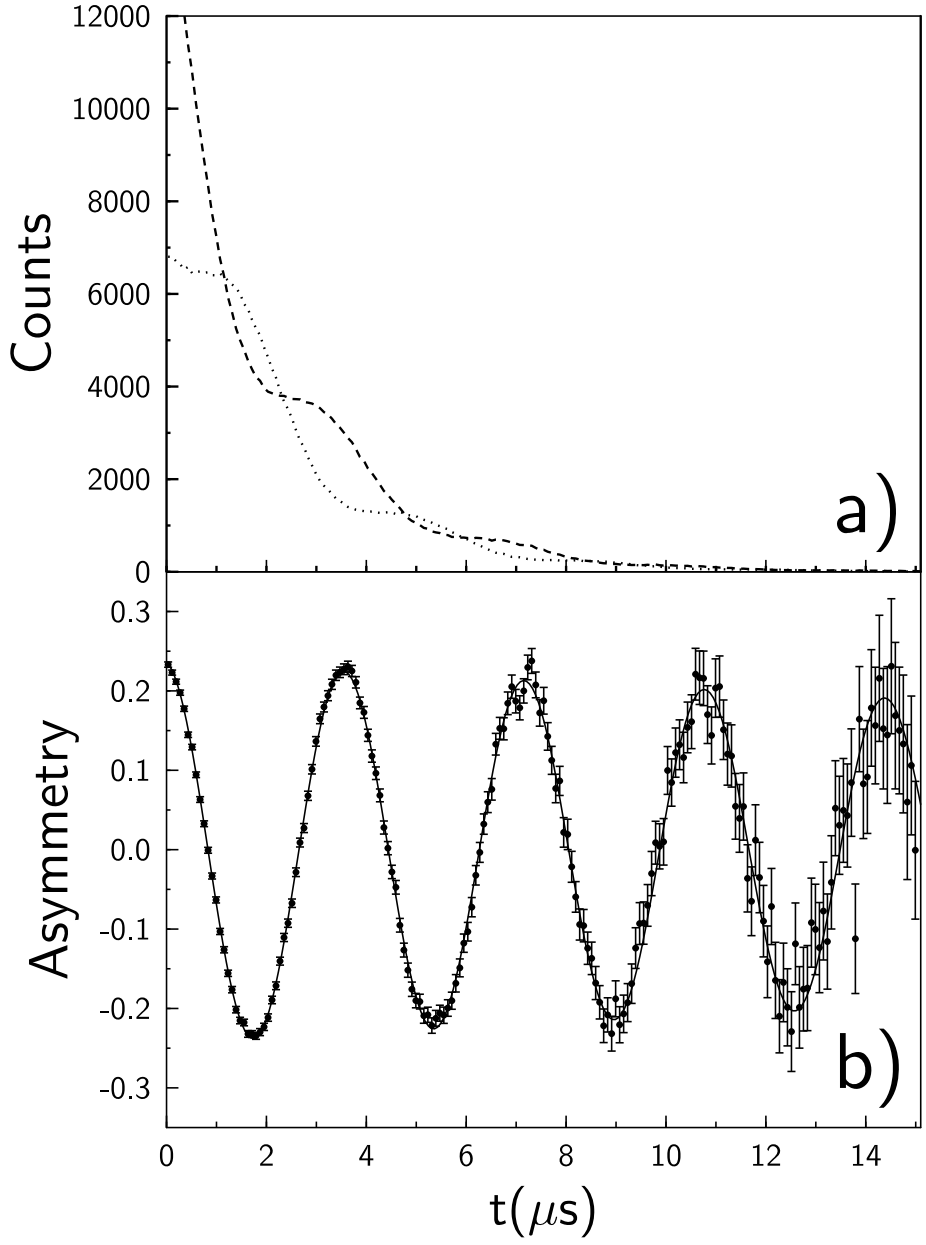

Figure 2.9: Example of a "T20" calibration run. a) The dashed and dotted lines are the measured data and refer to the forward and backward detectors, respectively. b) the data points and the full line are the corresponding asymmetry data and the fitted function. For this data set ($La_{2-x}Sr_xNiO_{4+\delta}$, x = 0.33 at T = 293 K) we find $\alpha = 1.29$.

Equation 2.12, and the muon spin polarization function will be given by

$$P_z(t) = \frac{1}{3} + \frac{2}{3}\cos(\omega_\mu t). \tag{2.19}$$

The first term describes the polarization parallel to the local fields (zero-frequency component), the second term describes the precession of the *transverse* components and reflects the magnetic order in the sample. In the absence of an external field, the frequency ω_μ is proportional to the internal magnetic field at the muon site and hence to the local magnetic order parameter, e.g. the staggered magnetization in an antiferromagnet. If there is more than one muon site in the crystal (where we have to consider the *magnetic* unit cell) then the above formula is easily extended.

When the distribution of fields at the muon site is too large, e.g. in the case of a small correlation length of the magnetic order, then the oscillation might be strongly damped, see below. For some samples the oscillation is fast compared to the time resolution of the muon spectrometer, and then one can see only a time average of the cos term in Equation 2.19, i.e. $P_z(t) = 1/3$. In these cases a drop of the inital asymmetry from 1 to 1/3 will be a signature of a magnetic phase transition as we go through it. In zero field and longitudinal field the polarization function P_z and the depolarization function G_z are identical, and are sometimes used interchangeably.

If we have a zero external field and static internal fields with a Gaussian distribution, as in Equation 2.15 with $i = x, y, z$, then we get the *zero field static Kubo-Toyabe* (ZF-sKT) formula

$$G_z(t, \Delta) = \frac{1}{3} + \frac{2}{3}(1 - \Delta^2 t^2)e^{-\frac{1}{2}\Delta^2 t^2} \tag{2.20}$$

where Δ^2 is the second moment of the x and y components of the random dipolar fields. Figure 2.10 shows this function for several values of Δ. For short times the ZF-sKT function can be approximated by a Gaussian function. It decays to a value of 1/3 at a time $t = \Delta^{-1}$, it then has a minimum and recovers to the value of 1/3. Below we will see that this 1/3 tail decays for a situation where we have *dynamic* local fields.

If we consider a situation with an applied LF, we have to make the replacement $B_z \rightarrow (B_z - B_{ext})$ in Equation 2.15. We call $\omega_\mu = \gamma_\mu B_{ext}$. We then get [Haya79]

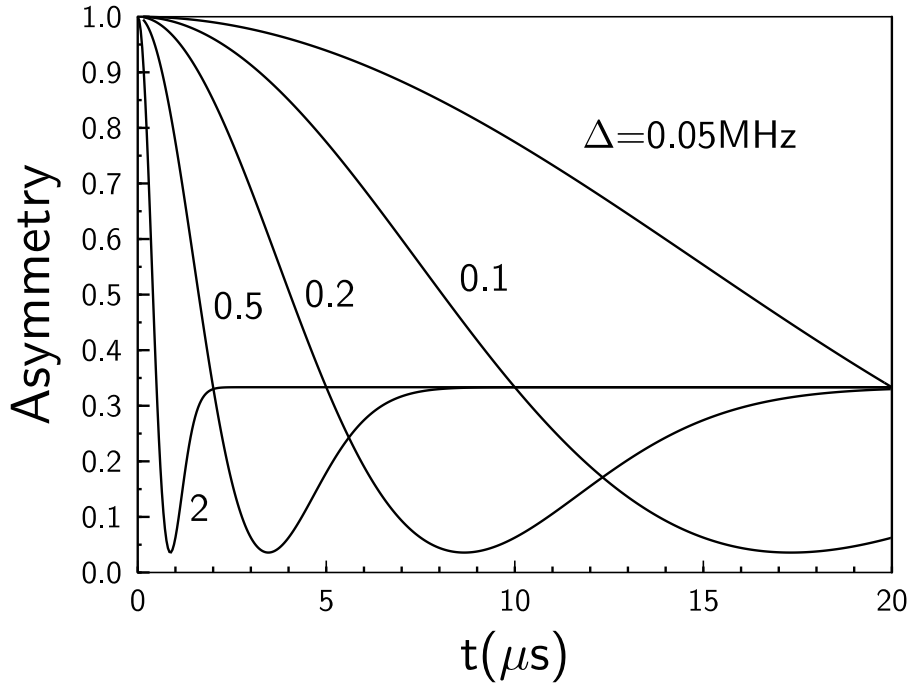

Figure 2.10: Static Kubo-Toyabe function for zero field, see Equation 2.20. Note that there is a scaling law: if the function is plotted vs. Δt then we get only *one* universal curve for any value of Δ.

the *longitudinal field static Kubo-Toyabe* function (LF-sKT)

$$G_z(t,\Delta,B_{ext}) = 1 - \frac{2\Delta^2}{\omega_\mu^2}\left(1 - e^{-\Delta^2 t^2/2}\cos\omega_\mu t\right) + \frac{2\Delta^3}{\omega_\mu^3}\int_0^{t\Delta} dt' e^{-t'^2/2}\sin\left(\frac{\omega_\mu t'}{\Delta}\right). \tag{2.21}$$

In this situation, see Figure 2.11, the applied longitudinal field can decouple the muon spin from internal magnetic fields, i.e. the recovery value of 1/3 seen at long times for the ZF-sKT function becomes larger, and for large external fields (compared to the internal field distribution) this value approaches 1.

We now introduce temporal fluctuations of frequency ν of the internal magnetic fields, as in Equation 2.17. We therefore model either fluctuations of the local spins (in the case of dipolar fields) or muon diffusion. This can be done in the "strong collision model" [Haya79]. In this model the time evolution of $G_z(t)$ consists of contributions of muons which did not jump until the time t, which jumped once,

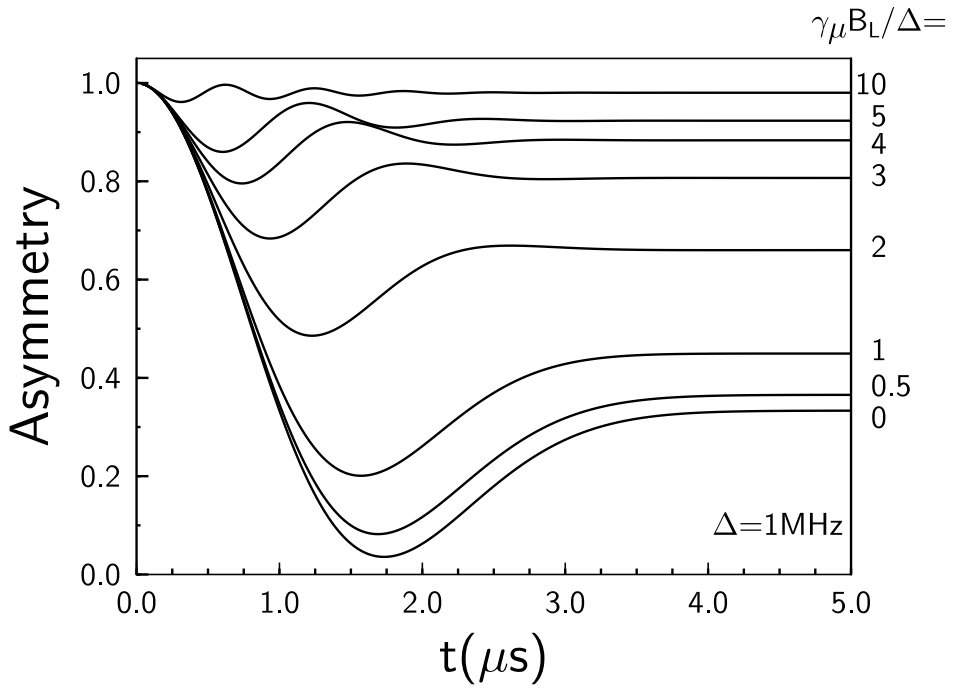

Figure 2.11: Static Kubo-Toyabe function for various external magnetic fields $B_L = \omega_0/\gamma_\mu$, see Equation 2.21. The magnetic field is given in units of Δ/γ_μ.

twice, etc. This leads to the expression

$$G_z(t, \Delta, B_{ext}, \nu) = \sum_{n=0}^{\infty} g_z^{(n)}(t) \ , \tag{2.22}$$

where the n in the sum stands for the number of hops of the muon (or changes in the magnetic field) and

$$g_z^{(n)}(t) = \nu^n e^{-\nu t} \int_{t_n}^{t} dt_n \ldots \int_0^{t_1} dt_1 \, g_z(t - t_n) g_z(t_n - t_{n-1}) \ldots g_z(t_1) \tag{2.23}$$

where g_z is the LF-sKT function from Equation 2.21. This is the *dynamic Kubo-Toyabe* (dKT) function. The form of this function can be obtained numerically. Note that a scaling law is applicable for all KT functions: $G_z(t, k\Delta, kB_{ext}, k\nu) = G_z(kt, \Delta, B_{ext}, \nu)$.

In Figure 2.12 the dKT function is displayed for ZF. For slow hopping [Haya79] the 1/3 recovery of the ZF-sKT function is suppressed and the asymptotic form is $G_z(t, \nu) = 1/3 \times \exp(-2\nu t/3)$ for $t \gg 3/\Delta$.

In Figure 2.13 the dKT function is plotted for a fixed correlation frequency ν and various external magnetic fields. For increasing fields G_z becomes less steep,

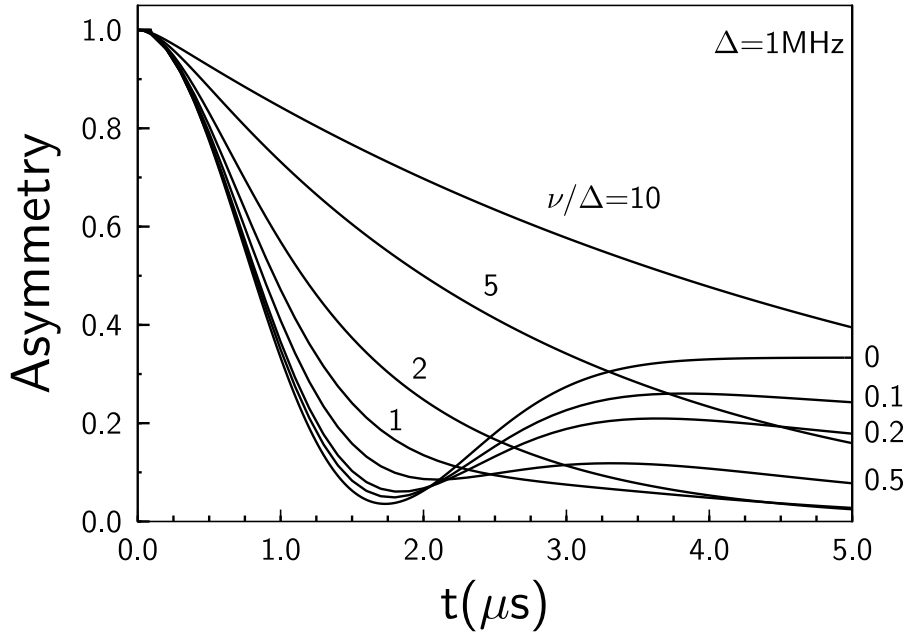

Figure 2.12: Dynamic Kubo-Toyabe function for zero applied field, with various correlation times $1/\nu$, given in units of $1/\Delta$.

for large fields it is flat and close to 1. This figure can be compared to Figure 2.11, where $\nu = 0$. In both regimes the initial decay has Gaussian character, though in the dynamic regime the curve is more featureless at longer times.

Figure 2.14 displays the dKT function for a fixed external field and for a range of correlation frequencies ν. As ν is increased the long-time behaviour becomes more like an exponential curve. Indeed, in the fast fluctuation limit the polarization function can be written as $G_z(t) = e^{-\lambda t}$ with

$$\lambda = \frac{2\Delta^2 \nu}{\nu^2 + \omega_\mu^2}\,, \tag{2.24}$$

see [Uemu85]. Depending on the model, one can arrive at other depolarization functions. In later chapters we will introduce other functions, in order to correctly describe the observed data. For example, in a limit of dilute spins one will obtain a "root-exponential" function. In order to fit G_z efficiently, sometimes a semi-phenomenological "stretched exponential" function,

$$G_z(t) = \exp\left\{-(\lambda t)^\beta\right\}\,, \tag{2.25}$$

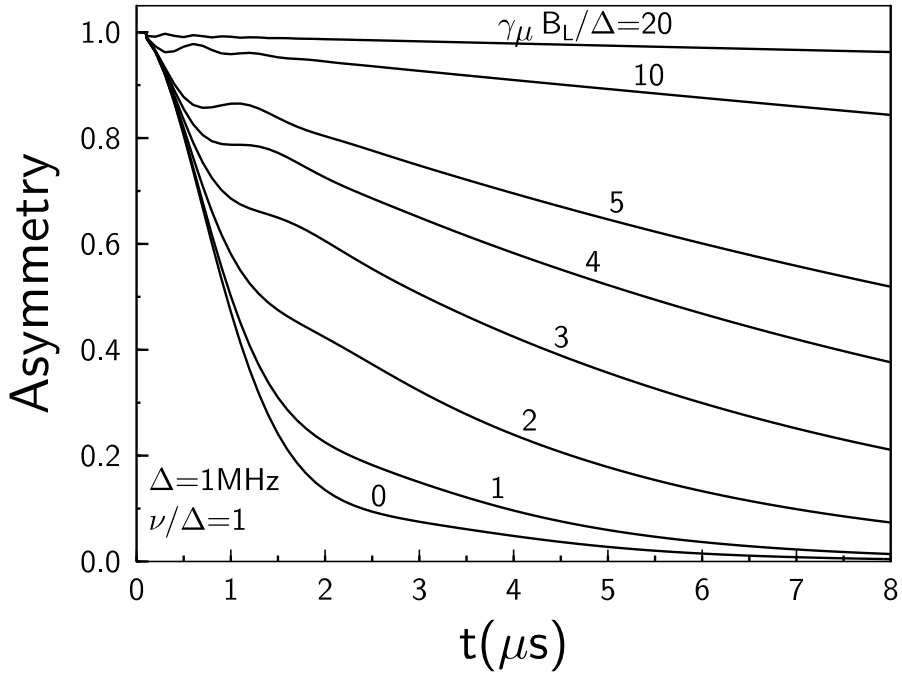

Figure 2.13: Dynamic Kubo-Toyabe function for a fixed correlation time $1/\nu$ and various external magnetic fields B_L, given in units of Δ/γ_ν.

is used. The root-exponential is the case with $\beta = 1/2$, while $\beta = 1$ or 2 describe an exponential or Gaussian decay. Values of $\beta < 1$ are observed in the presence of an inhomogeneous distribution of relaxation rates.

2.4.4 Repolarization

Sometimes longitudinal magnetic fields are applied in order to investigate the nature of the underlying physics more closely. Two scenarios, first the presence of muonium in the sample and second a diamagnetic muon in a magnetic material, are treated briefly in the following.

Muonium repolarization

If a muonium state is formed and we apply a LF magnetic field we will obtain the polarization function in Equation 2.9. Half of the muons are in the eigenstate $|\uparrow_\mu\uparrow_e\rangle$, the other half in the non-eigenstate $|\uparrow_\mu\downarrow_e\rangle$, which gives rise to the cosinus-term in Equation 2.9, see Table 2.4. Usually the cos-term is not observed, owing to the large value of ω_{24}. For zero applied field the initial polarization $P_z(t = 0, B = 0) = \frac{1}{2}$, and there is a "missing fraction" of muon polarization. On increasing the

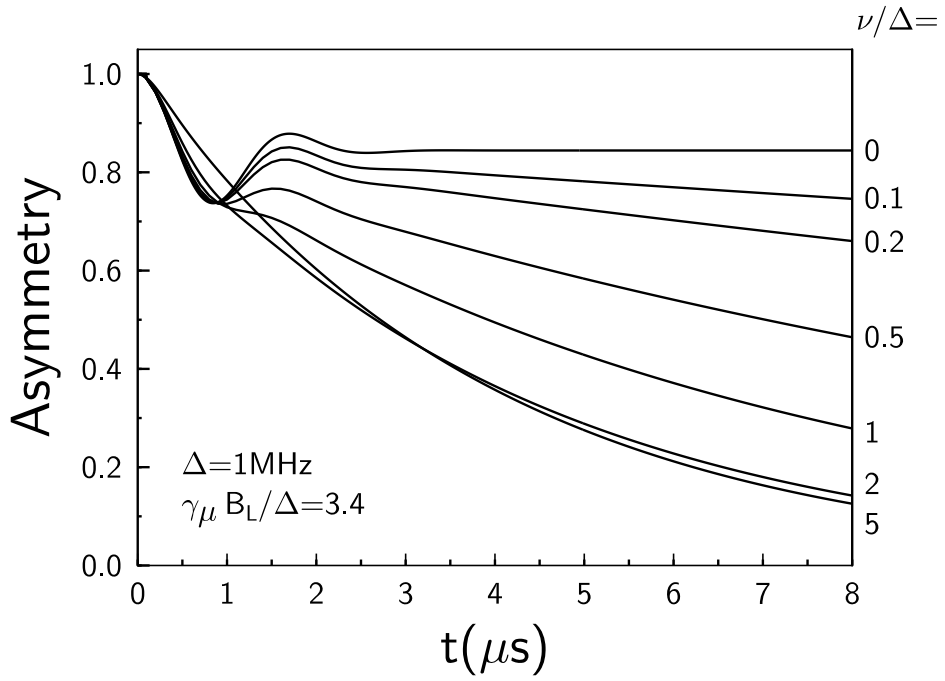

Figure 2.14: Dynamic Kubo-Toyabe function for a fixed external magnetic field B_L, and various correlation times $1/\nu$, given in units of $1/\Delta$.

magnetic field B, the Zeeman energy dominates, and the electron and muon spins become decoupled, i.e. $|\Psi_4\rangle \longrightarrow |\uparrow_\mu\uparrow_e\rangle$, see also Table 2.4. This "repolarization" is illustrated in Figure 2.15 and given by

$$P_z(B) = \frac{1 + 2(B/B_0)^2}{2\{1 + (B/B_0)^2\}} \,, \tag{2.26}$$

see Equation 2.9. For anisotropic muonium, the repolarization is slightly more complicated, see for example [Prat93, Prat97a].

Repolarization for diamagnetic muons

Figures 2.11 and 2.13 illustrate the effect of external magnetic fields for muons in magnetic materials. For sufficiently strong magnetic fields, $P_z(t) = 1$, i.e. we have "quenched" the internal field. If the sources of the depolarization are strongly fluctuating fields, the external fields available at μSR beamlines are sometimes too weak to achieve quenching. For static internal fields caused by nuclear moments, usually applied fields of the order of a few Gauss are sufficient to cause quenching.

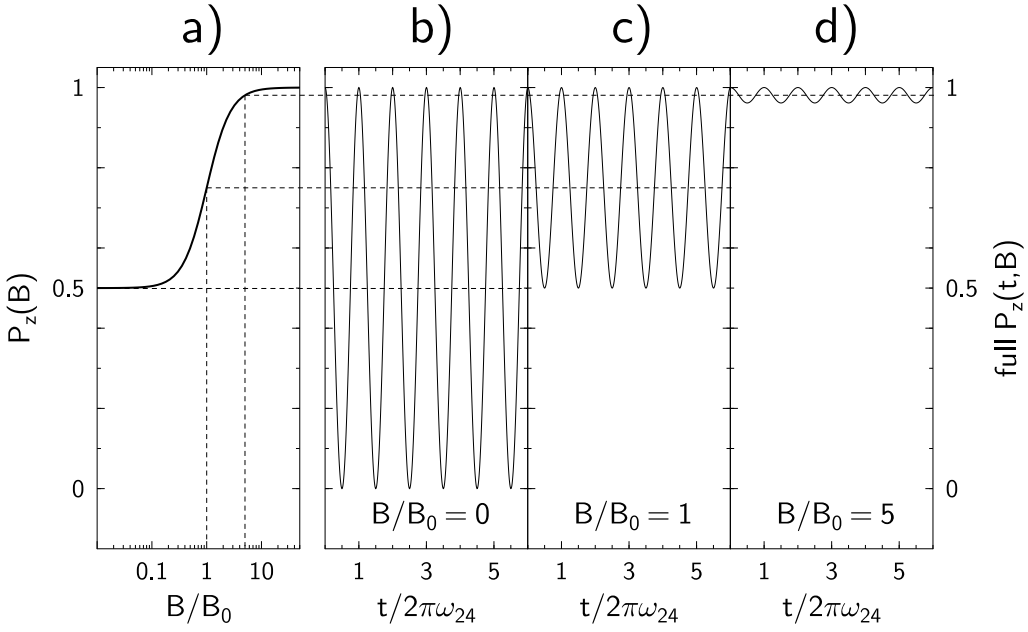

Figure 2.15: Muonium repolarization curve. a) The field dependent repolarization curve, see Equation 2.26. b) - d) the "full" muon polarization function for various values of B/B_0, including the cos-term in Equation 2.9, which is averaged out in a realistic μSR experiment.

Chapter 3

Magnetic order in $La_{2-x}Sr_xNiO_4$

Contents

In this chapter I report μSR measurements on a series of compounds with composition $La_{2-x}Sr_xNiO_{4+\delta}$ (nickelates) with strontium doping level x between 0 and 1. A magnetic transition is found in all the samples studied, which occurs at a composition-dependent temperature T_M.

This study has led to conclusions about the character of the magnetic phase diagram and the appropriate parameter for the characterization of the magnetic to non-magnetic transition which differ from to those based on a previous much more limited data set. The μSR technique is a sensitive method for investigating *local* magnetic order and of the nickel spin fluctuation rates, see Chapter 2. These experiments complement other investigations of the nickelates by (1) providing information on the temperature and composition dependence of the magnetic short-range order parameter, (2) enabling estimates of the magnetic transition temperatures T_M and the corresponding phase diagram to be made and (3) making estimates of the spin fluctuation rates.

In particular, below the transition temperature muon precession signals in zero-applied field are observed. This shows that there is at least short range magnetic order on a timescale longer than 10^{-8} s at low temperatures, indicating that speculations [Land91, Stra91] that the strontium doped compounds might have a spin glass ground state for certain doping levels need reexamination (see section 3.4.1). Above T_M the correlation time of the internal magnetic field at the muon decreases by several orders of magnitude. An interesting observation is that both T_M and the zero temperature staggered magnetization, $M^\dagger(x, T = 0\text{ K})$, show a peak at $x = 0.33$, a fact that might be due to enhanced hole localization at this strontium doping level.

This chapter is arranged as follows: In section 3.1 I describe properties of the nickelates obtained from neutron and electron diffraction as well as other experimental methods. In section 3.2 details of the sample preparation and characterization procedure are given. In section 3.3 I give a short description of the experimental setup used in this study and in section 3.4 the results are presented and discussed, stressing in particular the magnetic order in the samples, the static and dynamic nature of the nickel spins and the phase diagram of the doped samples. In this section I also discuss the likely muon site(s) in the nickelates. The last section (3.5) contains concluding remarks.

The work described in this chapter follows preliminary investigations of the nickelates [Chow96a, Chow96b] and parts of it have been published [Jest99].

3.1 Introduction

La_2NiO_4 and La_2CuO_4 are antiferromagnetic insulators with the layered perovskite (K_2NiF_4) structure, see Figure 3.1; they have a high degree of oxygen $2p$ character in the valence band and transition metal $3d$ character in the conduction band. Hole doping can be achieved by (1) substitution of Sr^{2+} for La^{3+} or (2) intercalation of excess oxygen. Although $La_{2-x}Sr_xCuO_{4+\delta}$ and $La_{2-x}Sr_xNiO_{4+\delta}$ are isostructural (though with different tilting distortions), there are dramatic differences in the effects of hole doping on their electrical and magnetic properties. In $La_{2-x}Sr_xCuO_{4+\delta}$ antiferromagnetic long-range order is replaced by short-range 2D correlations for $x \geq 0.02$ [Thur89, Cheo91] and the material becomes metallic and superconducting with the maximum T_C at $x \sim 0.15$ [Bedn86]. $La_{2-x}Sr_xNiO_{4+\delta}$ shows significant enhancement in conductivity (seen beyond $x = 0.6$), with truly metallic behaviour down to $T = 5$ K beyond $x \sim 1$, but no superconductivity is observed at any composition [Cava91, Tavi91].

The differences between $La_{2-x}Sr_xCuO_{4+\delta}$ and $La_{2-x}Sr_xNiO_{4+\delta}$ provide an incentive to understand the nature of the ground state in the doped nickelates and consequently their magnetic properties have been investigated using a variety of methods. Electron diffraction [Chen93] and neutron scattering [Hayd92, Tran94a, Tran94b, Yama94, Sach95, Tran95a] measurements have been instrumental in providing detailed microscopic information on the arrangement of the spins and holes in lightly doped nickelates. Electron diffraction studies [Chen93] find evidence for a 2D ordered array of localized doped holes at low temperatures for $x < 0.5$. The spin as well as the charge structures have also been probed extensively by neutron diffraction measurements [Hayd92, Tran94a, Tran94b, Yama94, Sach95, Tran95a, Tran96, Tran97a, Tran97b, Naka97]. These studies in general agree that as the doping level of the holes in the nickelates is increased, 3D antiferromagnetic order is suppressed and is replaced by 2D incommensurate correlations within the Ni-O planes. In particular, many interesting measurements have been reported for samples with no strontium, i.e. $x = 0, \delta \neq 0$. For example, [Tran94a] and [Tran95a] report an ordering of interstitial oxygens for $\delta = 0.125$ near room temperature and provide convincing evidence that below 110 K the magnetic state consists of antiferromagnetic stripes of nickel spins separated by periodically spaced anti-phase domain walls to which the holes segregate, see Figure 3.2.

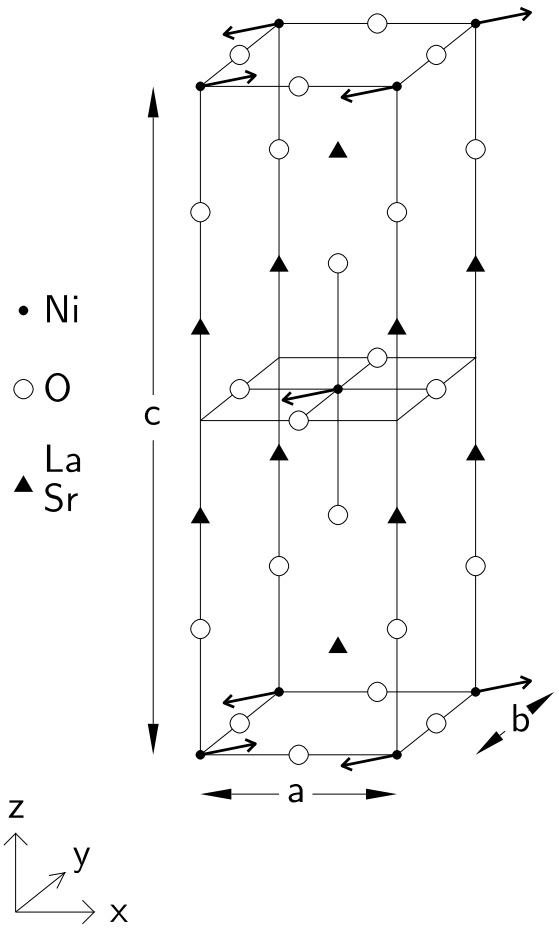

Figure 3.1: Structure [Frel91] of $La_{2-x}Sr_xNiO_4$. The nickel moments, symbolized by arrows, point along the $\langle 110 \rangle$ directions. The lattice parameters [Frel91] are a = b = 3.87 Å, c = 12.63 Å.

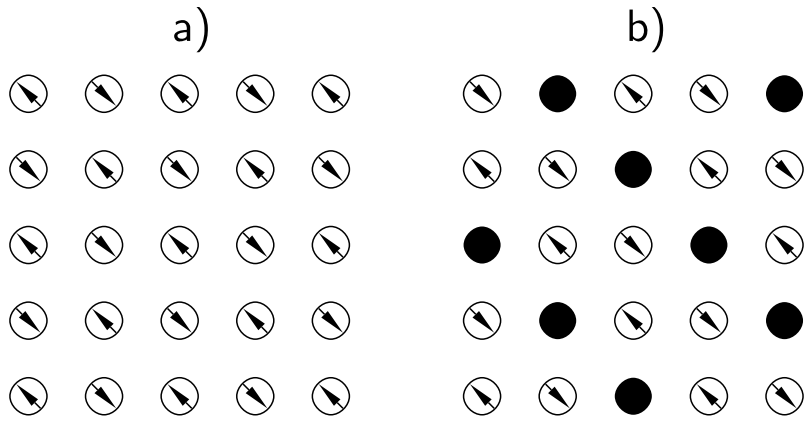

Figure 3.2: a) Idealized diagram of the antiferromagnetic ordering in the NiO_2 plane of the x = 0.00 compound. b) Idealized diagram of the spin stripe structure in the x = $\frac{1}{3}$ compound. In a) and b) only the Ni atoms are represented. Arrows indicate the orientation of the Ni spins, a circle without arrow represents a Ni atom with a hole. After [Tran95b].

In $La_2NiO_{4+\delta}$ magnetic order remains commensurate for $0 < \delta < 0.11$, although there is a pronounced variation of the magnetic transition temperature (T_M) with δ. For $\delta > 0.11$ both the oxygen interstitials and charge stripes order three dimensionally. Whereas a large number of articles have been published on the properties of $La_2NiO_{4+\delta}$ and $La_{2-x}Sr_xNiO_{4+\delta}$ with $x = 0.33$, less is known about the properties of the strontium doped materials for $x \neq 0.33$, especially for large x. Anomalies in the magnetic susceptibility and resistivity have been reported [Tavi91, Chen93, Cheo94] for $x = \frac{1}{3}$ and $\frac{1}{2}$. Hole ordering in the Ni-O planes, perhaps enhanced by commensurability effects at these magic numbers [Chen93, Cheo94, Tran96], are believed to be responsible for this behaviour. Furthermore, a recent neutron scattering study [Lee97] of $La_{1.67}Sr_{0.33}NiO_4$ suggests that charge ordering is the driving force for magnetic ordering in this material.

3.2 Sample Preparation and Characterization

Table 3.1 lists the nineteen polycrystalline $La_{2-x}Sr_xNiO_{4+\delta}$ samples that were investigated, including six samples on which earlier μSR measurements were performed [Chow96a]. The samples studied were prepared by M. Green and J. Millburn at the Oxford University Inorganic Chemistry Laboratory as follows: stoi-

x	δ	T_M(K)
0.00	0.009(4)*	335 ± 5
0.15	0.01(1)	28 ± 9
0.20	0.08(1)	133 ± 14
0.20	0.052(3)*	125 ± 9
0.25†	0.090	119 ± 6
0.33†	0.09(1)	180 ± 7
0.33	0.010(4)*	207 ± 2
0.33	0.08(1)	204 ± 9
0.40†	0.08(1)	118 ± 13
0.40	0.06(1)	131 ± 7
0.40	0.008(3)*	107 ± 5
0.50†	0.065(3)*	73 ± 10
0.50	0.006(4)	53 ± 10
0.60†	0.095(4)*	67 ± 5
0.60	0.01(1)	75 ± 2
0.80	0.05(1)*	80 ± 8
1.00†	0.063(4)*	44 ± 14
1.00	0.02(1)	49 ± 5
1.00	0.007(3)*	42 ± 5

Table 3.1: Polycrystalline $La_{2-x}Sr_xNiO_{4+\delta}$ samples studied and magnetic transition temperatures T_M obtained from μSR measurements. The superscript † indicates data from [Chow96a]. The superscript * indicates determination of the oxygen content by thermogravimetric analysis (TGA) and iodometry (the oxygen content in the remaining samples was obtained using TGA only).

chiometric quantities of $SrCO_3$, La_2O_3 (dried at 800 °C) and nickel powder were dissolved in 150 ml of dilute nitric acid. Citric acid and ethylene glycol were added and the mixture was heated, while stirring, to evaporate the solution. The resulting gel was decomposed at 350 °C overnight and the powder produced was refired at 800 °C in air, made into pellets and refired at temperatures between 1250 °C and 1450 °C in O_2 for an average of 10 days with several intermittent regrindings. Samples with a low oxygen doping were prepared by annealing in an N_2 atmosphere with 10% H_2 at $\sim$ 300 °C for 6 hours. The phase purity of all samples was confirmed using X-ray powder diffraction. The oxygen content of the samples was determined by thermogravimetric analysis under 8% H_2 in N_2. Some of the samples were also characterized by iodometry (see Table 3.1).

3.3 Experimental Aspects

All the samples were measured at the EMU and MuSR beamlines at ISIS (U.K.) to determine the temperature dependence of the initial decay asymmetry and the high temperature relaxation rates. In addition, selected samples were investigated at the πM3 and μE1 beamlines at PSI (Switzerland). As discussed in Chapter 2.2, PSI is a continuous-source muon facility while ISIS provides a pulsed beam of muons with a half width at half maximum of 70 ns. In the magnetically ordered state there is a strong internal magnetic field at the muon site ($\approx$ 220 mT $\equiv$ 40 MHz). The occurrence of coherent oscillations in the asymmetry function could be directly observed in the PSI data. The ISIS data provide only indirect evidence for the magnetic transition through the loss of initial asymmetry, see Chapter 2.4.3.

In the majority of the experiments $P_z(t)$ was monitored with no external field applied, so it reflects the interaction of the implanted muon with the internal magnetic field (ZF μSR). The earth's magnetic field was compensated to better than 10 μT. Longitudinal-field (LF) measurements were also performed on some of the samples. In the experiments polycrystalline samples of a typical mass of 2 g were packed in a silver foil (thickness 25 μm) pocket with typical dimensions of 20 mm $\times$ 17 mm $\times$ 2 mm. The contribution of the silver to the muon signal is accounted for by adding a constant term to $P_z(t)$ in the fitting procedure, see Chapter 2.4.3. For the experiments a variety of cryostats were used (Closed Cycle Refrigerator, He fridge). The samples were mounted on a silver backing plate in the cryostat and fixed with low temperature (kapton) tape. For better thermal conductivity vacuum grease was used. In each case the temperature was monitored with a thermometer on the back of the backing plate.

3.4 Experimental Results and Discussion

In this section I begin by describing the general features of the data. Then, in various subsections particular aspects are elaborated on and their physical significance is discussed in more detail.

There are two distinct temperature regimes in all the samples we have examined. In the ISIS experiments the following results were obtained: At temperatures above the magnetic transition temperature T_M, $P_z(t)$ is well-described by

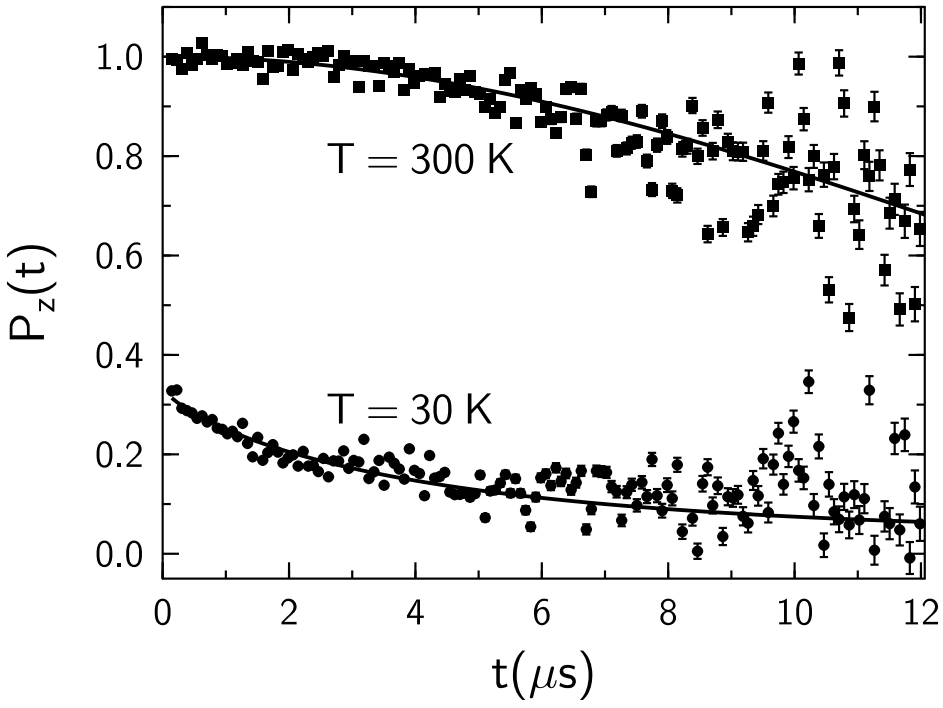

Figure 3.3: Time dependence of the muon decay asymmetry for the $La_{2-x}Sr_xNiO_{4+\delta}$, $x = 0.60$, $\delta = 0.01$ sample, shown for T = 300 K and T = 30 K. Note the distinct Gaussian character at the higher temperature and the exponential character at the lower temperature.

a Gaussian function $Ae^{-\sigma^2 t^2}$. However, when $T < T_M$ there is a marked decrease in the apparent initial amplitude as well as a change in the lineshape to a more exponential character, see Figure 3.3. The decrease in the observed asymmetry is due to a fast-relaxing and/or a high-frequency component which cannot, as discussed in Chapter 3.3, be resolved at ISIS. This results in an apparent missing fraction in the data below T_M since fast oscillations and/or fast relaxations will be averaged to zero. By contrast, for each of our samples the fast oscillations were resolvable at PSI. This is illustrated in Figure 3.4 for two of the samples.

I fitted the data to a modified version of Equation 2.19:

$$P_z(t) = G_{\parallel}(t) + G_{\perp}(t)\cos(\omega_\mu t)\ . \tag{3.1}$$

The following phenomenological functions are assumed in order to model the

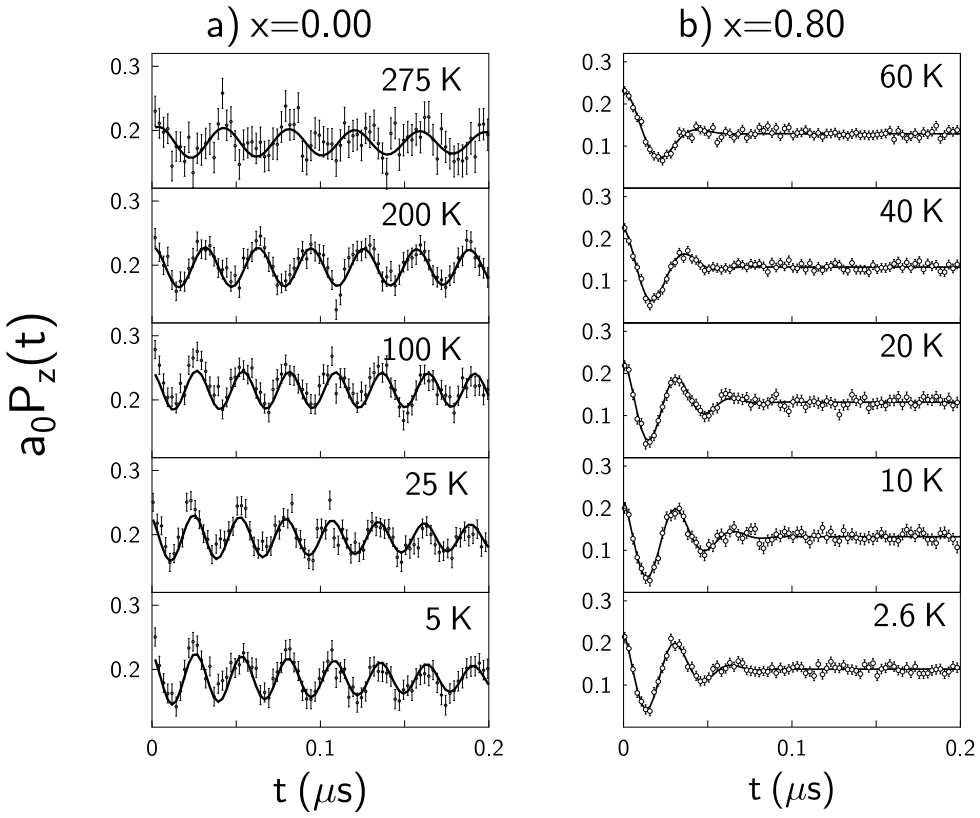

Figure 3.4: Time dependence of the muon decay asymmetry for $La_{2-x}Sr_xNiO_{4+\delta}$ (see Table 3.1). a_0 is a calibration factor, see Chapter 2.1.3. a) The short time behaviour for x = 0.00, showing fast, relatively long-lived coherent precession and b) the short time behaviour for x = 0.80, showing damped coherent precession. The smaller error bars in b) result from higher counting statistics.

zero-frequency component and the rapid decay of the oscillations:

$$G_{\parallel}(t) = a\exp(-\lambda_{\parallel}t) \tag{3.2}$$

$$G_{\perp}(t) = b\exp(-\lambda_{\perp}t). \tag{3.3}$$

A constant non-relaxing term is also added to model the polarization of muons which miss the sample and stop in the silver backing plate. In all the samples measured at PSI clear single frequency oscillations in zero applied field were observed (see Figure 3.4), except in the almost stoichiometric sample ($x = 0.00$, $\delta = 0.009$, see Table 3.1) where we find *two* oscillatory signals. This is in agree-

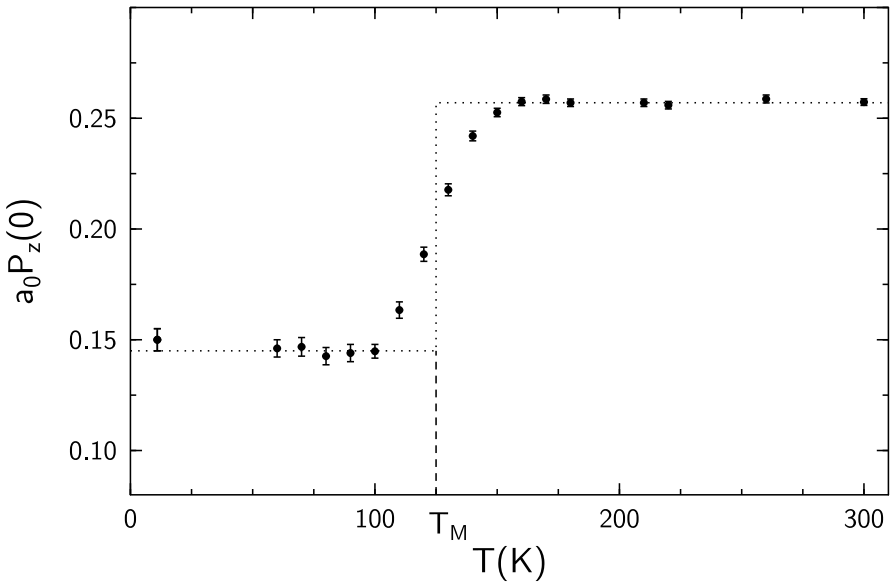

Figure 3.5: Initial muon decay asymmetry for the x = 0.20, $\delta = 0.052(3)$ sample (see Table 3.1), as measured at ISIS. The magnetic transition temperature T_M is indicated (see text). a_0 is a calibration factor, see Chapter 2.1.3.

ment with [Mart92]. The second *low* frequency signal can also be seen in the ISIS data for temperatures above ≈ 100 K. In Chapter 3.4.4 below we discuss how we can associate the frequencies with particular muon sites within the crystal.

The magnetic transition temperature T_M for each of the samples is listed in Table 3.1 on page 40. This quantity is estimated by studying the temperature dependence of the zero-field initial amplitudes using a coarse binning of the data. We define T_M as the temperature corresponding to 0.5Δ and the lower and upper bounds for T_M as the temperatures corresponding to 0.2Δ and 0.8Δ, where Δ is the change in the initial amplitude between the high and low temperatures. Figure 3.5 shows a typical result.

3.4.1 Magnetic Order in Samples

As mentioned above, in all samples coherent precession in zero applied field is observed below T_M. This implies that at a particular temperature below T_M the muon senses an internal magnetic field of essentially constant magnitude which

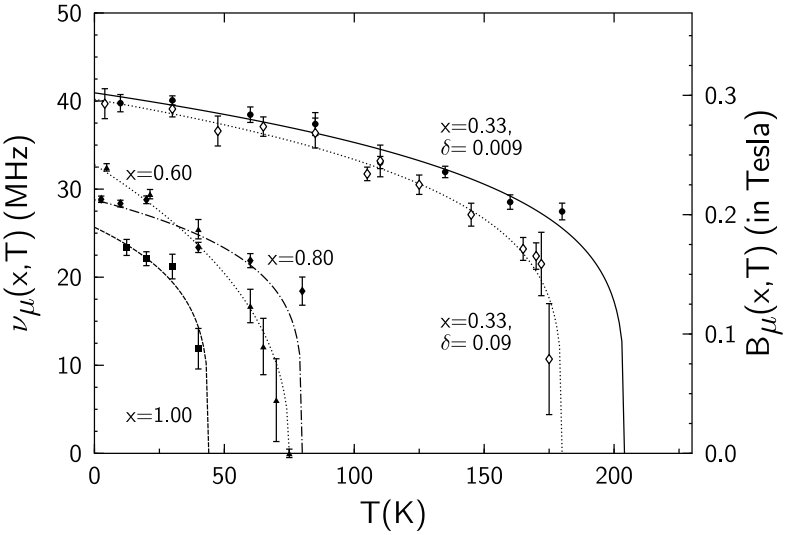

Figure 3.6: Temperature dependence of muon precession frequencies and internal magnetic fields in $La_{2-x}Sr_xNiO_{4+\delta}$ for various x-values. The lines are the fitting functions $\nu_\mu(x,T) = \nu_\mu(x,\ 0\ K)\ \{1 - T/T_M(x)\}^{\beta(x)}$.

is either static or quasistatic on a timescale of the order of microseconds. The Larmor frequency $\nu_\mu(x,T)$ of the oscillations is proportional to the magnetic field $B_\mu(x,T)$ at the muon site,

$$\nu_\mu(x,T) = \frac{\omega_\mu}{2\pi} = \frac{\gamma_\mu}{2\pi} B_\mu(x,T)\ , \tag{3.4}$$

and hence to the staggered magnetization $M^\dagger(x,T)$. We attribute the source of the internal field to the ordered nickel moments in the vicinity of the muon.

Some authors have suggested on the basis of magnetic susceptibility measurements that $La_{2-x}Sr_xNiO_{4+\delta}$ might have a spin glass ground state [Land91, Stra91]. In a spin glass the muons would see a very broad distribution of local magnetic fields, leading to a noncoherent precession [Uemu85]. Such a behaviour is not found in our experiments. We can therefore conclude that the samples do not show spin-glass behaviour but cannot rule out the possibility that there is a small fraction of each sample ($< 5\%$) that might exhibit spin glass behaviour which dominates the magnetic susceptibility, but because of its low volume fraction is unobservable in μSR.

Figure 3.6 shows the temperature dependence of $\nu_\mu(x,T)$ for several different

x	δ	β
0.33	0.009	0.22(2)
0.33	0.08	0.22(1)
0.60	0.01	0.43(4)
0.80	0.05	0.22(2)
1.00	0.007	0.24(4)

Table 3.2: Fitted β values for various doping levels to the function $\nu_\mu(x,T) = \nu_\mu(x, 0\ K)\ \{1 - T/T_M(x)\}^{\beta(x)}$ using the values of T_M listed in Table 3.1.

doping levels. A fit of the data to the function

$$\nu_\mu(x,T) = \nu_\mu(x, 0\ \mathrm{K}) \times \left(1 - \frac{T}{T_M(x)}\right)^{\beta(x)} \tag{3.5}$$

using the values of T_M listed in Table 3.1 yields a value of $\beta(x)$ of 0.22 ± 0.02 and 0.22 ± 0.01 for the $x = 0.33$ samples ($\delta = 0.009$ and 0.08, respectively), 0.22 ± 0.02 for $x = 0.80$, 0.24 ± 0.04 for $x = 1.0$ and 0.43 ± 0.04 for $x = 0.60$, see also Table 3.2.

Our functional form of $\nu_\mu(x,T)$ (Equation 3.5) gives a good description of the data over the complete temperature range. Theoretical values of the exponent β for 3D Heisenberg, XY and Ising systems are 0.38, 0.33 and 0.31, respectively [Ma76], while the value for a 2D XY model [Bram93] is 0.23, consistent with values found in other 2D magnetic systems [deJo74, Bors95]. The values of β for most of the samples are close to the theoretical value for 2D XY systems, and are consistent with the two-dimensional character of these materials even though the functional form used is normally only expected to be applicable to a small range below the temperature of the phase transition. The $x = 0.60$ sample shows a qualitative difference of the temperature dependence from the other samples. The reason for this difference in behaviour for this composition is not clear at present.

It is notable that magnetic order persists in these samples to much higher hole concentrations than in $La_{2-x}Sr_xCuO_{4+\delta}$ [Dago94]. This is consistent with the suggestion [Bors95] that mobile holes are more effective in destroying the exchange interaction giving rise to magnetic order than less mobile holes [Cava91]. The holes in $La_{2-x}Sr_xNiO_{4+\delta}$ have a greater $3d$-character compared to those in

$La_{2-x}Sr_xCuO_{4+\delta}$ and are therefore expected to be less mobile. The existence of less mobile holes is also consistent with the much higher Sr doping concentration needed to induce metallic conductivity in $La_{2-x}Sr_xNiO_{4+\delta}$ (see [Cava91] and below).

Figure 3.7 shows the doping dependence of the Larmor frequency $\nu_\mu(x, T = 0\text{ K})$ extrapolated to $T = 0$ K. The data set (excluding the $x = 0.33$ points) is fitted to the phenomenological function [Bors95]

$$\nu_\mu(x, T = 0\text{ K}) \;=\; \nu_\mu(x = 0, T = 0\text{ K}) \times \left(1 - \frac{x}{x_c}\right)^n , \qquad (3.6)$$

and as best fit we get $x_c = 1.02$ and $n = 0.113$. Reasonable fits can also be obtained for values $1.02 \leq x_c \lesssim 1.08$, see Figure 3.7. The parameter x_c can be interpreted as the doping level where the magnetic order is lost and a phase transition to a metallic state occurs. The estimate of x_c is consistent with the value $x_c \approx 1$ determined by an NMR study [Furu96]. Note also that the values of ν_μ in the less heavily-doped samples are close to the high frequency precession in the undoped material (Figure 3.4 a)). This implies that the *average* local field detected by the muon is similar in the doped and the parent material, a result which was also found [Hars88] in lightly-doped $La_{2-x}Sr_xCuO_4$. However, there is a peak in the frequency in $x = 0.33$. Such behaviour is qualitatively consistent with a higher localization of the holes at this concentration alluded to in the introduction.

Reference [Bors95] proposed a model for weakly doped $La_{2-x}Sr_xCuO_4$ below T_N in which carrier-rich domain walls are formed, separating undoped spin-rich domains, and that these walls effectively reduce the dimensionality of the spin-rich regions in the Cu-O planes. The holes are in motion along the direction of the domain walls, and in this they isolate the spin-rich domains from one another. This model, presented to explain the anomalous low temperature rise in the local magnetic field seen by the muon in $La_{2-x}Sr_xCuO_4$, suggests that the effective size of the magnetic domains determines both the local staggered magnetization and the transition temperature T_M. In particular, both these quantities decrease with decreasing domain size. Within the context of this model, we can visualize that in $La_{2-x}Sr_xNiO_4$ samples where $x \neq 0.33$, the holes act like "flowing rivers" of charge which form walls in the Ni-O planes separating undoped AFM domains. However, at $x = 0.33$, the holes are more localized and this leads to larger effective domain sizes and hence a corresponding increase in the local staggered magnetization.

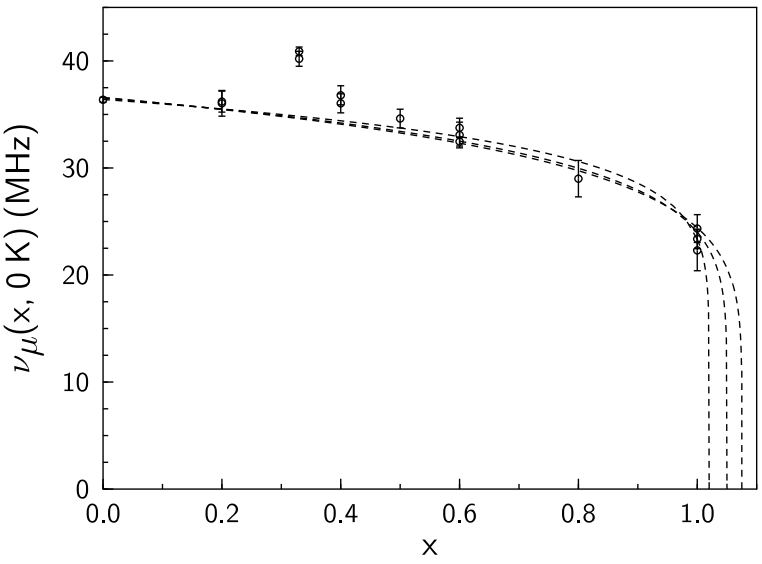

Figure 3.7: Low temperature (5 – 10 K) Larmor frequency vs. doping level x (see text). Note the peak at x = 0.33. We also display a range of reasonable fits to the phenomenological function ν_μ(x, T = 0 K) = ν_μ(x = 0, T = 0 K) × (1 - x/x_c)^n, with (x_c, n) = (1.02, 0.113), (1.05, 0.138) and (1.075, 0.152).

Note that this model also predicts the existence of a peak in T_M, an issue that I will return to in section 3.4.3.

3.4.2 Static and Dynamic Nature of the Nickel Spins

I now discuss the damping rates $\lambda_\perp$ of the oscillating signals as well as $\lambda_\parallel$ (see Equations 3.3 and 3.2, respectively). The implications of these results will be discussed in the context of a previous μSR study [Chow96a] of polycrystalline $La_{2-x}Sr_xNiO_4$ as well as neutron measurements in nickelates with lower hole doping levels [Sach95, Tran94a, Tran95a]. These show evidence for stripe spin and hole order, a phase which is quite different from the Néel state of the parent material [Aepp88]. The observation that $\lambda_\perp \gg \lambda_\parallel$ for all x, as shown in Figure 3.8, indicates that the relaxation of the oscillations is dominated by the *static* distribution of the neighboring Ni spins. Nevertheless, some *dynamic* broadening, i.e. fluctuations of the Ni spins, is undoubtedly present since $\lambda_\parallel$ is nonzero.

The large values of $\lambda_\perp$ indicate that there is a significant inhomogeneity in the local spin structure around the muon. This broadening ranges from $\lambda_\perp(x, T \to 0\ \mathrm{K})/(2\pi\nu_\mu(x, T \to 0\ \mathrm{K})) = 1.8\ \%$ in the $x = 0.00$, $\delta = 0.009$ sample to ≈ 28.2

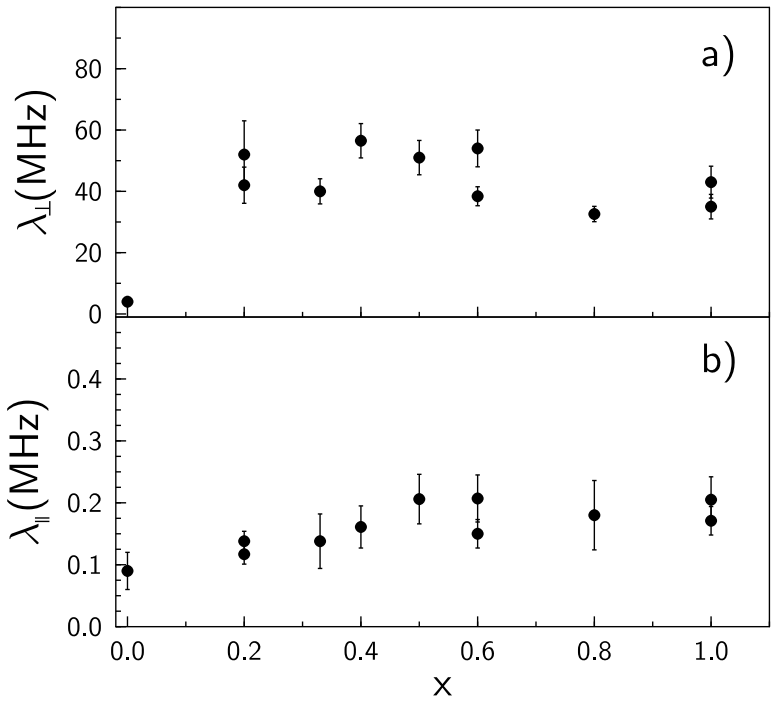

Figure 3.8: a) Low temperature damping rate $\lambda_\perp$ as a function of x. b) Low temperature damping rate $\lambda_\parallel$ as a function of x.

% in the $x = 1.00$, $\delta = 0.00$ sample. Such inhomogeneities might arise from the formation of stripe phases; however, the muon is not sensitive to the details of this local spin structure, as evidenced by the nearly constant $\lambda_\perp$ for $x \neq 0$. No clear correlation is seen between stripe formation at the "special" doping value of x=0.33 and $\lambda_\perp$. The spin fluctuation rates are significantly less than $\gamma_\mu B_\mu$ since coherent precession is observed, implying that the correlation time of the nickel spins is longer than 10^{-8} s at low temperatures ($\approx$ 5 K). In this context it is interesting to note that in a sample with $x = 0.2$ (δ not measured) the magnetic correlation time for correlated regions (stripes) was found by neutron scattering [Hayd92] to be longer than $\sim 10^{-11}$ s at 2 K and of the order of $\sim 10^{-12}$ s at 80 K.

The source of the muon relaxation for $T \gg T_M$ can be attributed to *nuclear* dipolar fields, as suggested in [Chow96a]. In the present study this could be confirmed for a number of samples by the observation that a weak longitudinal field of $\approx$ 10 mT is sufficient to quench the relaxation, *i.e.* $P_z(t)$ is almost constant. This was checked in the $x = 0.25$, $x = 0.33$, $x = 0.40$, $x = 0.50$ and $x = 1.00$ samples. The nuclei responsible for the relaxation are likely to be ^{139}La, the most

Isotope	Natural Abundance (%)	Nuclear Spin	Nuclear Magnetic Moment
^{138}La	0.089	5	3.707 μ_N
^{139}La	99.911	7/2	2.783 μ_N
^{84}Sr	0.056(1)	0	
^{86}Sr	9.86(1)	0	
^{87}Sr	7.00(1)	9/2	-1.094 μ_N
^{88}Sr	82.58(1)	0	
^{58}Ni	68.007(9)	0	
^{60}Ni	26.223(8)	0	
^{61}Ni	1.140(1)	3/2	-0.750 μ_N
^{62}Ni	3.634(2)	0	
^{64}Ni	0.926(1)	0	
^{16}O	99.762(15)	0	
^{17}O	0.038(3)	5/2	-1.894 μ_N
^{18}O	0.200(12)	0	

Table 3.3: Isotopes in $La_{2-x}Sr_xNiO_{4+\delta}$ and their properties, taken from [CRC95].

abundant species with non-zero nuclear spin (the natural abundances are ^{138}La 0.089% and ^{139}La 99.911%, the nuclear spin of ^{139}La is 7/2, see Table 3.3). In this high temperature range the fluctuation rate of the nickel moments is much higher than the Larmor frequency of the muon; hence, the Ni moments do not contribute significantly to the muon depolarization (motionally narrowed limit).

In the fast fluctuation limit in zero applied field the *exponential* relaxation rate above the magnetic transition is given by [Uemu85, Kere94]

$$\lambda = 2\gamma_\mu^2 B_{rms}^2 \tau \ , \tag{3.7}$$

see Equation 2.24. Here τ is the correlation time of the internal field and B_{rms} is the rms internal magnetic field at the muon site, assumed to be of the order of the average magnetic field sensed by the muons at the lowest temperatures. The exponential relaxation rate λ can be estimated from a short-time exponential fit to $P_z(t)$. This fit is valid since the Gaussian nuclear relaxation (see above) will be dominant only on a longer timescale. In addition, this was experimentally confirmed in some of the samples by applying a longitudinal field of between 5 mT and 10 mT. The Gaussian contribution disappears but the exponential part

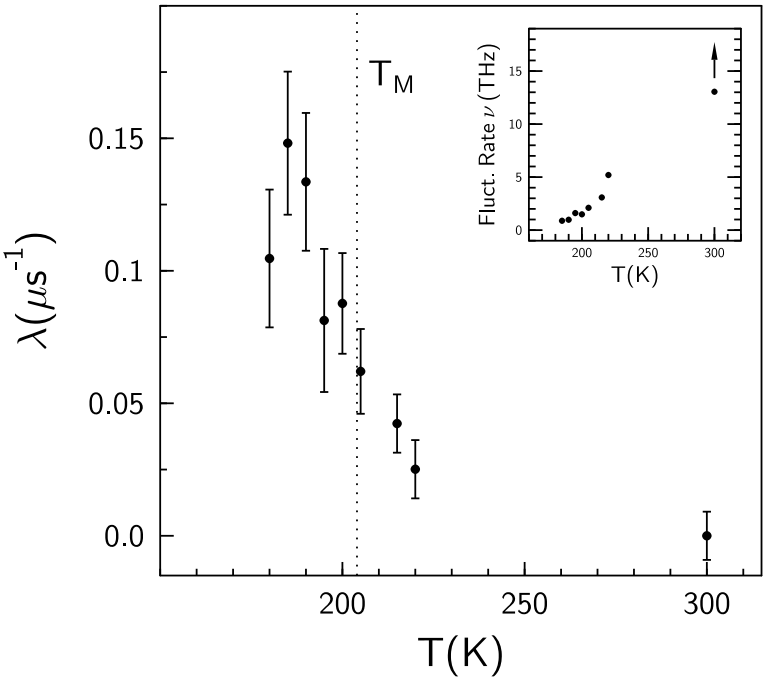

Figure 3.9: Exponential relaxation rate λ and spin fluctuation rate ν (inset) for the $La_{1.67}Sr_{0.33}NiO_{4.010}$ sample in zero magnetic field. The fluctuation rate is calculated in the fast fluctuation limit (see section 3.4.2).

remains the same within the error bars. A representative plot of the temperature dependence obtained from the relaxation rates is displayed in Figure 3.9. At 300 K the exponential relaxation rate λ is too close to zero to be measurable, see Figure 3.9. From this we can safely deduce that $\lambda \ll 0.01\ \mu s^{-1}$, and from Equation 3.7 one can estimate that the correlation time of the Ni spins is smaller than 10^{-13} s (shorter than reported in [Chow96a]). Note that the muon is not diffusing very rapidly on a microsecond timescale since a coherent precession is observed by μSR in stoichiometric La_2NiO_4 up to 335 K.

3.4.3 Phase Diagram of the magnetic transition

We now discuss the dependence of T_M on the strontium doping concentration. The measurements are summarized in Figure 3.10. The different T_M-values for a given x are associated with different values of δ, e.g. the three values of T_M represented for $x = 0.40$ correspond to $\delta = 0.08$, $\delta = 0.06$ and $\delta = 0.008$. The transition temperatures for a particular x are, however, very close to each other even though

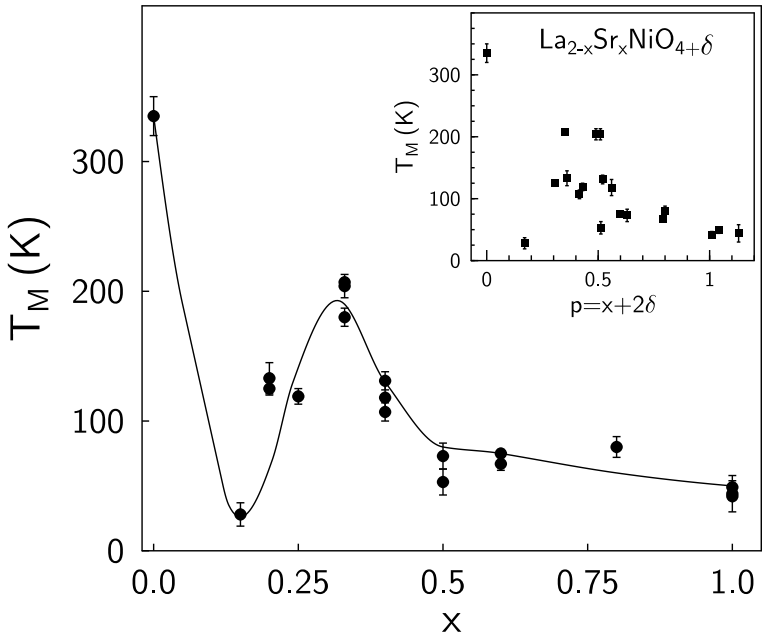

Figure 3.10: Phase diagram for $La_{2-x}Sr_xNiO_{4+\delta}$. Multiple entries for the same x-value are associated with different δ values (see Table 3.1). The solid line is a guide to the eye. The inset shows the same data set, plotted as a function of p=x+2δ. Clearly p is not the appropriate parameter for the characterization of the magnetic transition temperature.

δ is different in each case (see Table 3.1). Contrast this behaviour with the $x = 0$ material (see Figure 3.11, data taken from [Yama94, Naka97, Frel91, Tran93, Gopa92]), where a drastic initial drop in the magnetic transition temperature is seen with increasing δ. We find that T_M first drops with increasing x, reaches a minimum at $x \sim 0.15$, and then rises again to a maximum of ≈ 205 K for $x = 0.33$. For larger x the transition temperature again drops, falling to a value of about 45 K at the highest doping levels (Figure 3.10).

In [Chow96a] it was speculated that $p = x+2\delta$ might be the relevant parameter for controlling the magnetic transition temperature, following a suggestion based on neutron measurements [Sach95]. The current study, making use of many more samples, demonstrates that this appears to be incorrect for $La_{2-x}Sr_xNiO_{4+\delta}$ where $x \neq 0$ (see Table 3.1). This is particularly obvious from the inset in Figure 3.10 where there are a number of very different T_M values for a particular value of p. The interstitial accommodation of oxygen requires a local lattice distortion [Gopa92] while quite different structural consequences result from Sr substitution [Hean98]. Both these structural effects are likely to have significant, but dissimilar,

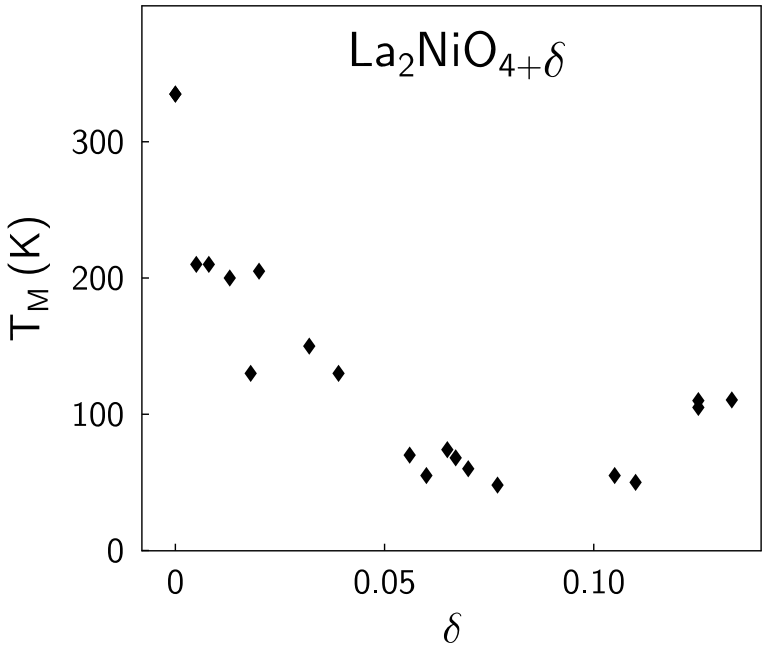

Figure 3.11: Dependence of the magnetic transition temperature on the oxygen doping in $La_2NiO_{4+\delta}$ (taken from references cited in the text). A similar sensitivity of the transition temperature to oxygen doping is not apparent in the strontium doped compounds that we have studied (see section 3.4.3).

effects on the magnetic properties even when the nominal hole concentration is identical.

Based on neutron scattering experiments, it has been suggested [Tran96] that spin stripe ordering is driven by charge ordering. The $x = 0.33$ doping has attracted much attention because it demonstrates pronounced charge ordering (at 239 K) [Tran96, Cheo94]. It is plausible that the loss of hole mobility is responsible for the pronounced increase in T_M (Figure 3.10) at this doping level. In view of the earlier discussion (Chapter 3.4.1) regarding the effects of the magnetic domain size on $\nu_\mu(x, T = 0 \text{ K})$, a peak in T_M is also expected and indeed observed at this special concentration. For $x = 0.5$, anomalies in bulk properties, e.g. resistivity [Cheo94], have previously been observed at higher temperatures ($\sim$ 340 K), but the features were much broader and weaker than those for $x = 0.33$. We find no evidence of another peak in T_M at this hole doping level.

3.4.4 Muon Site

In agreement with [Mart92] we find two distinct values of ν_μ in our $x = 0.00$ sample, which can be attributed to two muon sites. There is no indication of a second muon site for any of the Sr doped samples. In order to arrive at possible muon sites in $La_{2-x}Sr_xNiO_{4+\delta}$, I have performed dipole field calculations, analogous to those described in [Le90, Chow96b]. The local magnetic field $\mathbf{B}_\mu(\mathbf{r}_\mu)$ sensed by the muon is given by the sum of the dipolar field, $\mathbf{B}_{\rm dip}(\mathbf{r}_\mu)$, which is due to Ni moments and the hyperfine field, $\mathbf{B}_{\rm hf}(\mathbf{r}_\mu)$, which is due to any non-zero electron spin density at the muon site. Although we lack knowledge of the hyperfine coupling constant it is assumed to be small, as in the case of La_2CuO_4 (see [Le90]) and other magnetic oxides. With this assumption the magnetic field at the muon site can be calculated as a sum of dipolar contributions,

$$\mathbf{B}_\mu(\mathbf{r}_\mu) = \sum_i \frac{3(\boldsymbol{\mu}_i \cdot \mathbf{n}_i)\mathbf{n}_i - \boldsymbol{\mu}_i}{|\mathbf{r}_\mu - \mathbf{r}_i|^3} \quad , \tag{3.8}$$

where $\mathbf{r}_\mu$ is the position of the muon, $\boldsymbol{\mu}_i$ is the effective magnetic moment of the i-th nickel ion and $\mathbf{n}_i$ is the unit vector from the muon to the nickel ion at site $\mathbf{r}_i$. The magnetic moment $\boldsymbol{\mu}_i$ of La_2NiO_4 has been measured by neutron diffraction [Frel91, Tran93]. The values obtained in the two studies were 0.75 $\mu_{\rm B}$ and 0.85 $\mu_{\rm B}$, respectively. In our calculations we assumed the mean of those values, *i.e.* $|\boldsymbol{\mu}_i| = 0.80\ \mu_{\rm B}$. From Reference [Frel91] we have taken the lattice parameters (neglecting the small differences in the two lattice constants a and b) of $a = b = 3.87$ Å, $c = 12.63$ Å and the spin structure as shown in Figure 3.1. The sum in Equation 3.8 was evaluated numerically by taking into account nickel spins within a radius of $15a$ about $\mathbf{r}_\mu$.

In the Ni-O plane the field distribution is rather flat in the center of the plane but changes rapidly near the nickel sites (where the field diverges) and the oxygen sites (where the field is zero); see Figure 3.12. As one would expect, outside this plane the field is much smaller, and becomes smallest in the $z/c = 1/4$ plane (where the maximum value is $|\mathbf{B}| = 41$ mT).

Sites which are within 15 % of 260 mT were selected; this field value corresponds to the average high precession frequency observed in the nearly stoichiometric sample, $x = 0.0$, $\delta = 0.009$. The 15 % tolerance reflects the uncertainty in the magnetic moment from the neutron measurements. We find that the muon dis-

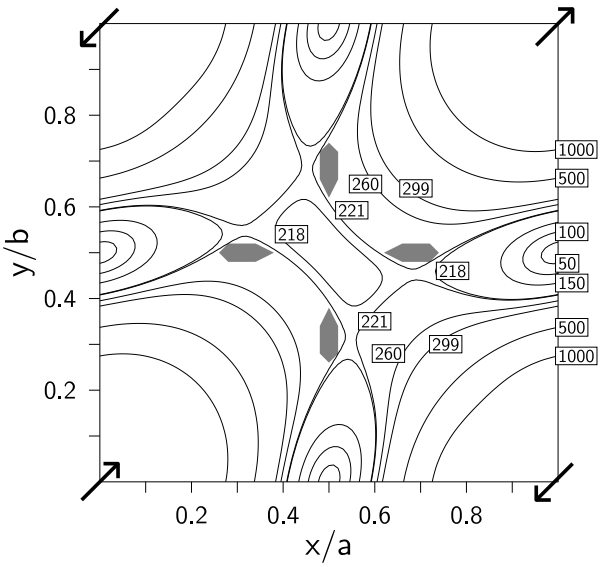

Figure 3.12: Contour plot of the dipole field in the z/c = 0 plane. The nickel moments are symbolized by arrows at the corners of the square. The shaded region corresponds to the muon positions compatible with the data. The magnetic field is given in mT.

tance to the Ni-O plane should be smaller than 1.3 Å. Restrictions can be imposed because crystallographically equivalent sites in the unit cell do not experience the same magnetic field (the field symmetry is reduced due to the spin structure), *i.e.* in general $|\mathbf{B}(x,y,z)| \neq |\mathbf{B}(x,b-y,z)|$. Assuming that the field distribution is less than 5 % of the mean value (given in section 3.4.2), the two possible sites in the Ni-O plane are

(1) $x/a = 0.4$, $y/b = 0$ (and equivalent sites) and

(2) those regions in Figure 3.12 which are shaded.

In a variety of μSR Experiments in oxides [Boek86, Daws90, Holz81, Nish90, Webe90] it has been shown that the μ^+ forms a covalent bond with an oxygen atom; the typical distance between the oxygen atom and the muon is 1.0 ± 0.1 Å. For case (1) the distance to the oxygen (at $x/a = 0.5$, $y/b = 0$) would be rather small compared to this typical O–μ bonding length of 1 Å. We conclude that within the magnetic dipole approximation, position (2) is the most likely muon site in the Ni-O plane. An analogous treatment for the second lower precession frequency in La_2NiO_4 leads to a range of possible second muon sites, some of which are consistent with the ones proposed for La_2CuO_4 [Le90].

3.5 Conclusion

In conclusion, magnetic order in $La_{2-x}Sr_xNiO_{4+\delta}$ was studied for a large number of samples where $0 \leq x \leq 1$ and demonstrated that local magnetic order exists in all samples below an x-dependent transition temperature T_M. This enabled us to probe the temperature dependence of the short-range order parameter in the samples and make estimates of the correlation times below and above the transition temperature. We have extended the information on magnetic transition temperatures to doping values other than those previously reported and particularly to higher values, and conclude that, in contrast to previous speculations [Sach95, Chow96a], the appropriate parameter for controlling the magnetic transition temperature for non-zero x is not $p = x + 2\delta$, but x itself. In light of the coherent precessions obtained in the experiments, the previous speculation [Land91, Stra91] that the ground state for these materials at higher strontium doping levels is a spin glass needs further exploration. We find evidence for an enhancement in T_M and the zero temperature staggered magnetization associated with doping at $x = \frac{1}{3}$ which may be connected with enhanced hole ordering.

Chapter 4

Magnetic Order and Spin Dynamics of the n=2 Ruddlesden-Popper Phases $Sr_2LnMn_2O_7$

Contents

Colossal magnetoresistance (CMR) materials, which show very large changes in resistivity on application of a magnetic field, may have possible applications as sensors in magnetic memory devices. Because of this, and because the basic physical understanding of the mechanism of CMR is not clear, much research on these materials continues.

In this chapter I describe muon spin relaxation measurements on a family of bilayer perovskites which contain lanthanide ions, some of whose members show very large CMR. The results will be interpreted in terms of the presence of fluctuating magnetic clusters that are found in the compounds which show CMR. Information is also extracted concerning the fluctuation of the lanthanide moments which often show an activated temperature dependence as sensed by the muon.

This chapter is arranged as follows. In section 4.1 I give a short overview of colossal magnetoresistance effects and other physical properties of various CMR materials which have been studied by muons. In section 4.2 I review the μSR work performed on CMR materials so far. Section 4.3 describes the sample preparation. In section 4.4 I describe details of the experimental procedures, and in section 4.5 I present the data obtained on the range of samples studied. The muon depolarization data are presented for the series going from the largest to the smallest lanthanide (with the exception of the Gd sample, for which the results are presented last). In the concluding section, 4.6, I give a short summary.

Parts of the material in this chapter have been submitted for publication [Bewl99].

4.1 Introduction: The Ruddlesden-Popper Manganates

Colossal magnetoresistance (CMR) in pseudocubic perovskites $Ln_{1-x}A_xMnO_3$ (A = Ca, Ba, Sr, Pb, Bi and Ln = Pr, Nd, Sm, Eu, Gd, Tb, and Dy) has attracted considerable attention in recent years [Rami97, Kust89, Helm93]. The magnetoresistivity $\Delta\rho/\rho$ is defined as

$$\frac{\Delta\rho}{\rho}(T,B) = \frac{\rho(T,0) - \rho(T,B)}{\rho(T,B)} \,, \tag{4.1}$$

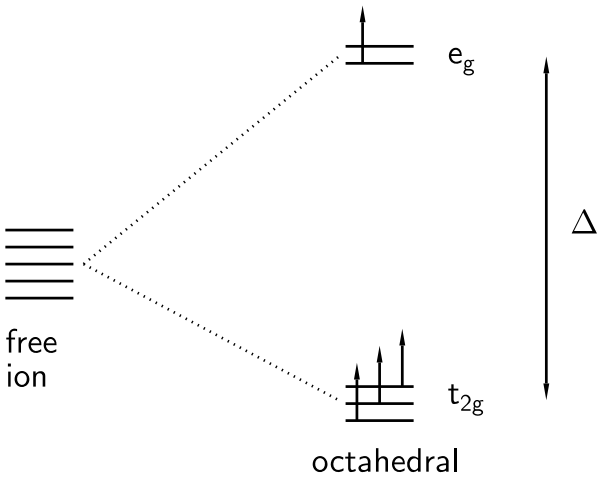

Figure 4.1: Crystal field splitting of the Mn 3d orbitals. Here I show an Mn^{3+} ion. In the double exchange mechanism, the e_g electron hops from an Mn^{3+} ion to an Mn^{4+} ion via the an oxygen orbital.

where B is the external applied field and ρ the specific resistivity. For example in $Pr_{0.7}Sr_{0.04}Ca_{0.26}MnO_{3-\delta}$ [Maig95] a value of $\Delta\rho/\rho$ of up to $10^{11}\%$ has been observed for $B = 5$ T at 30 K. The orthorhombic parent compound $LaMnO_3$ is an insulating antiferromagnet with 100% Mn^{3+} ions. It is possible to change the oxidation state of a fraction of the manganese ions to Mn^{4+} by replacing a fraction of the La^{3+} ions with doubly charged ions A^{2+} (see above). By doing so it is often found that the electrons become delocalized and a high temperature insulating paramagnetic phase gives way to a low temperature ferromagnetic metallic phase. The Curie temperature is then determined by the doping level x. The CMR effect occurs in a small temperature region near the Curie temperature. This shows that the spin alignment and the electrical transport are closely related. The coexistence of metallic conductivity and ferromagnetic coupling in these materials has been explained in terms of a double exchange (DE) mechanism [Zene51, Ande55, deGe60]. Octahedral crystal fields split the Mn $3d$ orbitals into two e_g orbitals, which are strongly hybridized with the oxygen p orbitals, and three lower energy t_{2g} orbitals, which are more localized, see Figure 4.1. The DE mechanism requires a mixed valence state of Mn^{3+} and Mn^{4+} cations in which the e_g electrons hop from a Mn^{3+} to a Mn^{4+} via the oxygen orbitals. In this process the e_g electrons retain their spin direction and therefore tend to align the spins of neighbouring Mn ions

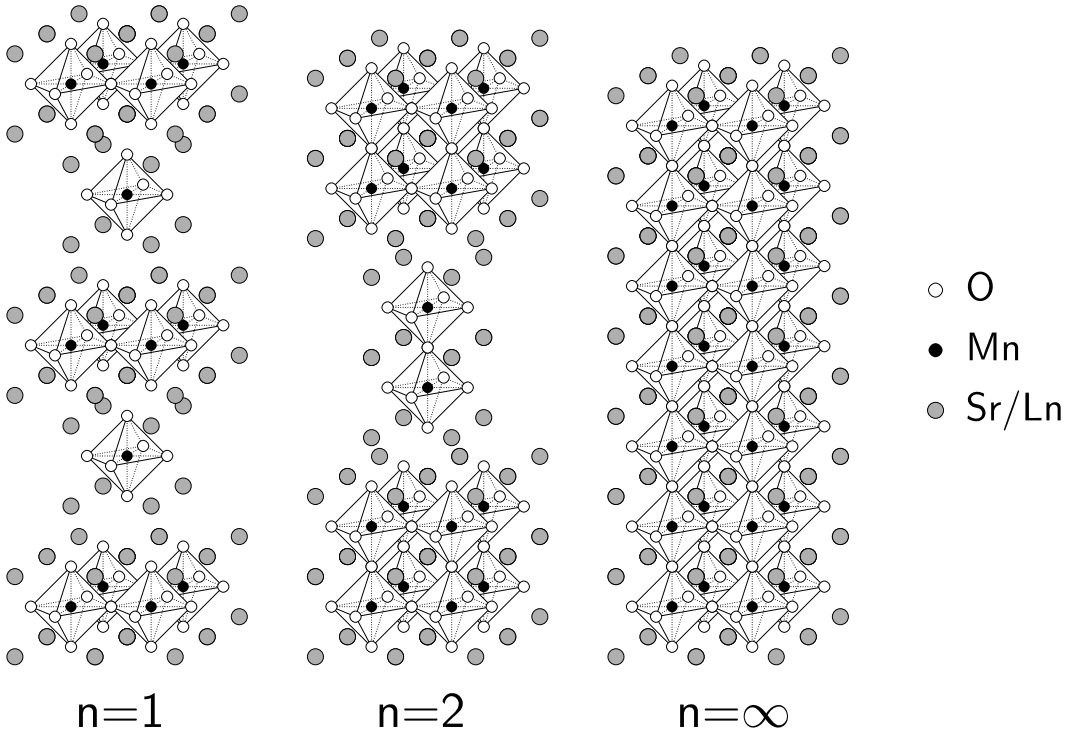

Figure 4.2: Structure of the Ruddlesden-Popper compounds $(Sr,Ln)_{n+1}Mn_nO_{3n+1}$. For n = 2 we get the structure of the $Sr_2LnMn_2O_7$, whereas n = ∞ corresponds to the perovskites, and n = 1 produces the K_2NiF_4 structure (see also Chapter 3 and Figure 3.1).

due to a strong Hund's rule coupling [Tere97]. Recent work shows that the DE mechanism on its own greatly overestimates both the conductivity and T_C and is not enough to explain CMR in these materials, and that it is necessary to include the dynamical Jahn-Teller effect [Mill95, Röde96, Mill96, Shen97].

More recently, CMR has also been observed [Mori96, Batt96a, Sesh96] in the $n = 2$ Ruddlesden-Popper (RP) phases [Rudd58]. The RP phases $(Sr,Ln)_{n+1}Mn_nO_{3n+1}$ can be thought of as stacks of perovskite blocks n layers thick with each block separated by a rock-salt $(Sr,Ln)_2O_2$ layer which decouples the blocks electrically and magnetically, see Figure 4.2. The perovskite compounds are realized for $n = \infty$, whereas the case $n = 1$ is equivalent to the K_2NiF_4 structure (see also Chapter 3). The structural consequences of moving from perovskite $n = \infty$ to the $n = 2$ RP phases is the introduction of a two-dimensional character and a reduction from 6 to 5 in the number of nearest neighbour Mn cations

around a particular transition metal site. The reduction in the number of nearest-neighbours is expected to produce an anisotropic reduction in the width of the energy bands derived (largely) from the Mn $3d$ orbitals, and hence is expected to modify the electrical conductivity and magnetic behaviour of these materials. All the samples of the $Sr_2LnMn_2O_7$ series have the same mean value of Mn oxidation state of +3.5, i.e. an equal number of Mn^{3+} to Mn^{4+} ions. However, the exchange coupling between Mn ions is very sensitive to the Mn-O bond angles. In crossing the lanthanide series from left to right, the size of the rare-earth ion decreases (the lanthanide contraction), thus creating a distortion in the MnO_6 octahedra. This can weaken the (ferromagnetic) double exchange coupling between Mn ions and can introduce magnetic frustration because of the competing ferromagnetic and antiferomagnetic superexchange interactions. As magnetization [Batt96a, Batt96b, Batt97a] and resistivity [Batt96a, Batt97a] measurements have shown, the physical properties of these samples depend on the lanthanide ion, an effect which has also been observed in the perovskites [Rami97].

However, the electrical and magnetic behaviour of some of the $n = 2$ RP phases is very different from their $n = \infty$ counterparts. Although $Sr_{2-x}Nd_{1+x}Mn_2O_7$, for example, shows [Batt96a] an enhanced CMR over a very wide temperature range 4 K $< T <$ 150 K for $x = 0.0$ and $x = 0.1$, it is non-metallic and there is no evidence of ferromagnetic ordering [Batt96b]. The lack of long range magnetic ordering and the reduced temperature of the CMR effects in these samples compared to the perovskites can be attributed to the reduced dimensionality of these systems and the resulting increase in the magnetic fluctuations. However, with no ferromagnetic ordering and non-metallic behaviour it is difficult to understand how the DE mechanism applies in these compounds, thus placing new constraints on the development of microscopic models. It is clearly important to understand the nature of the CMR in this material and other similar $n = 2$ RP compounds and this requires a knowledge of the magnetic state and magnetic fluctuations within these materials.

4.2 CMR Materials and muon spin spectroscopy

μSR has been used by other authors to investigate the magnetic properties of CMR compounds. De Teresa [Tere97] *et al.* have investigated the behaviour of $(La_{1-x}Tb_x)_{2/3}Ca_{1/3}MnO_3$ for $x = 0.33$ with small angle neutron scattering and

μSR. This compound is insulating and shows a decrease of eleven orders of magnitude in the resistance under an applied magnetic field of 12 T around 80 K. The neutron experiments found that small ferromagnetic clusters exist for the $x = 0.33$ compound, with a typical cluster size of around 18 Å at low temperatures. Muon spin relaxation experiments confirmed the absence of magnetic order and gave evidence for the existence of a spin-glass transition at $T_{sg} \approx 45$ K. The muon data were fitted with a stretched exponential function (see Equation 2.25), and a divergence in the relaxation rate was found, which describes the critical slowing down of the spin dynamics as the freezing of the local magnetic field is approached. For this compound, the magnetic coherence length increases monotonically with decreasing temperature, but there is no long-range ferromagnetic order. The muon data showed a strong variation of the parameter β (see Equation 2.25) below 125 K, well above T_{sg}, which approaches the value of ≈ 0.5 at T_{sg}. At high temperatures the relaxation was slow, and the values of β were close to unity.

The low temperature muon spin relaxation mechanism in this material which is dominated by randomly orientated frozen local fields, coexisting with residual spin fluctuations, differs strongly from the low-temperature depolarization observed in the metallic and 3D ferromagnetic $La_{0.67}Ca_{0.33}MnO_3$ [Heff96, Heff97]. In the paramagnetic high temperature region there are, however, similarities.

In $La_{0.67}Ca_{0.33}MnO_3$, Heffner *et al.* [Heff96, Heff97] observed a phase transition from a paramagnetic state to a ferromagnetic ground state. They fitted the data with the relaxation function

$$P_z(t) = A_1 e^{-\lambda_1 t} \cos(2\pi\nu_\mu t + \phi) + A_2 e^{-(\lambda_2 t)^\beta} \ . \qquad (4.2)$$

Here ν_μ is the muon spin precession frequency, proportional to the sublattice magnetization below the ferromagnetic transition temperature T_C. $A_1 + A_2 = 1$, λ_1 is the inhomogeneous linewidth and λ_2 is the dynamic spin-lattice relaxation rate. Below T_C the sublattice magnetization was proportional to $(1-T/T_C)^\gamma$ with $T_C = 274$ K and $\gamma = 0.345(15)$, which is characteristic of a phase transition for a 3D spin system (see also Chapter 3.4.1). There was no evidence for multiple muon stopping sites. They found that $\lambda_1/2\pi\nu_\mu \approx 1/3$ at 10 K. The dynamical relaxation changed from an exponential form (i.e. $\beta = 1$ in Equation 4.2) to a root-exponential (i.e. $\beta = 1/2$) at $T \approx T_C$, signifying a broad distribution of relaxation

times. The slow and inhomogeneous spin dynamics below T_C was interpreted as the signature of small magnetoelastic polarons, i.e. variable-size spin-clusters below T_C. Above the phase transition temperature $A_1 = 0$, while below T_C A_1 increased to the maximum value of $\approx 2/3$ at $T \leq 0.84T_C$. This growing of the local static spin correlations indicates that the microscopic spin freezing percolates over an extended temperature range, which was connected to "some kind of glassy state".

For the $n = 2$ compound $Sr_{1.6}La_{1.4}Mn_2O_7$, Heffner *et al.* [Heff98] reported on experiments on single crystals. Using again Equation 4.2 they found a spatially inhomogeneous relaxation rate λ_2 below the magnetic transition temperature $T_C \approx 80$ K, while it was anisotropic above T_C. They found evidence against in-plane correlations above T_C. Below T_C they observed coherent muon-spin precessions, but the order parameter was not a smooth function of temperature, which was attributed to competing magnetic ground states.

Comparison of the $n = \infty$ [Heff96, Heff97] and $n = 2$ [Heff98] material showed that in the layered material the spin lattice relaxation drops abruptly to nearly zero within a few degrees below T_C and there was no indication of the slow dynamics as was observed in the 3D perovskites. This difference was attributed to a larger cluster size in the $n = 2$ material. The lower $T_C \approx 80$ K in the layered material was attributed to the reduced dimensionality.

The last attribution, though valid in general, might not be applicable since Heffner *et al.* were dealing with $n = \infty$ and $n = 2$ materials with different constituents. As we have seen above and as we shall see below, different dopants can have quite dissimilar effects on the physical properties of the systems investigated.

4.3 Sample Preparation

The preparation and characterization procedures of the compounds described below were reported in more detail in [Batt97b]. All the samples were prepared by M. Green and J. Millburn in the Inorganic Chemistry Laboratory, Oxford. They were synthesized by a solid state reaction of stoichiometric quantities of $SrCO_3$, MnO_2 and Ln_2O_3, where Ln = Pr, Nd, Sm, Eu, Gd, Tb, Dy and Ho. The lanthanide oxides had first been dried in a muffle furnace at 800 °C. The reaction mixtures were calcined at 800 °C, 1000 °C and 1200 °C for 24 hours and then ground and formed into a pellet. Subsequently, they were heated in air at

1350 °C for 225 hours (Ln = Pr), 400 hours (Ln = Sm), 300 hours (Ln = Eu, Ho), 200 hours (Ln = Gd, Tb), 250 hours (Ln = Dy) or at 1300 °C for 120 hours (Ln = Nd). The progress of the synthesis was monitored after every firing stage by X-ray powder diffraction using a Phillips PW1710 powder diffractometer with a secondary graphite monochromator. X-ray powder diffraction data for structure analysis were collected with a Siemens D5000 diffractometer, using Cu Kα1 radiation.

4.4 Experimental Details

The experiments were performed on the EMU, MuSR and ARGUS beamlines at the ISIS facility and the πM3 beamline at the PSI facility. All the experiments were performed in zero applied field. The earth's magnetic field was compensated to better than 10 μT.

The cryostats used were a Closed Cycle Refrigerator and Helium fridges. In the experiments, polycrystalline samples of typical mass 1-2 g were wrapped in a 25 μm silver foil (with typical target dimensions of 20 mm $\times$ 17 mm $\times$ 2 mm). The samples were mounted on a silver backing plate in the cryostat and fixed with kapton tape. As mentioned before, silver is used because it gives a non-relaxing muon signal, and hence only contributes a temperature independent constant to $P_z(t)$. For better thermal contact vacuum grease was used. The temperature was monitored with a thermometer on the back of the backing plate.

4.5 Results and Discussion

In the following sections I present the muon depolarization data for the series of samples starting with the largest lanthanide ion, Pr, and going to the smallest lanthanide ion, Ho. However, the last sample presented is $Sr_2GdMn_2O_7$ (see Table 4.1), for reasons explained below. The corresponding raw data are shown in Figures 4.3, 4.4, 4.6, 4.8, 4.9, 4.10, 4.11 and 4.13. We do not know the interstitial site or sites of the muon in these compounds, but since the samples have the same stoichiometry and structure, we assume that the muon resides at the same sites in all of them. Hence a direct comparison of the data for the various compounds is possible. In a μSR study by Heffner *et al.* [Heff98] on single crystals of a similar material, $Sr_{1.6}La_{1.4}Mn_2O_7$ (see Chapter 4.2), a muon site was assigned. The

Symbol	Name	effective ionic radius (Å)	
		CN = 9*	CN = 12†
Pr	Praseodynium	1.179	1.286
Nd	Neodynium	1.163	1.276
Sm	Samarium	1.132	1.260
Eu	Europium	1.120	1.252
Gd	Gadolinium	1.107	1.246
Tb	Terbium	1.095	1.236
Dy	Dysprosium	1.083	1.228
Ho	Holmium	1.072	1.221

Table 4.1: CN stands for coordination number. * from [CRC95], † from [Shan76].

assignation of this site was based on dipole field calculations, and no additional hyperfine fields were necessary to model the measured spin-rotation frequency. Of the three inequivalent oxygen sites, O(1) at (0, 0, 0), O(2) at (0, 0, 0.2) and O(3) at (0, 0.5, 0.4) (all taken in unit cell units), the authors concluded that the muon site was located about 1 ± 0.1 Å from the oxygen O(2) (see also Figure 4.2). This site is in good agreement with the assigned muon site in La_2CuO_4 [Le90] (and therefore differs from that found in the nickelates, see Chapter 3.4.4 on page 54).

The depolarization data of all the samples in this series were fitted with a stretched exponential function

$$P_z(t) = A_0 \exp(-\lambda t)^{\beta}, \tag{4.3}$$

where A_0 is a temperature and sample dependent constant and λ is the muon depolarization rate. For each sample a temperature independent background was subtracted due to muons implanted in the silver backplate.

4.5.1 $Sr_2PrMn_2O_7$ and $Sr_2NdMn_2O_7$

Neutron diffraction measurements [Batt96b] on $Sr_2LnMn_2O_7$ samples revealed that it was difficult to make phase-pure compounds for the lanthanide members Pr through to Eu. The samples were found to be biphasic although both phases are of the RP type and have similar structural parameters. The magnetic Bragg diffraction data of the $Sr_2NdMn_2O_7$ sample was successfully modelled [Batt96b] with the majority phase being magnetically ordered (over the neutron timescale)

with a transition temperature of about 140 K, close to the onset of CMR and to the decrease in the initial muon asymmetry, and with the minority phase showing no long range order and considered to be either superparamagnetic or spin-glass-like. Between 140 K and 30 K the ordered phase is believed to be composed of ferromagnetically ordered Mn moments which lie within the plane of the perovskite layer but with antiferromagnetic coupling between the two adjacent layers such that there is no net magnetic moment [Batt96b]. A more complex magnetic structure forms in $Sr_2NdMn_2O_7$ below 30 K as the Nd ions order, but either the internal magnetic fields are static and too large for the transition to be observed with the muon directly, or the relaxation is too fast.

Magnetization measurements [Batt97a] on $Sr_2PrMn_2O_7$ and $Sr_2NdMn_2O_7$ have shown the existence of two coexisting phases in each of the samples, one phase showing antiferromagnetic order below 130 K, and the results for the other are suggestive of superparamagnetism or the development of ferromagnetic clusters.

Figure 4.3 shows the muon depolarization data of the $Sr_2PrMn_2O_7$ sample for various temperatures between 5 K and 225 K. In Figure 4.5 the parameters extracted from the fit to Equation 4.3 are shown. The data for the sample containing the slightly smaller Nd ion is shown in Figure 4.4 and the temperature dependence of the fitted parameters is remarkably similar to that of the Pr sample, see Figure 4.5. For both samples we see a broad loss of the initial asymmetry A_0 with decreasing temperature. The initial asymmetry loss for the Nd compound sets in at a slightly lower temperature, see Figure 4.5 a). The relaxation λ does not exhibit a divergence for either of the samples, though there is a slight peak in the data at $T \sim 140$ K for $Sr_2PrMn_2O_7$. The parameter β has a value of ~ 1 at high temperatures for both samples, and slowly decreases to $\beta \sim 0.7$ at lower temperatures.

I now describe two scenarios, each capable to some extent of accounting the behaviour of the parameters β and A_0.

- Equation 4.3 has been used [Camp94] for many concentrated spin glass systems. In such a system, on cooling to the spin glass transition temperature T_{sg} from above one finds a constant value of A_0 while λ critically diverges at T_{sg}. In this case the parameter β is temperature dependent and usually decreases from a value of unity at about $4T_{sg}$ to a value of 1/3 at T_{sg} [Camp94, Ogie85]. For other dilute systems the parameter β can take up a value of $\beta = 0.5$ [Uemu85], see also Chapter 5. We can interpret a value of β

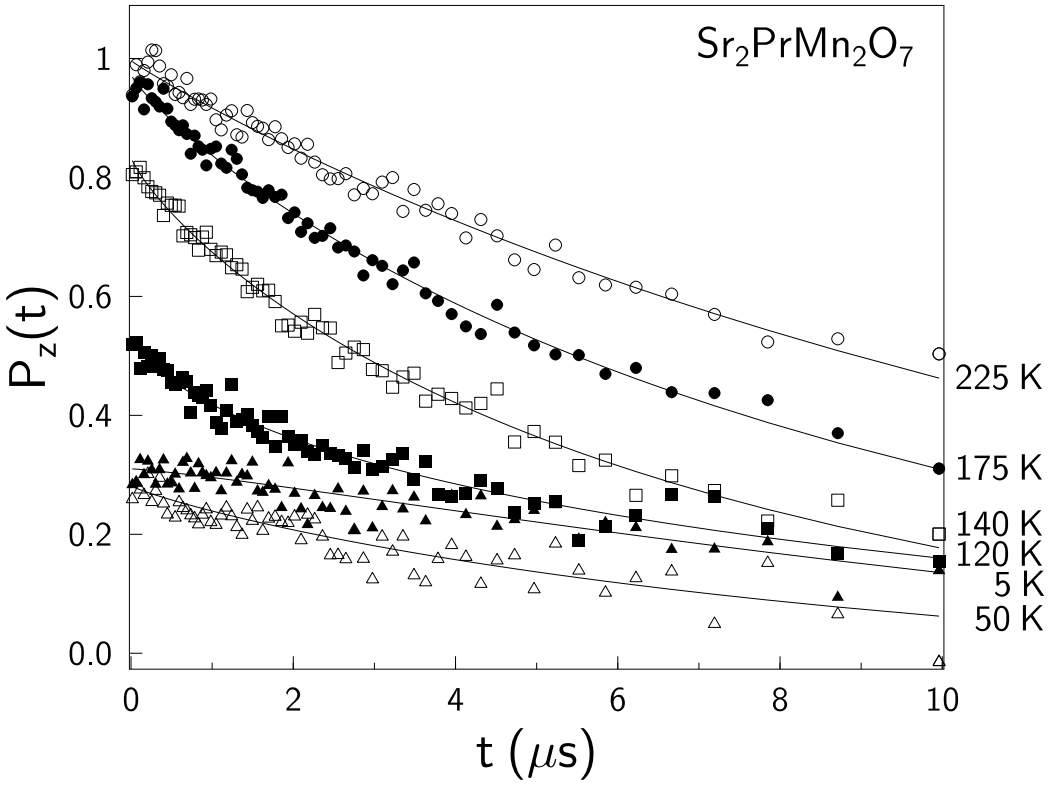

Figure 4.3: Muon depolarization of the $Sr_2PrMn_2O_7$ sample for a range of temperatures between 5 K and 225 K. The lines are fits to Equation 4.3.

less than unity as a distribution of magnetic relaxation times in the system.

- On the approach to a ferromagnetic or antiferromagnetic transition from above one would expect a constant value of A_0, and a value of $\beta = 1$ corresponds to a unique relaxation time. As T_C is approached, λ diverges critically and in the fast fluctuation limit $\lambda \propto \gamma_\mu^2 \sigma^2 / \nu$ where σ^2 is the rms magnetic field at the muon site, ν is the fluctuation rate of the spins and γ_μ is the muon gyromagnetic ratio [Uemu85], see also Chapter 3.4.2. Below T_C the internal magnetic field is often so strong that 2/3 of the inital asymmetry is lost owing to the fast depolarization from the two transverse components of the internal field relative to the initial muon polarization. This leaves a value of $A_0 = 1/3$ from the component of the internal field parallel to the initial muon polarization (assuming static internal fields in the polycrystalline samples).

However, neither of these two cases represent the muon depolarization which we see in the $Sr_2PrMn_2O_7$ and $Sr_2NdMn_2O_7$ samples, for which the initial asym-

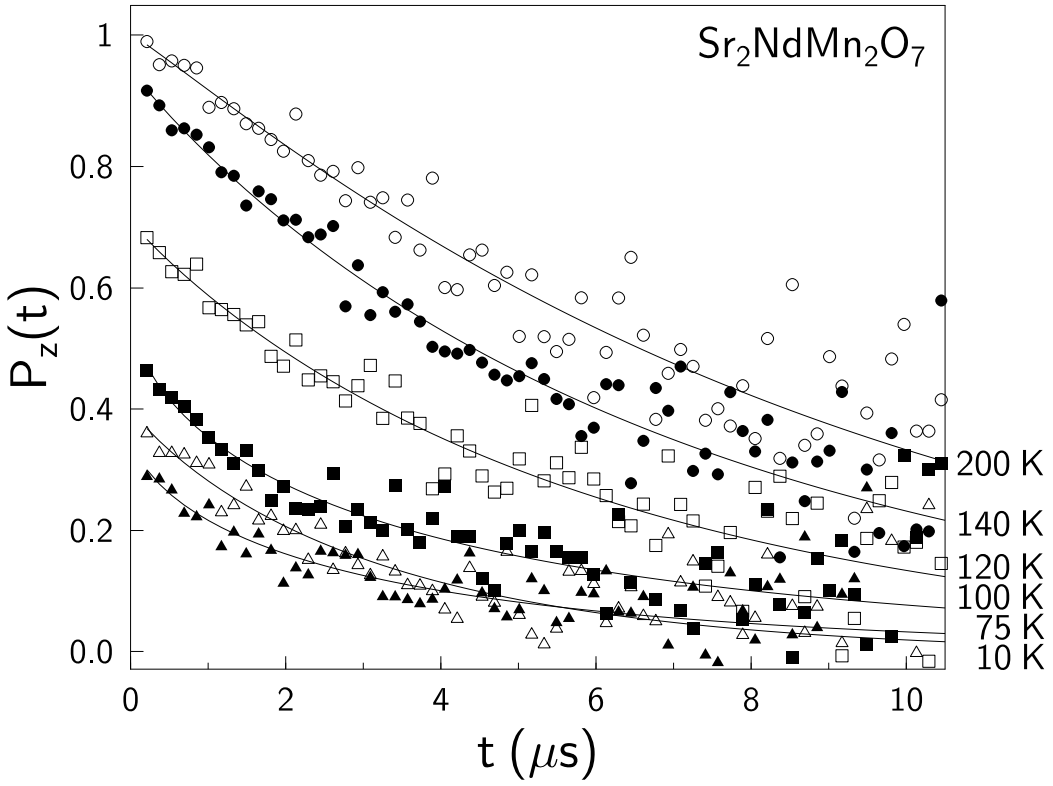

Figure 4.4: Muon depolarization of the $Sr_2NdMn_2O_7$ sample for a range of temperatures between 10 K and 200 K. The lines are fits to Equation 4.3.

metry $A_0 = P_z(0)$ slowly drops over a very wide temperature range. Figure 4.5 shows the temperature dependence of A_0, λ and β. From Figure 4.5 a) it can be seen that the initial asymmetry starts to drop around 150 K, the temperature of the onset of CMR in these sample. This also corresponds to the temperature at which magnetization measurements [Batt97a] display a split of the field cooled and zero field cooled data. The initial asymmetry decreases continuously down to 5 K, where it takes a value of about 1/3. These results strongly suggest that the magnetic state of this sample is inhomogeneous, with slowly fluctuating or even static magnetically ordered regions of the sample giving the initial rapid asymmetry loss, while other rapidly fluctuating ordered regions or non-ordered regions account for the slower depolarization component. As the temperature is reduced,

- either the ordered regions (hereafter referred to as clusters) slowly grow at the expense of the non-ordered regions, or
- rapidly fluctuating ordered regions fluctuate more slowly and hence cause the initial asymmetry to slowly decrease.

In view of magnetic neutron diffraction results discussed below, the latter is the more appropriate model to describe the data.

Such a picture of the magnetization would also qualitatively explain many of the other macroscopic measurements. For instance, if the temperature is below the blocking temperature of these clusters (that is, the temperature below which the spins appear static for the time window of the experiment) then one would expect a splitting of the field cooled and zero field cooled magnetization. This indeed is observed in these samples [Batt97a]. It may also indicate why CMR in the $n = 2$ RP phases is observed over an extended temperature range. As mentioned above, CMR is normally observed in only a small region around T_C where the application of a field can align the dynamic clusters necessary for the e_g electron to become mobile and hence reduce the resistivity. These results show that in this sample clusters are not limited to a small temperature region above T_C but are present over the whole temperature range from 4 K to 150 K. A clustered magnetic state would also provide an explanation of the non-metallic resistivity observed in the sample [Batt96a], as the lack of long range ferromagnetic order would inhibit the mobility of the e_g electrons.

The temperature dependence of λ for both samples also displays unusual behaviour (Figure 4.5 b)). In general, there are two extreme regions of the behaviour of λ which depend on how fast the fluctuation rate is. Usually (and essentially independent of the assumptions of the internal magnetic field distribution) λ is small when the fluctuation rate is very slow or very fast, but peaks when it is in the intermediate region (this is called the "critically slowing down" of spin fluctuations). Here, as the temperature is lowered towards 150 K, λ increases (Figure 4.5 b)) and hence there is a decrease in the spin fluctuation rate as expected. However, λ does not critically diverge at any temperature in either sample, and in $Sr_2PrMn_2O_7$ it exhibits only a small peak around 140 K with a relatively low value of ~ 0.16 MHz. We deduce that the muon is sensitive to magnetic fluctuations which are still very fast over the whole temperature range, and the relaxation may be dominated by the fluctuations of the lanthanide moment and/or the phase that does not undergo a magnetic phase transition. Below 140 K, λ levels off and starts to decrease again at low temperatures. At these lowest temperatures λ represents the decay of the 1/3 component of the asymmetry, see above. The decay of this 1/3 component generally means fluctuating rather than static (longitudinal) fields at the muon site. Uemura [Uemu85] has shown that the decay of this component

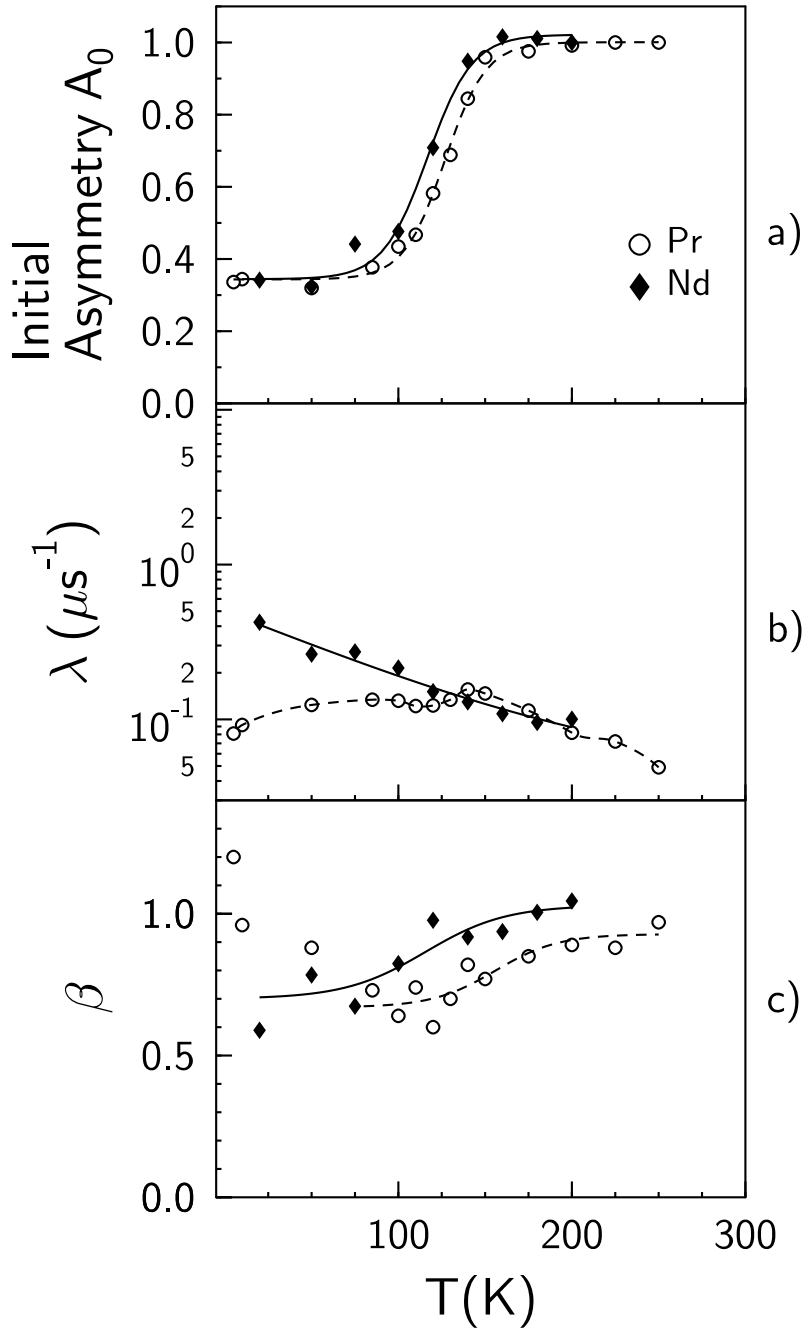

Figure 4.5: The temperature dependence of the a) initial asymmetry A_0, b) muon depolarization rate λ and c) β, for the samples containing the rare-earths Pr and Nd.

is given by $\lambda(T) \propto \nu(T)$, i.e. the slower the spin fluctuation rate ν the smaller λ. The results show that although the magnetic fluctuations are continuously slowing down with temperature they are still present even at the lowest measured temperature of 5 K. Figure 4.5 c) shows that β drops slowly from a value close to 1 at high temperatures, in $Sr_2PrMn_2O_7$ to a value of about 0.7 at low temperatures, indicative of a spread of relaxation rates.

The model of dynamic clusters as proposed from the muon data is consistent with the macroscopic measurements such as the splitting of the field cooled and zero field cooled magnetization data [Batt97a]. The neutron data gives constraints on the timescale of the fluctuations since neutrons and muons have differing resolutions and time windows. It should be remarked that it is not a new observation that sometimes muon and neutron techniques appear to be in contradiction, see for example [Nach98]. When interpreting the data, one has to consider intricacies and differences of the techniques, such as different time windows and possible limits to the resolution. Depending on the resolution of the neutron diffraction instrument, ΔQ, one would not be able to distinguish any difference in the diffraction data from magnetic clusters of size $d \sim 2\pi/\Delta Q$ and infinite range magnetic order in the sample. The muon data shows that the clusters are still fluctuating below 140 K and the fluctuation rates decrease with temperature such that more and more of these clusters appear frozen within the muon time window, resulting in a gradual reduction in the initial muon asymmetry (this assumes that the internal field is too high for the instrumentation so that it cannot be observed directly by precession). This again does not conflict with the neutron data, as the neutron has a time window approximately seven or eight orders of magnitude smaller than the muon and so is not sensitive to the *slow* dynamics of these clusters.

The interpretation of the muon spin depolarization data for these systems is not straightforward since both samples are biphasic. However, from a comparison of the μSR, neutron and magnetization data one can conclude that above 140 K neither of the samples is magnetically ordered, while below T = 140 K dynamic clusters with a range of fluctuation rates are formed. These clusters gradually reduce their fluctuation rates with decreasing temperature. Over the entire region the dynamics are sufficiently slow as to appear static on the neutron timescale, though not on the muon timescale.

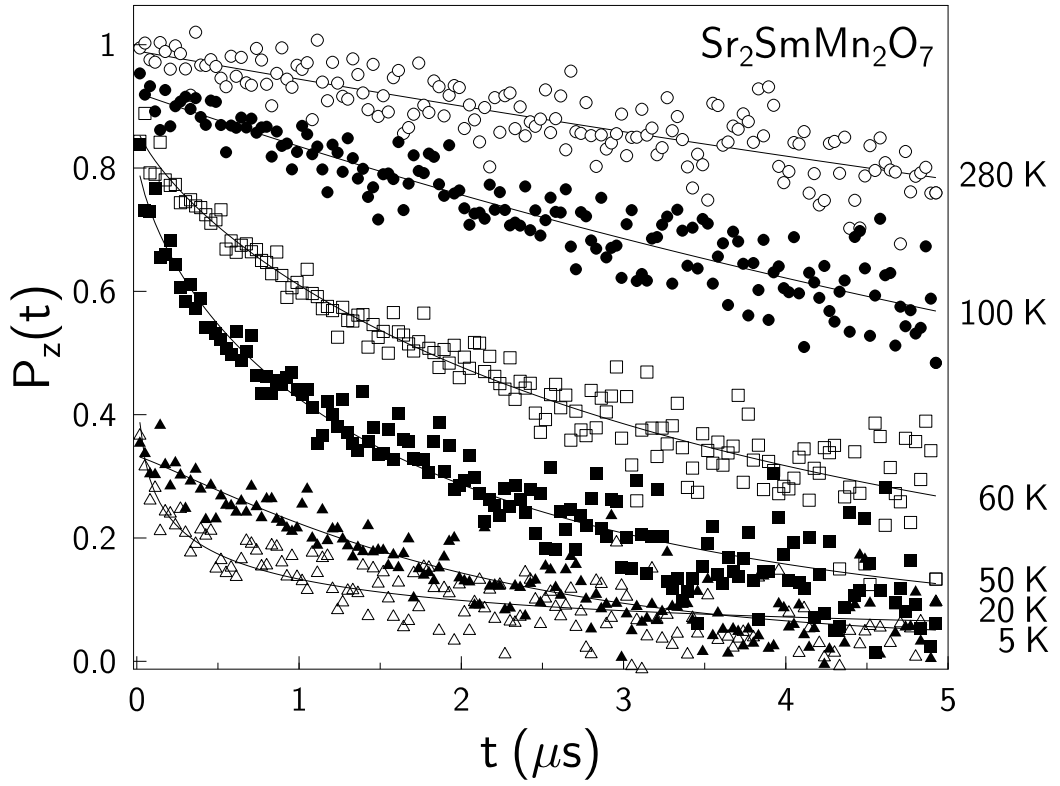

Figure 4.6: Muon depolarization of the $Sr_2SmMn_2O_7$ sample for a range of temperatures between 5 K and 280 K. The lines are fits to Equation 4.3.

4.5.2 $Sr_2SmMn_2O_7$

On reducing the size of the lanthanide ion further from Nd to Sm a significant change in the data (see Figure 4.6) and the magnetic behaviour is observed. Figure 4.7 b) shows that λ diverges beyond the experimental limits at about 30 K. This agrees with previous magnetization measurements for this sample [Batt97a] which show the presence of a cusp in the zero field cooled data at this temperature, with a splitting of the field cooled and zero field cooled data.

At higher temperatures β has a value of 1 (Figure 4.7 c)) while with decreasing temperature it decreases monotonically down to a value of 0.3 at the spin glass transition temperature T_{sg}. Such a temperature dependence of λ and β has been observed in many concentrated spin glass systems [Camp94, Ogie85] showing that there is a slowing down of the magnetic fluctuations on approaching T_{sg} with a broad distribution of relaxation rates, which might be indicative of magnetic frustration. However, unlike conventional spin glass systems there is a decrease in the initial muon asymmetry as the temperature approaches T_{sg} from above. As with

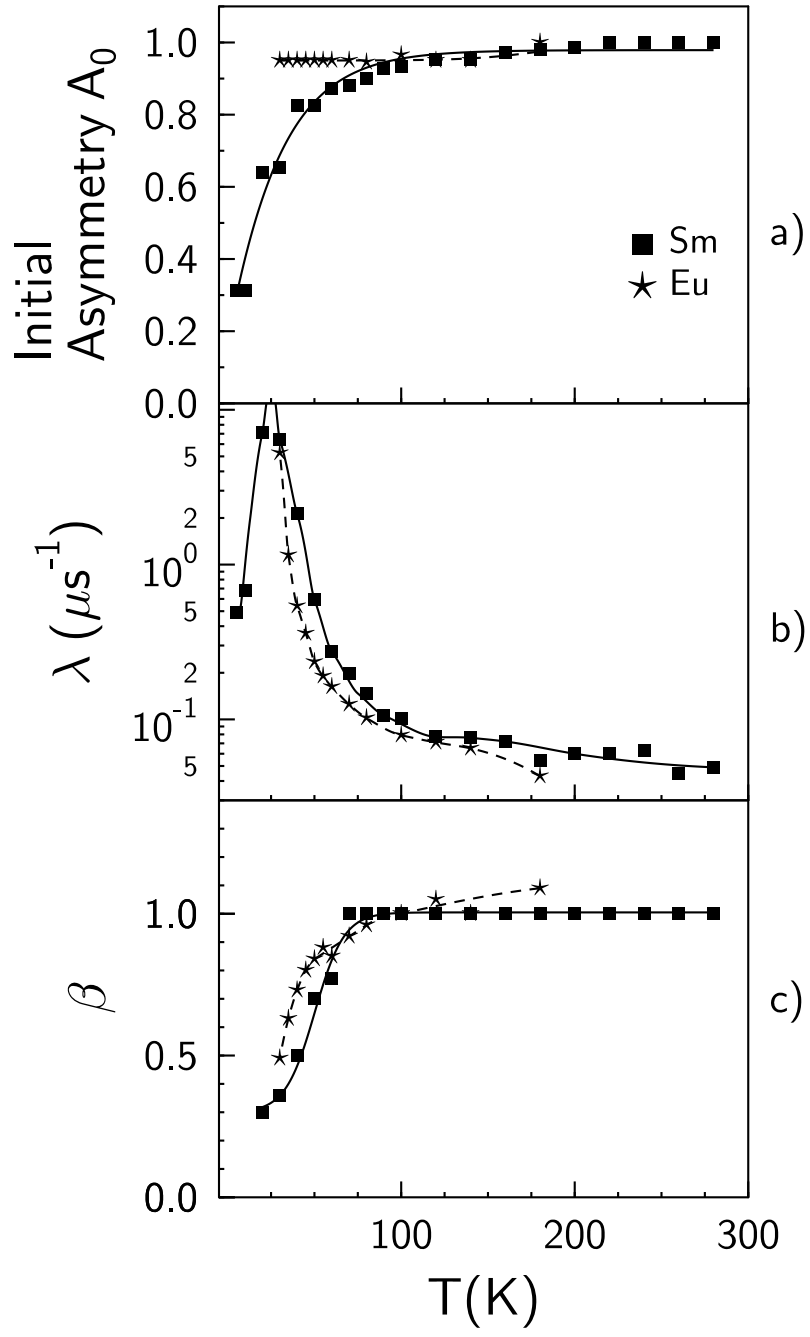

Figure 4.7: The temperature dependence of the a) initial asymmetry A_0, b) muon depolarization rate λ and c) β, for the samples containing the rare-earths Sm and Eu.

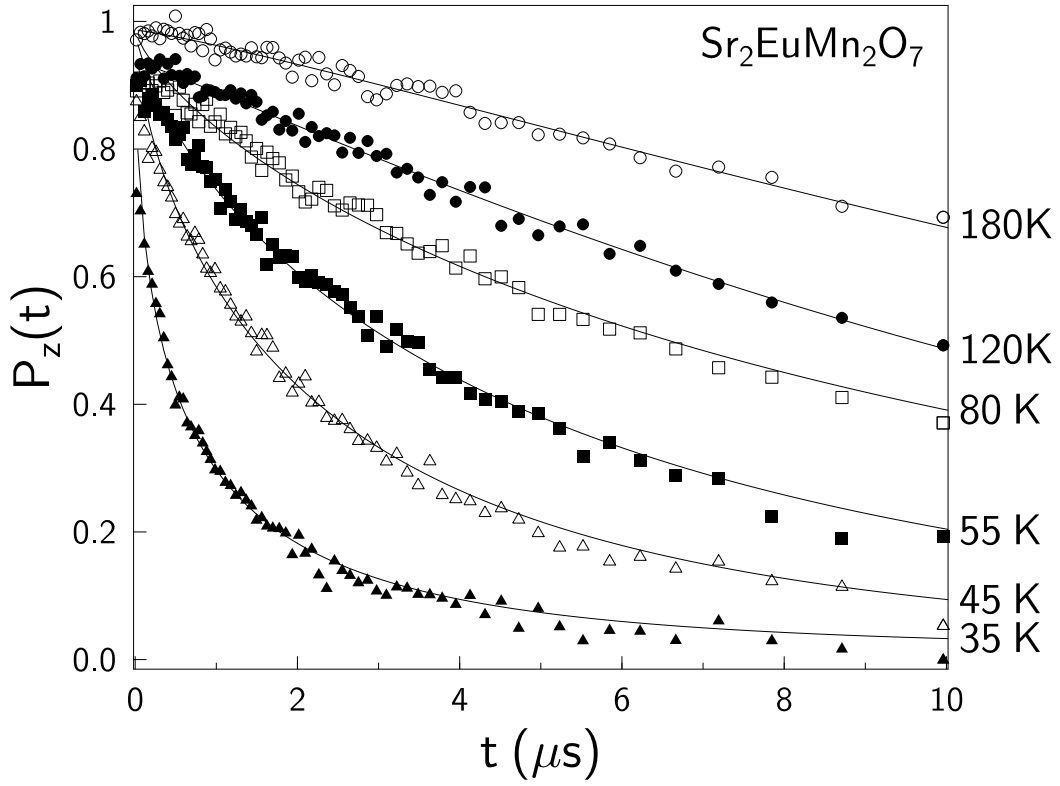

Figure 4.8: Muon depolarization of the $Sr_2EuMn_2O_7$ sample for a range of temperatures between 35 K and 180 K. The lines are fits to Equation 4.3.

the Nd and Pr samples we believe that this initial asymmetry loss is due to some muons residing in magnetic clusters, in agreement with magnetization measurements [Batt97a]. The lower temperature of the asymmetry loss in the Sm sample as compared to the Nd and Pr samples shows a weakening of the ferromagnetic exchange within these clusters. We can therefore postulate a magnetic state which is frustrated but in which the ferromagnetic exchange is still just strong enough for some clusters to form at lower temperatures.

4.5.3 $Sr_2EuMn_2O_7$

The ferromagnetic exchange is weakened further on reducing the size of the lanthanide ion from Sm to Eu. The muon depolarization data (Figure 4.8) of this sample shows no loss of initial asymmetry over the temperature range measured, indicating that ferromagnetic clusters are not being formed. The temperature dependence of λ (Figure 4.7 b)) and β (Figure 4.7 c)) is as expected for a spin glass system. This, coupled with the spin glass like cusp observed in the magnetization

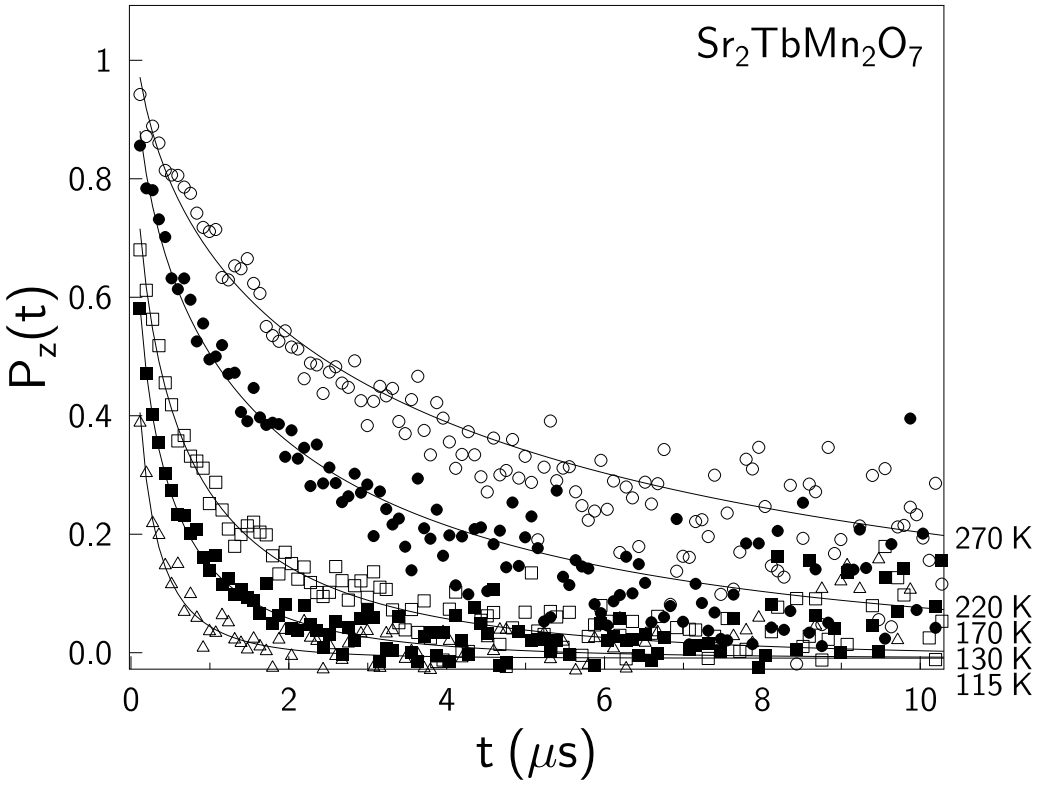

Figure 4.9: Muon depolarization of the $Sr_2TbMn_2O_7$ sample for a range of temperatures between 115 K and 270 K. The lines are fits to Equation 4.3 with $\beta = 0.5$.

data [Batt97a] leads one to conclude that the sample containing Eu is a spin glass. The distortion of the MnO_6 octahedra has clearly reached a critical point where the ferromagnetic double exchange has been so weakened that it becomes comparable in size to the antiferromagnetic superexchange. The resulting competing interactions yield a frustrated magnetic lattice with no magnetic long-range order.

4.5.4 $Sr_2TbMn_2O_7$, $Sr_2DyMn_2O_7$ and $Sr_2HoMn_2O_7$

The trend of weakening ferromagnetic exchange with reduction in the lanthanide ion size continues (see Figures 4.9, 4.10 and 4.11). Ultimately the Mn ions behave almost as isolated ions, resulting in paramagnetic behaviour. This has been shown by previous magnetization measurements [Batt97a] on the samples containing Tb, Dy and Ho. For these compounds the temperature dependence of the magnetization is well described by the Curie-Weiss law, yielding magnetic moments close to those expected for localized free ions of lanthanide, Mn^{3+} and Mn^{4+}. A very

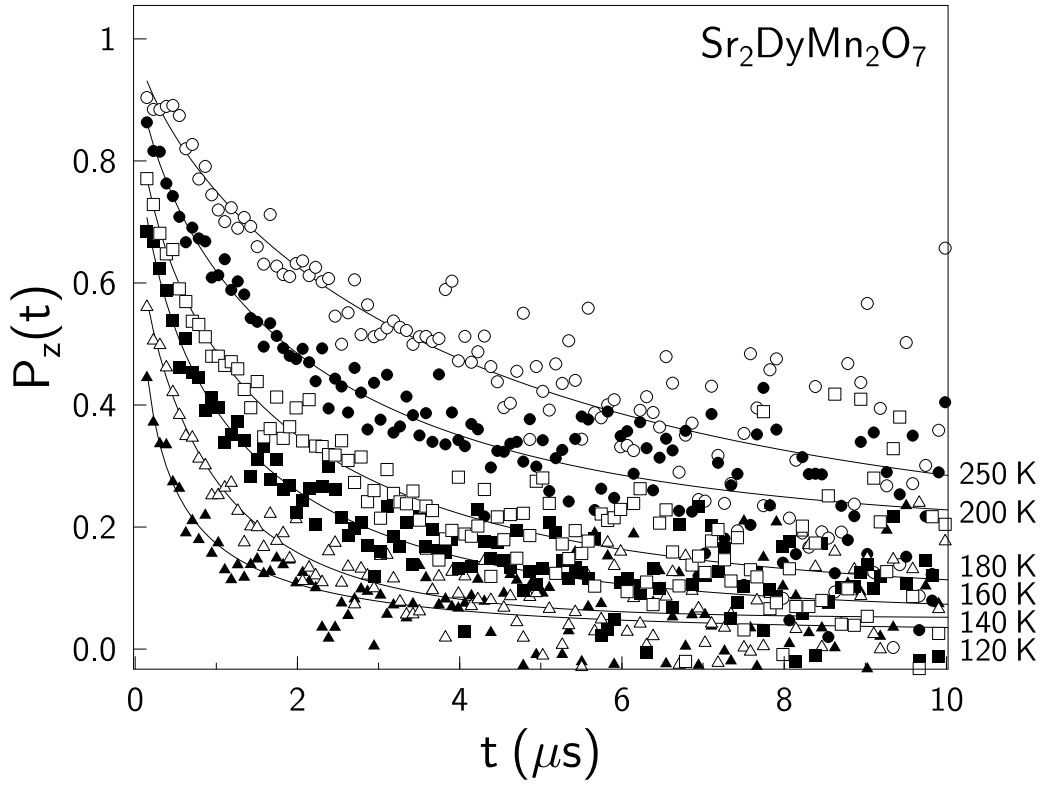

Figure 4.10: Muon depolarization of the $Sr_2DyMn_2O_7$ sample for a range of temperatures between 120 K and 250 K. The lines are fits to Equation 4.3 with $\beta = 0.5$.

slight splitting of the field cooled and zero field cooled data is observed at low temperatures indicating that weak frustrated exchange interactions still exist.

The μSR depolarization data for both the Tb and Dy samples were fitted by Equation 4.3 at all temperatures with a constant value of the initial asymmetry and a constant value of $\beta = 0.5$. λ is very large in these samples and monotonically increases with decreasing temperature until it has increased beyond the experimental range at about 120 K even though the samples are in a paramagnetic phase. It must be remembered that the muon depolarization in all the samples results from interaction not just with the Mn ions but also with the rare-earth ions. The non S-state rare-earth ions can strongly couple to the lattice through the interaction of their orbital moments with the internal crystal fields. In the case of the samples containing the Dy and Tb ions we believe that this pinning anisotropy is very strong thus causing a much slower fluctuation rate of these ions compared to the Mn ions and therefore a large value of λ (in the fast fluctuation limit λ is directly proportional to the inverse of the fluctuation rate, see Section

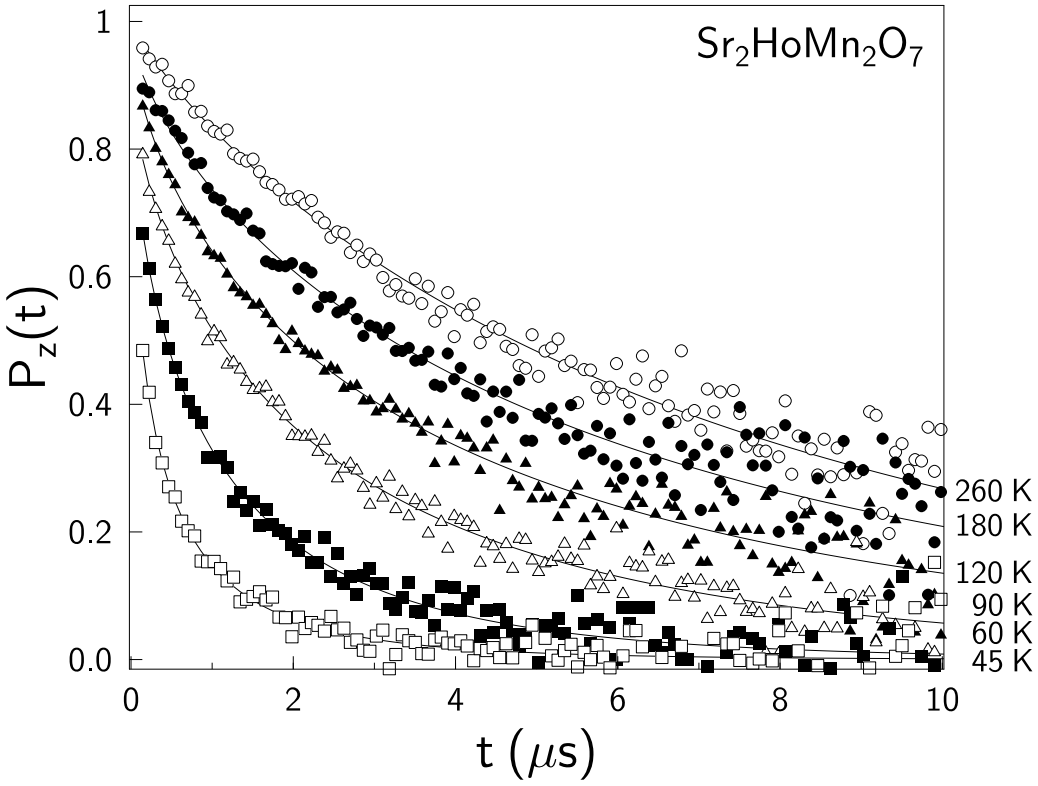

Figure 4.11: Muon depolarization of the $Sr_2HoMn_2O_7$ sample for a range of temperatures between 45 K and 260 K. The lines are fits to Equation 4.3 with $\beta = 0.5$.

4.5.1).

Support for this argument comes from other aspects of the data:

- First, the slowly fluctuating Tb, Dy and Ho ions would dominate the muon depolarization. As these ions substitute approximately randomly for the Sr ions in the lattice the muons would experience a large range of internal fields which can give rise to a "root exponential" [Uemu85] decay of the muon asymmetry, as is observed in both these samples.

- Second, if the dominant effect on the spin fluctuation rate were the anisotropy then one would expect the temperature dependence of the fluctuation rate or λ to have an Arrhenius like behaviour, i.e. activation of the spins over the anisotropy barrier.

Such behaviour is observed as can be seen in Figure 4.12, where a linear dependence of the $T\ln(\lambda[\mathrm{MHz}])$ versus T shows activated behaviour of the spin fluctuation rate. The intercept on the $T\ln\lambda$ axis in Figure 4.12 gives the effective

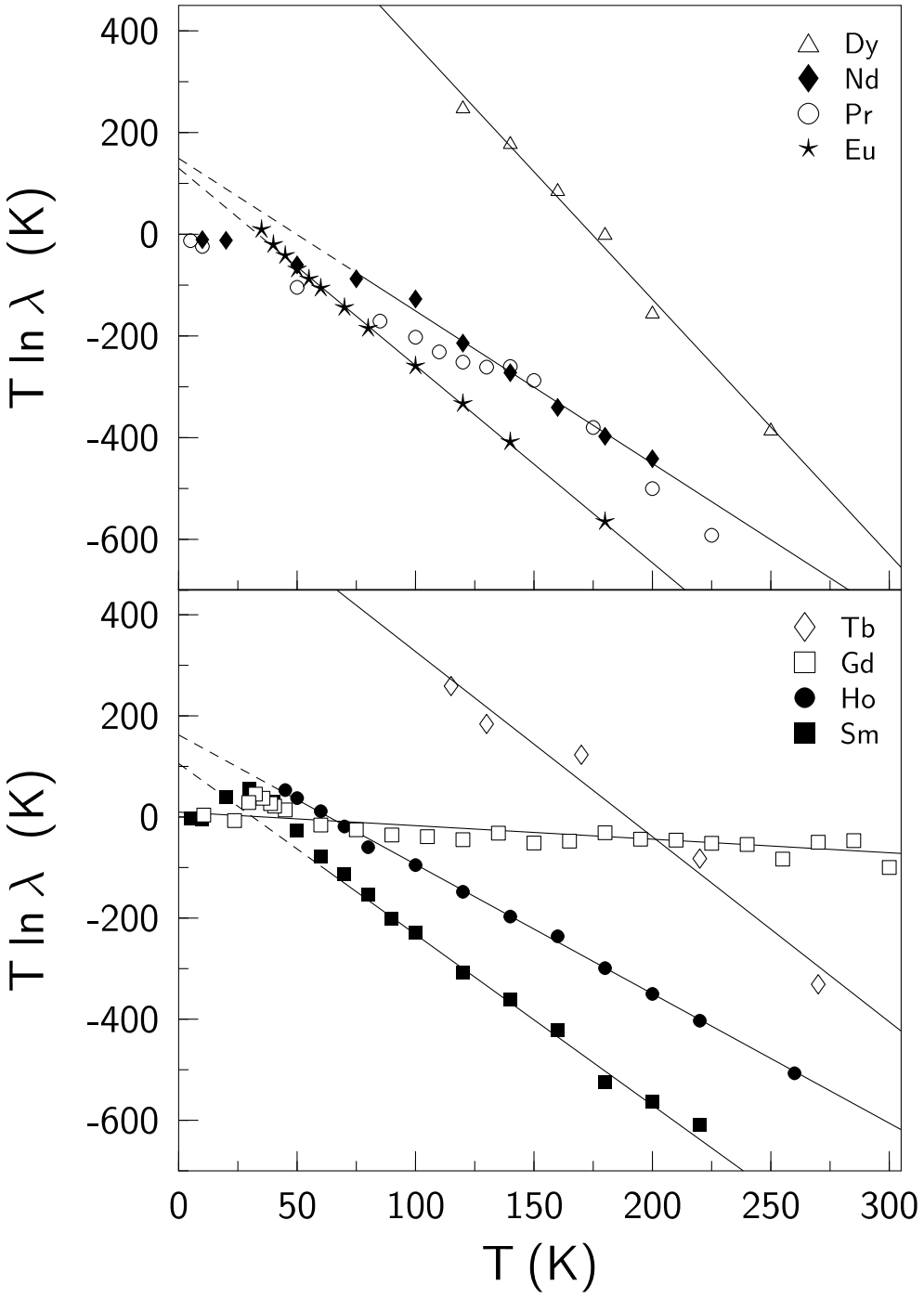

Figure 4.12: A graph of $T\ln\lambda$ versus temperature for samples containing the rare-earths Pr, Nd, Sm, Eu, Tb, Dy, Ho and Gd. A linear relationship shows Arrhenius like behaviour of the spin fluctuation rate with temperature. The intercept on the $T\ln\lambda$ axis gives the effective activation energy in Kelvin, and the gradient is proportional to the product of the second moment of the internal field and the spin relaxation time $1/\nu$ (see text).

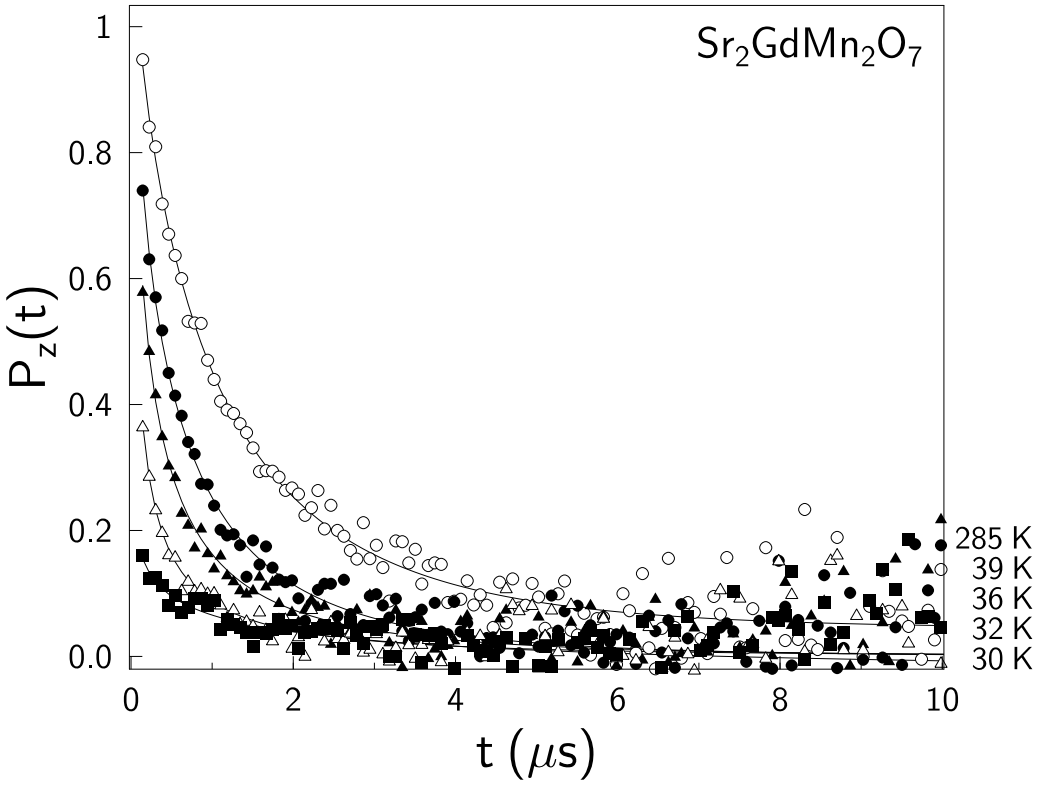

Figure 4.13: Muon depolarization of the $Sr_2GdMn_2O_7$ sample for a range of temperatures between 11 K and 285 K. The lines are fits to Equation 4.3.

activation energy E_a in Kelvin and the gradient is related to the intrinsic fluctuation rate. The activation energies of the Dy and Tb samples are very large, 880±40 K and 690±70 K respectively, leading to large relaxation rates. As shown in Figure 4.12, some of the other samples containing other rare-earth ions also display linear behaviour at higher temperatures although the intercept shows that the activation energies are much smaller.

4.5.5 $Sr_2GdMn_2O_7$

The sample containing Gd (Figure 4.13) is a special case because Gd is an S-state ($^8S_{7/2}$) ion and therefore little or no crystal anisotropy is expected. The data were fitted by Equation 4.3 at all temperatures with a constant value of the initial asymmetry and a fixed value of $\beta = 0.5$. Corresponding to the reduced crystal anisotropy the activation energy for this sample obtained from Figure 4.12 is very close to zero, adding further support to the above interpretation. The deviation from linearity at lower temperatures occurs because it is not possible to ignore

the effect of the Mn spins on the muon depolarization as the Mn spins rapidly slow down on the approach to the spin glass like transition. Similar behaviour is observed for the Eu sample with a deviation from linearity approaching the spin glass transition. In the lighter rare-earths from Pr to Sm the deviations from linearity are even larger (see Figure 4.12) which is to be expected as exchange interactions between the Mn ions are even stronger.

4.6 Conclusion

In conclusion, the μSR measurements have shown the effect of the systematic decrease in the ferromagnetic coupling between the Mn ions with reduction in lanthanide ion size. None of the samples in this study displayed the long range ferromagnetic order, which is usually associated with CMR. This was not only evident from the lack of any coherent muon precession even at the lowest measured temperatures but also from the temperature dependence of the muon depolarization which is very different from that expected for a paramagnetic to ferromagnetic or antiferromagnetic transition. The μSR results show the presence of dynamic clusters in the Nd and Pr samples from $\sim$150 K down to low temperatures, corresponding to the temperature region of the observed CMR in these samples. This suggests that the CMR in these compounds may be directly linked to these dynamic clusters just as it is linked to the dynamic clusters above the ferromagnetic transition in the n=∞ CMR materials. Further evidence in support of this comes from the fact that the muon data shows that no clusters are present in the other samples of the series in which no CMR has been observed. One can speculate that the lack of ferromagnetic ordering and continuing fluctuations of the clusters and hence the extended CMR in the Pr and Nd samples may be related to the reduced dimensionality as compared to the $n = \infty$ Ruddlesden-Popper phases.

Chapter 5

Spin Dynamics in the Spin-Gap Material CaV_4O_9

Contents

5.1 Introduction

Spin-gap systems are in many respects model quantum magnetic systems [Dago95]. Often they form a dimer ground state and they are characterized by a finite energy gap in the magnetic excitation spectrum, $k_B T_{sg}$ (where k_B is the Boltzmann factor and T_{sg} the 'spin-gap temperature'). The singlet ground state is non-magnetic, whereas the triplet excited state is not. Therefore one would expect that it should be possible to access certain characteristics of spin-gap systems by μSR since the muon spin will be relaxed by spin excitations thermally excited across the gap. Subtle magnetic effects of spin-gap formation (including the spin-Peierls transition) have been reported on a wide range of materials using μSR [Garc95, Blun97, Koji97].

Below I describe a muon-spin relaxation study of the two-dimensional spin-gap system CaV_4O_9. Parts of the results in this chapter have already been reported in [Jest98]. The chapter is arranged as follows: section 5.2 describes properties of spin-gap systems and mechanisms of spin-gap formation. In particular a short overview of neutron, susceptibility and NMR experiments on CaV_4O_9 is given. In section 5.3 I describe the sample preparation and the experimental details. Section 5.4 contains the results of μSR and susceptibility measurements. It is shown that the muon response in CaV_4O_9 shows an intriguingly wide range of behaviour as a function of temperature, and a model for this behaviour is given. The last section (5.5) contains concluding remarks.

5.2 Spin-Gap Materials and Properties of CaV_4O_9

A number of one-dimensional spin-gap materials are known and have been investigated experimentally (e.g. [Bray75, Azum94, Barn94, Eccl94, Ishi94]). μSR has been used to investigate a few of these low-dimensional systems and especially spin-Peierls systems (see section 5.1).

A spin-Peierls compound can be described [Bray83] by one-dimensional antiferromagnetic spin-$\frac{1}{2}$ Heisenberg chains (without interchain spin interactions) with coupling to the (three-dimensional) phonons. The magnetic energy is taken as linear in lattice displacement and the elastic energy due to distortion of the spin-equilibrium sites is quadratic in the displacement. As a result of this competition, the magnetic energy is lowered at the expense of the elastic lattice distortions

below T_{sP}. The uniform next neighbour (NN) exchange is then replaced by two unequal alternating exchange constants. The driving force of this dimerization is the magnetoelastic coupling between the three-dimensional phonons and the one-dimensional Heisenberg spin-chains. The dimerization lifts the degeneracy of the ground state and the triplet excited states. A gap develops, the excited states are no longer populated at $T = 0$ K and the magnetic energy is lowered. A signature of the gap is a fall of the magnetic susceptibility below T_{sP}.

In the case of an opening of a spin-gap one would also expect a dramatic effect on the spin dynamics. For example in NMR measurements on such spin-Peierls systems [Itoh95, Smit76] a sharp decrease in the relaxation rate is found below T_{sP} since the main relaxation mechanism is reduced as it becomes increasingly difficult to thermally excite across the gap as the sample is cooled. One can estimate the magnitude of the spin-gap by analysing the relaxation rates. In the case of a temperature independent gap one would, in the simplest case, expect a temperature activated functional form.

The existence of the first (quasi-)two-dimensional spin-gap material, CaV_4O_9, has only been reported recently [Tani95]. The mechanism for the existence of a spin-gap is obviously not the same as for spin-Peierls systems, yet similar experimental observations can be made. The material consists of V_4O_9 planes (see Figure 5.1) separated by layers of calcium atoms [Boul73]. Each vanadium atom is at the centre of an O_5 square pyramid. The vanadium atoms are in oxidation state IV and thus behave as a localized spin with $S = \frac{1}{2}$. Magnetic susceptibility [Tani95], NMR [Oham97, Koda97] and neutron scattering [Koda97, Koda96] measurements indicate the existence of a spin-gap in this material with a spin-gap temperature $T_{sg} \sim 110$ K. These experimental reports have stimulated a number of theoretical studies [Kato95, Albr96a, Albr96b, Gelf96, Mesh96, Miya96, Sach96, Sano96, Star96, Troy96, Ueda96, Whit96, Bose97, Fuko97, Ivan97, Pick97, Weih97, Weih98]. One way to approach this magnetic system is to describe it by a Heisenberg model for the vanadium spins for a $\frac{1}{5}$ depleted square lattice. At each site of this lattice two of the bonds belong to spin plaquettes ("plaquette bonds"), and the third one connects a plaquette with its neighbour ("dimer bond"). The inclusion of a frustrating next nearest neighbour (NNN) interaction seems to be essential for the formation of the spin-gap [Ueda96]. Starykh *et al.* [Star96] argue that CaV_4O_9 might represent an example of a two-dimensional "spin-Peierls"-like system where spin-phonon coupling cooperates with tendencies to form a spin-gap

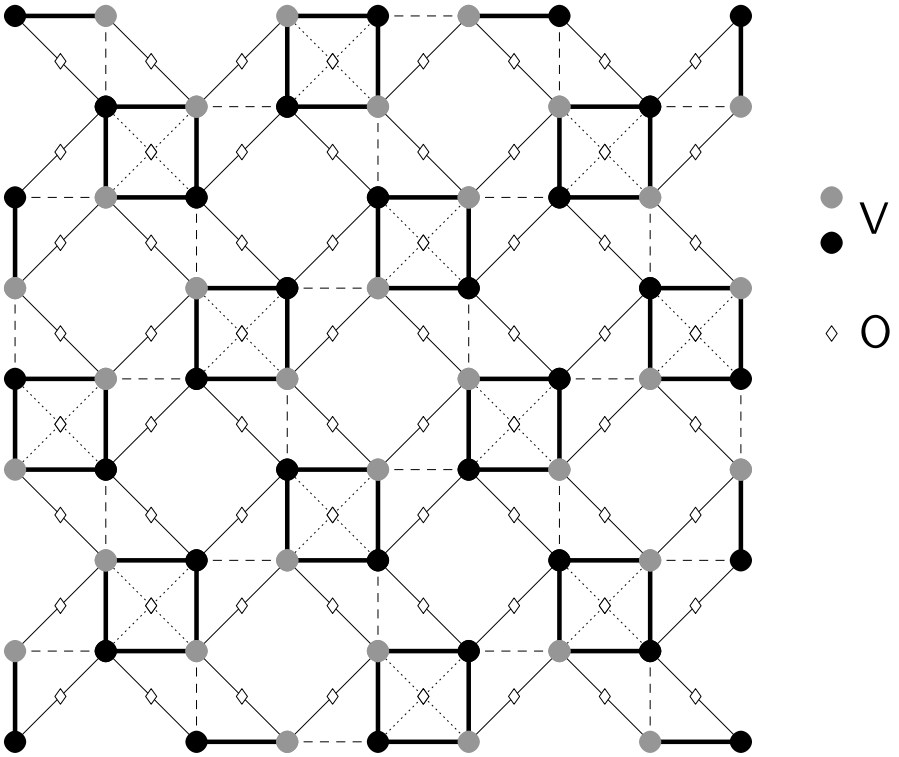

Figure 5.1: Structure of V-O plane in CaV_4O_9. The diamonds represent the oxygen atoms, the black and grey circles are the vanadium atoms slightly below and above the CaV_4O_9 plane. Figure after [Fuko98].

due to the frustrating NNN interactions.

These theoretical studies usually idealize the V-O layer as flat, whereas in reality it consists of V atoms slightly above and below the plane, see Figure 5.1. These structural intricacies motivated a later study [Pick97], which suggests that the NNN coupling of the V atoms to those above (below) the plane are stronger than those to the actual next neighbour, which sits below (above) the plane. The author of this study therefore suggested that a picture of two coupled metaplaquette systems is a realistic way of interpreting the spin-gap behaviour. The metaplaquettes are in the two planar layers slightly above and below the the V-O plane, see also [Weih98].

The investigation of the properties of CaV_4O_9 with μSR is motivated by interest in the spin-gap and possible influences on the magnetic excitation spectrum.

5.3 Sample Preparation and Experimental Details

Powder samples of CaV_4O_9 were prepared by R. C. C. Ward (Clarendon Laboratory) by reaction of molar ratios of CaO (Johnson Matthey, puratronic grade) and VO_2 (99.9%, Aldrich Chemical Co.). The starting powders were ground together in a glovebox and then sealed under vacuum in silica ampoules. Heat treatments of 18 hr at 750 °C were employed, following previous reports [Tani95, Boul73]. The product was reground in the glovebox and the heat treatment repeated to ensure homogeneous reaction. After this stage the product appeared uniformly green in colour. We shall see below that our material contains a substantial concentration of magnetic defects, presumably arising from disorder in the vanadium sublattice.

μSR experiments below room temperature were carried out at the General Purpose Spectrometer (GPS) of the Paul-Scherrer-Institute (Switzerland). The sample was mounted on a silver backing plate (which provides a non-relaxing muon-spin signal) and inserted in a helium flow cryostat. Additional ZF experiments above room-temperature were performed at the RIKEN beamline and further experiments to determine the field dependence of the relaxation at the MuSR beamline, both at the Rutherford Appleton Laboratory (U.K.). There the sample was mounted on a silver backing plate in a Closed Cycle Refrigerator (CCR) device. In each of the experiments the earth's magnetic field was compensated to better than 10 μT.

In order to characterize the magnetic properties I have also performed magnetization measurements at the Quantum Design SQUID magnetometer in the Inorganic Chemistry Laboratory, Oxford.

5.4 Experimental Results

5.4.1 Susceptibility and Defect Spins

The mass magnetization M was measured in an applied magnetic field of $B = 0.1$ T. Variation of the magnetic field up to at least 1 T shows a linear relation between mass magnetization M and applied field B. Figure 5.2 (open circles) shows

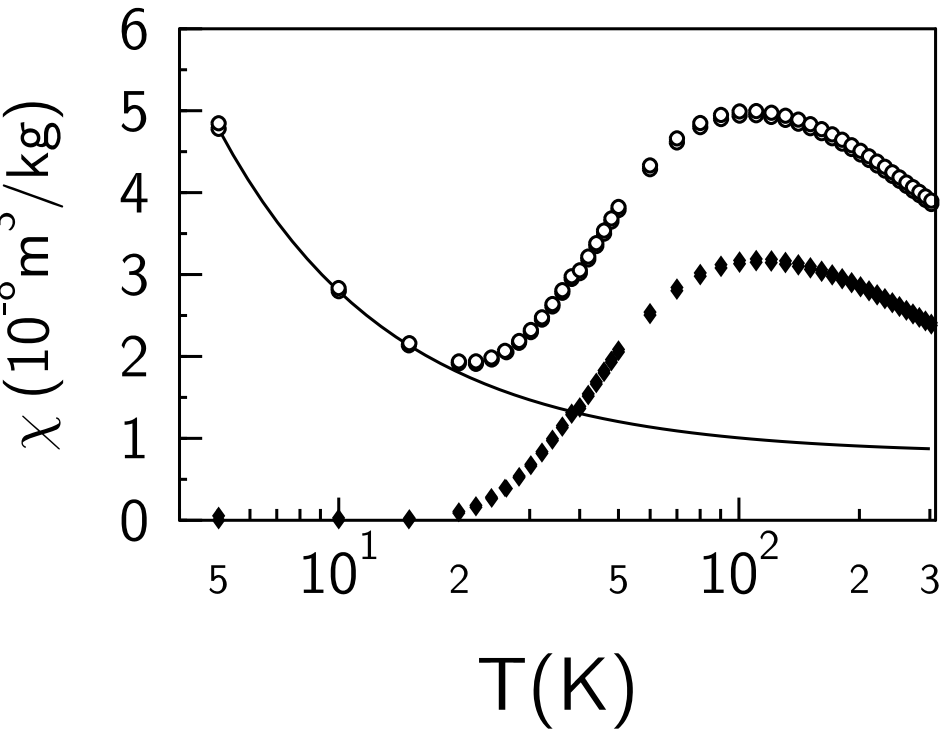

Figure 5.2: Susceptibility data for CaV_4O_9. The open circles show the total mass susceptibility, χ_{tot}, the diamonds show the spin susceptibility, χ_{spin}, and the full line shows the spin-defect contribution, χ_{def}, see text.

the mass susceptibility

$$\chi_{tot} = \mu_0 M/B \tag{5.1}$$

of the sample of CaV_4O_9. Below ~ 20 K there is an upturn of χ_{tot} with decreasing temperature. This can be ascribed to defect spins (see below). Below the spin-gap temperature of $T_{sg} \sim 110$ K the value of χ_{tot} drops with decreasing temperature.

Following [Tani95] we can split the contributions to the susceptibility into three terms:

(i) the spin susceptibility χ_{spin},

(ii) χ_0, that is the diamagnetic part and the Van Vleck paramagnetic part (both temperature independent) and

(iii) the defect spin contribution

$$\chi_{def} = \frac{C}{T}, \quad \text{with } C = \frac{N}{m} \times (g\mu_B)^2 \, \frac{J(J+1)}{3k_B}, \tag{5.2}$$

where N is the number of defect spins in the sample, m the mass of the sample, μ_B the Bohr magneton and k_B the Boltzmann constant. In the following treatment I take $g = 2$ and $J = 1/2$.

The expression in Equation 5.2 is a good approximation to a Brillouin function (which is the appropriate functional form for analysing isolated non-interacting spins) in the given temperature and magnetic field range, i.e. $\mu_B B/k_B T \ll 1$.

The values of C and χ_0 have been fitted assuming $\chi_{spin} = 0$ for temperatures below 15 K [Oham97] (see Figure 5.2). This enables us to plot the contribution to the susceptibility by the spin system (diamonds in Figure 5.2), in good agreement with previous measurements [Tani95]. From the fit we get

$$C = 1.99 \times 10^{-7} \, \frac{\mathrm{m^3K}}{\mathrm{kg}} \quad \text{and} \quad \chi_0 = 0.81 \times 10^{-8} \, \frac{\mathrm{m^3}}{\mathrm{kg}} \, . \tag{5.3}$$

With the help of Equation 5.2 we can estimate the defect-spin density to be $N/m \approx 5.1 \times 10^{22}/\mathrm{kg}$, giving $\approx 3.3 \times 10^{-2}$ defect spins per formula unit. As demonstrated below these defect-spins lead to observable muon-spin relaxation at low temperatures.

5.4.2 Results of μSR measurements

Typical $G_z(t)$ values are shown in Figure 5.3 for $T = 30$ K $< T_{sg}$ and $T = 160$ K $> T_{sg}$. Well below T_{sg}, G_z is well fitted by an exponential function, and well above by a Gaussian. No oscillations were observed at any temperature, nor was any reduction of the initial asymmetry measurable. We can follow the exact behaviour of the relaxation curve as a function of temperature by fitting the data to the stretched exponential form (see Equation 2.25)

$$G_z(t) = A_{\mathrm{S}} e^{-(\lambda t)^\beta} + A_{\mathrm{Ag}}, \tag{5.4}$$

where λ is a temperature-dependent relaxation rate; A_S and A_{Ag} are temperature independent amplitudes, reflecting the relative fraction of muons stopping in the sample ($\sim A_S$) and in the silver backing plate ($\sim A_{Ag}$). A value of $\beta = 2$

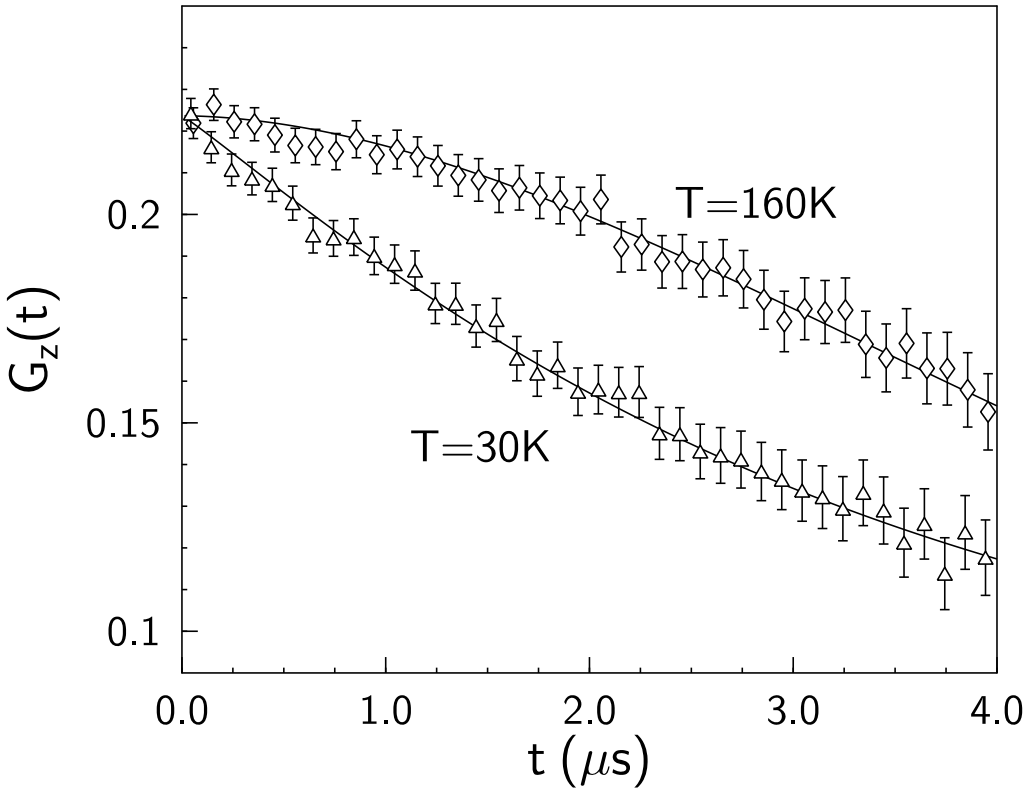

Figure 5.3: Typical forms of the μSR relaxation function for CaV_4O_9. The solid lines are fits to Equation 5.4.

corresponds to a Gaussian relaxation, $\beta = 1$ corresponds to an exponential relaxation and $\beta = \frac{1}{2}$ corresponds to a root-exponential relaxation (see Chapter 2). Equation 5.4 fits the data well over the entire temperature range studied. In the fitting process A_S and A_{Ag} were determined at high temperatures and kept fixed for all temperatures, and λ and β were adjustable parameters whose variations give information on spin dynamics.

From Figure 5.4 we can see that $\beta \approx 0.5$ for temperatures below 25 K. Above this temperature it rises to unity. For higher temperatures it rises to a peak value of almost 2 at 160 K, and drops off to a value of about 1 at the highest temperatures of the experiment (450 K).

The value of λ drops from about 0.45 μs^{-1} at the lowest temperature to about 0.05 μs^{-1} at the highest temperature, with a small rise around 160 K, the region where the lineshape becomes Gaussian.

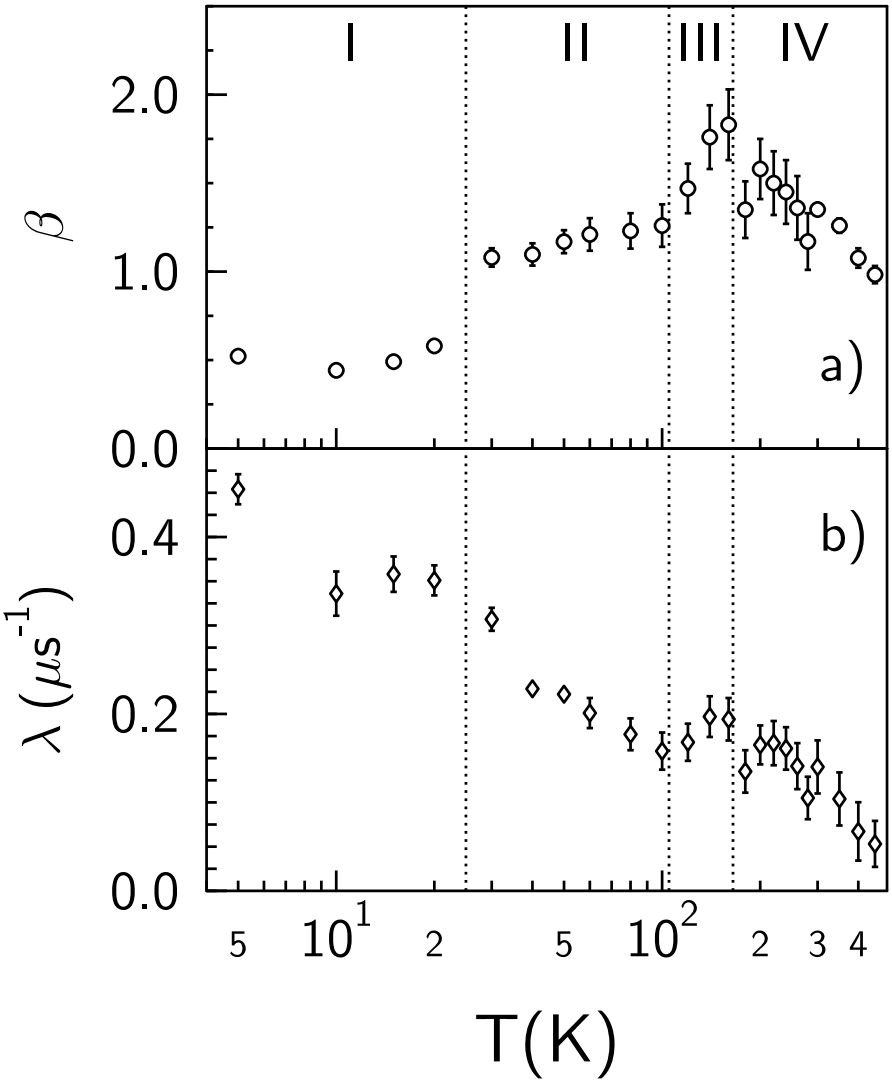

Figure 5.4: Parameters extracted from the fits to Equation 5.4.

5.4.3 Modelling the μSR temperature dependence

There is a large variation of the parameter β as a function of temperature which needs to be explained. For the purpose of modelling the complex temperature dependence of β, I have divided the temperature range into four different regions (see also Figure 5.4):

- Region I: $T < 30$ K
- Region II: 30 K $< T < T_{sg} \approx 100$ K
- Region III: $T_{sg} < T \lesssim 160$ K
- Region IV: 160 K $\lesssim T$

In the following the four regions are examined, starting with region III and IV, and then region II and I are treated.

Isotope	Natural Abundance (%)	Spin	Nuclear Magnetic Moment
^{40}Ca	96.941(18)	0	
^{42}Ca	0.647(9)	0	
^{43}Ca	0.135(6)	7/2	-1.3173 μ_N
^{46}Ca	0.004(3)	0	
^{48}Ca	0.187(4)	0	
^{16}O	99.762(15)	0	
^{17}O	0.038(3)	5/2	-1.8938 μ_N
^{18}O	0.200(12)	0	
^{50}V	0.250(2)	6	+3.34569 μ_N
^{51}V	99.750(2)	7/2	+5.148706 μ_N

Table 5.1: Isotopes in CaV_4O_9 and their properties, taken from [CRC95].

Region III: Above T_{sg}

Above T_{sg} the parameter β rises from ~ 1 to a maximum value of $\beta \sim 1.9$ at 160 K. This behaviour can be ascribed to the fluctuations of the electronic spins [Haya79]. At low temperatures the electronic fluctuations produce exponential relaxation but, as the temperature rises, these fluctuations become too fast for the

muon to follow. Hence the dipole fields of the fast fluctuating electronic spins average to zero over a time much shorter than the lifetime of the muon. A Gaussian relaxation, as seen here, is characteristic of randomly orientated quasi-static magnetic moments. This resulting Gaussian relaxation therefore can be attributed to quasi-static nuclear moments [Haya79] of ^{51}V, see Table 5.1. From [Koda97] we can extrapolate that the nuclear spin relaxation time in this temperature region is longer than the typical muon lifetime, consistent with our model.

In order to test this hypothesis we have performed additional longitudinal field measurements. In the picture described above, we would expect a static Kubo-Toyabe function (see Equation 2.21) or a dynamic Kubo-Toyabe function (see Equation 2.22) with a small fluctuation rate to be the appropriate functional form for the analysis of the data. If nuclear spins are responsible for the shape of our polarization spectra we would expect a rapid repolarization, with magnetic field values of a few tens of Gauss giving the full recovery of the asymmetry, and we would expect the parameter Δ to be compatible with the curves in Figures 2.11 or 2.13.

Figure 5.5 shows the measured LF spectra at 180 K and the corresponding best fits to a dynamic Kubo-Toyabe function. The only varying parameter in the Figure is the applied field, while the fluctuation rate $\nu = 0.20$ MHz and the width of the magnetic field distribution $\Delta = 0.21$ G were both kept fixed. The curves fit the measured spectra well, and thus are in agreement with our model.

Region IV: Nuclear spin dynamics or muon hopping above T = 160 K

Above 160 K the functional form of the relaxation becomes an exponential again. This drop in β is explained by the onset of either speeding up nuclear magnetic fluctuations or muon hopping. Thus, the muon averages the fields of the randomly orientated nuclear spins [Haya79]. We can follow this behaviour more closely by using the dynamic Kubo-Toyabe functional form, Equation 2.22. We have fixed all parameters as above, except the fluctuation rate, which has been fitted as a function of temperature. The results of this fitting procedure can be seen in Figure 5.6. We get good fits with $\chi^2 \approx 1.1$, and the parameter ν is found to follow a temperature activated behaviour, see Figure 5.6.

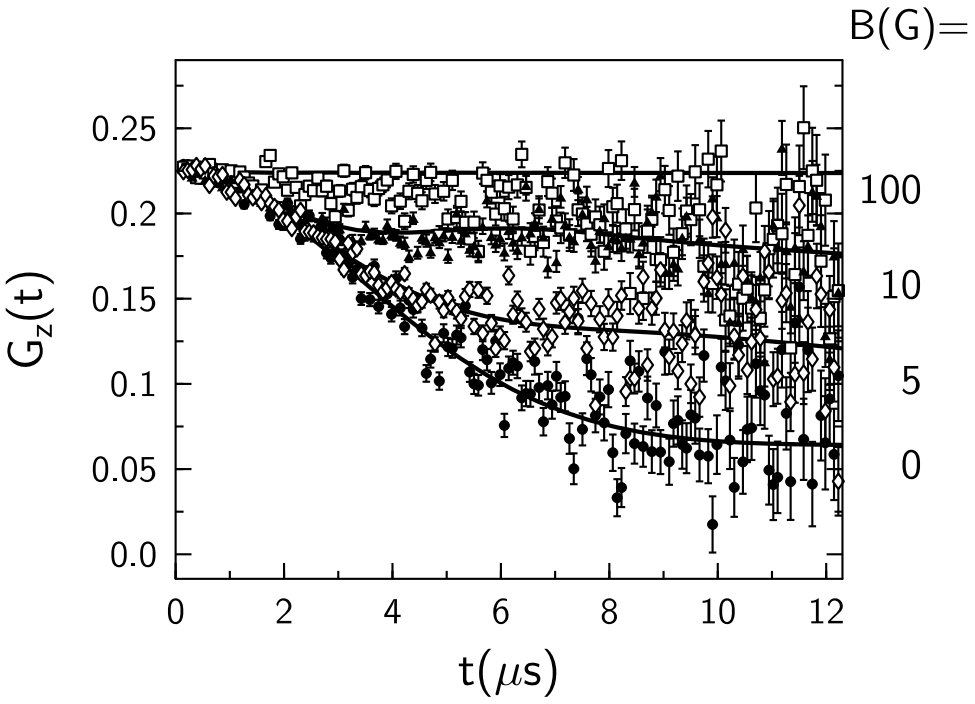

Figure 5.5: Longitudinal field measurements on CaV_4O_9 at 180 K. The full lines are curves calculated from Equation 2.22 with the parameters $\nu = 0.20\ \mu s^{-1}$, $\Delta = 0.21$ G and B as indicated in the Figure. There was no additional free parameter.

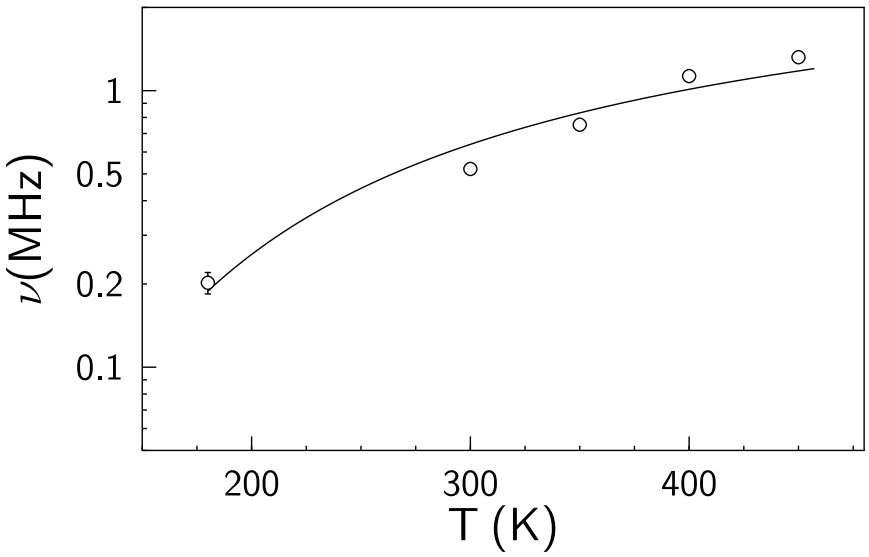

Figure 5.6: Nuclear spin fluctuation rates, extracted from the fits to Equation 2.22. The solid line shows a temperature activated behaviour fit.

Region II: Below T_{sg}

Below T_{sg} the electronic spins which were in the excited triplet state begin to freeze out and fall into the singlet ground state. Between 30 K and 100 K we find $\beta \sim 1$ and 0.17 $\mu s^{-1} < \lambda < 0.30$ μs^{-1} (Figure 5.4), where the relaxation rate rises with decreasing temperature. We note that in a μSR experiment [Blun97] on the spin-Peierls compound MEM(TCNQ)$_2$ a similar result is seen below the spin-Peierls transition (which results in the formation of a spin-gap). In CaV_4O_9 the increase in the relaxation is similar to NMR results [Tani95] for T_1^{-1} in the temperature region 100 K – 30 K. A fit to a phenomenological function $\lambda(T) = A \ln(\Delta_p/T)$ gives the parameters $A = 0.21(1)$ μs^{-1} and $\Delta_p = 378(21)$ K. Two main effects may influence the change in the relaxation rate. First, fewer and fewer electronic spins will be excited with decreasing temperature, thereby decreasing the effective field at the muon site. Second, the spin fluctuations will slow down, consistent with the increasing exponential relaxation rate below T_{sg} [Blun97]. In the same temperature region the susceptibility decreases with decreasing temperature (see Figure 5.2).

Region I: The Low Temperature Region Below 30 K

Since the ground state is non-magnetic, there should be no spin relaxation in ideal spin-gap systems at low temperatures. If relaxation is observed there are two possible mechanisms: defect spins, resulting from impurities or lattice imperfections, or triplet excitations at finite temperatures. As the temperature is lowered, more and more of the electrons go into the non-magnetic singlet states and hence do not affect the muons. In this low temperature regime, in which the electronic spins are frozen out, the dominant mechanism for relaxing the muon polarization comes from dilute defect spins. At temperatures below 30 K the shape of G_z is root-exponential ($\beta \sim \frac{1}{2}$, Figure 5.4), which is characteristic of a dilute spin system, see [Uemu85] and Chapter 2.4.3. This freezing out of spins below 20 K coincides with the vanishing of the spin-susceptibility (Figure 5.2 and Ref. [Tani95]) and the saturation of the transverse relaxation rate in NMR [Koda97]. If we assume a Markovian modulation of the defect spins with spin fluctuation rate ν, the field H at the muon site will follow the same time correlation function, i.e.

$\langle H(t)H(0)\rangle / \langle [H(0)]^2\rangle = \exp(-\nu t)$. A detailed treatment [Uemu85] yields

$$G_z(t) = A_S e^{-\sqrt{4a^2 t/\nu}} + A_{Ag} \tag{5.5}$$

for $\nu/a \gtrsim 5$. Here a is a measure for the average field at the muon site. Assuming that the defect spin fluctuations are thermally activated, $\nu(T)/\nu(0) = \exp(-\Delta_d/T)$, where Δ_d is the activation temperature for defects spin fluctuations, we find that for a fit below 30 K, $\Delta_d = 28.5\,\text{K} \pm 4.5\,\text{K}$. We can give a lower limit of the defect spin fluctuation rate in this temperature region by doing a free fit to the root exponential in Equation 5.5 and extracting the parameter $\lambda = 4a^2/\nu$. Together with the condition $\nu/a \geq 5$ we can deduce that at 5 K the fluctuation frequency ν of the defects has a lower limit of 1 MHz.

5.5 Conclusion

The form of the muon-spin relaxation in CaV_4O_9 is strongly temperature dependent. At temperatures below 30 K a root exponential behaviour is seen for the muon spin relaxation function, which can be attributed to defect spins. At higher temperatures spin fluctuations begin to increase, and the exponential relaxation rate decreases with increasing temperature. Eventually the spin fluctuation rate results in relaxation whose characteristic time exceeds the muon time-window and we are sensitive to nuclear spins only, resulting in a Gaussian relaxation. At temperatures above 160 K we see the onset of either muon hopping or increasing nuclear spin fluctuations, resulting in the dominance of an exponential relaxation again.

Even though CaV_4O_9 does not show short-range magnetic order, in contrast to $La_{2-x}Sr_xNiO_{4+\delta}$ (Chapter 3) and $Sr_2LnMn_2O_7$ (Chapter 4), it provides us with an example where a great deal of different subtle relaxation effects can be studied.

Chapter 6

Muon Studies of Polybutadiene

Contents

After having considered examples of two-dimensional magnetic systems in the previous chapters, we now have a closer look at the one-dimensional material polybutadiene (PB). This system is a polymer without side-chains and has the chemical formula $(-CH_2-CH=CH-CH_2-)_n$.

In organic systems implanted muons usually pick up an electron to form muonium. Muonium addition to a polymer can result in a muon bonded to the polymer plus an associated polaron. The implanted muon can appear in various states: diamagnetic, weakly paramagnetic and strongly paramagnetic (see also Chapter 2). In the diamagnetic case there is no unpaired spin density at the muon site. In the weakly paramagnetic case the associated electron escapes from the muon and diffuses through the polymer with a finite probability of returning to the muon if not being trapped elsewhere. For the strongly coupled paramagnetic case, the electron remains trapped near the muon (e.g. in the case when the electron diffusion is small in the polymer), and the muon spin relaxation will be dominated by the motion of the polymer itself. Muon implantation has been used in the past to gain information on polaron diffusion processes in conducting polymers [Naga84, Ishi85, Risc92, Haye95, Jest97, Prat97b, Prat97c, Prat99].

In many polymers and organic materials, there is more than one possible paramagnetic state, corresponding to more than one muon site. As we shall see later, we can find only one paramagnetic state in PB.

The data presented below are interesting in the context of conducting polymers and the possible influence of polymer motion on the spin relaxation of the muon. Polybutadiene is also of relevance because it exhibits a glass transition at $T_g = 171$ K, and the muon spin relaxation data reflects this transition.

This chapter is arranged as follows: In section 6.1 I give some theoretical background. In particular, I present the models for interaction of muons with systems where radicals are created through the implantation of a muon. Transverse field measurements and avoided level crossing (ALC) measurements can elucidate the nature of such a radical state. In section 6.2 I introduce PB and present its physical properties. In the following sections 6.3 (TF measurements) and 6.4 (ALC measurements) I make use of the results of the first section, and the muon state in the polymer is identified. The longitudinal field data is then presented (section 6.5), and the relation to the glass transition in PB is made. The last section (6.6) contains concluding remarks.

object	gyromagnetic ration
electron (e)	$\gamma_e = 2\pi \times 2.799 \times 10^{10}$ Hz/T
muon (μ)	$\gamma_\mu = 2\pi \times 1.355 \times 10^{8}$ Hz/T
proton (p)	$\gamma_p = 2\pi \times 0.4258 \times 10^{8}$ Hz/T

Table 6.1: Gyromagnetic ratios for electron, muon and proton

6.1 Theory of μSR in radical systems

If a muon enters an organic material it can usually pick up an electron to form muonium (or undergo muon - muonium cycles), which can be viewed as a light isotope of hydrogen. This muonium may then break a double bond and create a radical electron (for an illustration for PB see Figure 6.2 on page 104). The Hamiltonian which describes this state must include the spins of the muon, the unpaired electron and any nearby magnetic nuclei, and may be written as

$$H = -\gamma_\mu \, \mathbf{S} \cdot \mathbf{B} + \gamma_e \, \mathbf{I} \cdot \mathbf{B} + \mathbf{S} A_\mu \, \mathbf{I} + \sum_k \mathbf{I} A_k \, \mathbf{I}^k - \sum_k \gamma_k \, \mathbf{I}^k \cdot \mathbf{B} \, . \qquad (6.1)$$

Here $A_\mu$and A_k are the electron hyperfine interaction tensors for the muon and the nuclei, $\mathbf{I}^k$ is the nuclear spin operator and γ_k is the corresponding gyromagnetic ratio, which is $2\pi \times 42.58$ MHz/T for protons (see also Table 6.1). The other symbols are explained in Chapter 2.3.2, except that we here neglect factors of $\hbar$ for clarity. For isotropic hyperfine interactions, the hyperfine tensors can be replaced by real numbers. We have neglected quadrupolar interactions (since we are dealing with nuclear spins of 1/2 or 0) and terms of Knight-shift character.

In the experiments which we are considering the observation of radicals in the dilute limit is possible. We then have two contributions to the hyperfine interaction of any muon (or nucleus) in an organic radical: the Fermi contact interaction of any unpaired electron spin, which is independent of the orientation of the radical in a magnetic field, and the dipolar magnetic interaction of the point-like muon (or nucleus) and the unpaired electron spin (which is distributed in space). The latter interaction reflects the distribution of the electron spin and is anisotropic. Reorientational dynamics often average the anisotropy partially or wholly, and often it is appropriate to assume a hyperfine tensor with axial

symmetry. The hyperfine interaction tensor is the sum of an isotropic part $A_\mu^{\rm iso}$ and a traceless dipolar part, D_μ. In the case of axial symmetry the latter can be described by a single parameter $D_\mu^{\parallel}$, the largest principal value. The other two principal values are $D_\mu^{\perp} = -D_\mu^{\parallel}/2$ [Prat97a].

6.1.1 Transverse Fields

We now consider the Hamiltonian in Equation 6.1 for the case of a transverse magnetic field. As a basis of the spin Hilbert-space we take the product of the individual spin functions, $|\chi\rangle = |\chi_\mu \chi_e \chi_k\rangle$, where for simplicity we consider the case of only one nearby nuclear spin. The eigenfunctions of the isotropic Hamiltonian can then be written [Rodu81] as

$$|m\rangle = \sum_i c_{im} |\chi_i\rangle \tag{6.2}$$

where c_{im} are the expansion coefficients. We then can write the x-component of the polarization (see also Chapter 2 and Appendix A) as

$$P_x(t) = \frac{1}{4} \sum_m \sum_{n<m} \left| \sum_{ij} c_{im}^* c_{jn} \langle \chi_i | \sigma_x | \chi_j \rangle \right|^2 \cos(\omega_{nm} t)\,. \tag{6.3}$$

If we recall that the muon spin-up and spin-down states are not eigenstates of σ_x we can easily see that for P_x there are contributions from states for which the muon-spin is not the same. In the high field limit, when $\gamma_e B \gg A_\mu, A_k$, the spins are decoupled from each other and the eigenstates become equal to the individual product states. The coefficients c_{ij} are then all equal to one or zero. We get the selection rules $\Delta m_S = \pm 1,\ \ \Delta m_I = 0,\ \ \Delta m_k = 0$, where $m_{S,I,k}$ is the eigenvalue of the z-component of $\mathbf{S}$, $\mathbf{I}$ or $\mathbf{I}^k$. In these high fields, the energy of the Hamiltonian can be expressed as

$$E_n/\hbar = \gamma_e B m_I - \gamma_\mu B m_S - \sum_k \gamma_k B m_k + A_\mu^{\rm iso} m_I m_S + \sum_k A_k^{\rm iso} m_I m_k\,. \tag{6.4}$$

Here $A_{\mu,k}^{\rm iso}$ are the isotropic hyperfine interactions values. For high transverse fields, where the nuclei in the molecule are decoupled from the muon and can be

neglected, the transition frequencies are given [Rodu81] by

$$\nu_{1,2} = \left| \nu_m \pm \frac{1}{2} A_\mu^{\mathrm{iso}} \right| \tag{6.5}$$

with

$$\nu_m = \frac{1}{2} \left(\sqrt{(A_\mu^{\mathrm{iso}})^2 + (\nu_e + \nu_\mu)^2} - \nu_e + \nu_\mu \right) \tag{6.6}$$

and $\nu_\mu = \gamma_\mu B/(2\pi)$. For high fields, $\nu_m \approx \nu_\mu$ is a good approximation. The two frequencies $\nu_{1,2}$ in Equation 6.5 are seen in $P_x(t)$, and a Fourier analysis can provide us with their values. The magnitude of the Fermi contact interaction constant A_μ^{iso} is then given by the sum of these frequencies. We note that for an *anisotropic* Hamiltonian the expression gets more complicated. For the axially symmetric case we can simply make the replacement

$$A_\mu^{\mathrm{iso}} \longrightarrow A_\mu^{\mathrm{iso}} + D_\mu^{\perp}(1 - 3\cos^2\theta) \tag{6.7}$$

where θ is the axis between the vector connecting the (point) dipole giving rise to the dipolar interaction and the muon spin on the one side and the external magnetic field on the other side. For a polycrystalline sample, $\langle \cos^2\theta \rangle = 1/3$ and there is no contribution from the second term of the right hand side in Equation 6.7. However, if the sample is oriented, and if motional processes do not average out the anisotropy (on the muon time scale), then a change of the sample orientation should lead to a change of the location of the resonance signal. At the angle of 54.7° the only contributing term is the isotropic part of Equation 6.7.

Usually there will be more than two frequencies in the spectrum. These additional frequencies can have several origins. If there are several muon sites in the system investigated, then the muons at these various sites will have different hyperfine constants, and therefore more than one pair of frequencies will be seen in the spectrum. Some muons may not be in a paramagnetic state and therefore the free muon Larmor frequency ν_μ will also be apparent in the spectrum. This frequency might be seen anyway, due to muons coming to rest in the silver backing plate. The experiments described below were performed at PSI, and there is also a contribution of the cyclotron operating frequency of 50 MHz (and harmonics) to the spectrum. When analysing data, these artefacts must be taken into consideration.

The nuclear terms (the third and fifth term in Equation 6.4) can often be considered as small (i.e. $|A_\mu| > |A_k|$ and with use of sufficiently high fields), and perturbation theory then gives second order corrections [Rodu81].

Muonium in muonated radicals is often regarded as a light isotope of hydrogen (with $m_\mu \approx \frac{1}{9} m_p$, see Table 2.1 on page 9). In order to make a meaningful comparison of proton hyperfine interactions A_p (where we have taken $k = p$) and muon hyperfine interactions A_μ, the latter are often multiplied by the ratio of the magnetic moments of the muon and the proton, i.e.

$$A'_\mu = \frac{\mu_p}{\mu_\mu} A_\mu = 0.3141 A_\mu \,. \tag{6.8}$$

It is then possible to compare these values to those obtained for A_p (e.g. from ESR experiments). They will usually not be identical, since the different masses of hydrogen and muonium will have influence on bonding lengths and bonding angles and therefore also on the contact interaction [Vall96]. A typical relation is $A'_\mu = c \times A_p$, where $c \approx 1.3$, but higher values of c have been observed (e.g. $c = 1.74$ for ethene ($H_2C{=}CH_2$) [Rodu82]).

6.1.2 Avoided Level Crossing (ALC) measurements

We have seen in Chapter 2.4.4 how free muonium gets repolarized in a longitudinal magnetic field. The corresponding time-integrated polarization $P_z(B) = \int_{t=0}^{\infty} dt P_z(B,t)$ is shown in Figure 2.15 a) (page 33). For muon-substituted free radicals, resonances in the curve $P_z(B)$ are predicted. These resonances depend on the hyperfine couplings. The spin-Hamiltonian contains information about the distribution of the electron density at neighbouring nuclei. At high fields and at crossings of the magnetic energy levels in the Breit-Rabi diagram, the eigenstates are pure product states of the Zeeman states. However, when a third spin (the nuclear spin) is coupling to the electron and the muon spin, the corresponding Breit-Rabi diagram becomes complicated, and there are several (avoided) crossings of levels with varying field (see Figure 6.1). Typically the electron spin interacts strongly with the nuclear spin and the muon spin, while the direct coupling of the muon spin to the nuclear spin is small. Near avoided level crossings, the muon and nuclear near-Zeeman states couple to each other via their respective interaction to a third spin. The system is then not prepared in an eigenstate, and $P_z(t)$ is

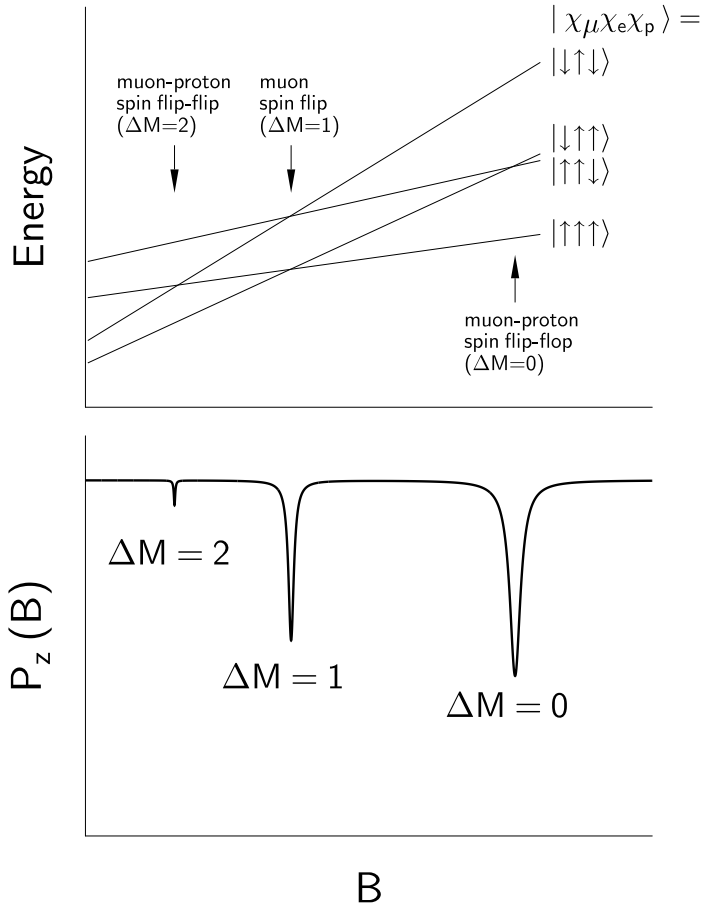

Figure 6.1: Upper panel: Scheme of high field energy level diagram of a three spin system (muon, electron, proton). The four "crossings" shown are in reality avoided level crossings. Lower panel: ALC resonances occur when states with opposite muon spin become near-degenerate in energy. After [Rodu93].

not time-independent any more. A component of it now oscillates at a frequency corresponding to the gap between the two levels. Then the time-integral of $P_z(t)$ is less then for the time-independent case. In the time-integrated $P_z(B)$ curve this leads to a dip. We can classify these resonances according to the difference in the total magnetic quantum number between the levels: $\Delta M = \Delta(m_S + m_I + m_k) = 0$, 1, 2.

- We do not consider further the type where $\Delta M = 2$, a muon-nuclear spin flip-flip transition. It is usually a weak and narrow transition and cannot be seen in our data.

- For $\Delta M = 1$, two states which have the same nuclear and electron spin

but different muon spins mix. This is a muon spin flip. This transition is only possible in the presence of muon hyperfine *anisotropy*. Assuming an axially symmetric case, the relevant time for any anisotropy-averaging motional process is given by the inverse anisotropy, $1/D_\mu^\perp$. The resonance is centred at a magnetic field

$$B_r = \left| \frac{A_\mu^{\rm iso}}{2\gamma_\mu} \right| . \tag{6.9}$$

The level crossing is avoided by coupling of the two Zeeman states through the dipolar part of the hyperfine interaction [Kief86]. This result can be compared to the hyperfine coupling measured by TF measurements, see above. In a polycrystalline sample the anisotropy D_μ will give rise to an asymmetric ALC lineshape [Rodu93]. The mean muon spin precession frequency "on resonance" in high fields is

$$\omega = \frac{D_\mu^\perp}{2} . \tag{6.10}$$

With decreasing axial anisotropy the resonance narrows and loses intensity as it becomes smaller than the inverse muon lifetime $1/\tau_\mu = 0.45$ MHz [Treg96].

- The $\Delta M = 0$ transition occurs when the muon and nucleus exchange spin polarization (a muon-nucleus spin flip-flop). The crossing of the levels is avoided by indirect coupling of both Zeeman states to a third one. This avoided level crossing occurs at a magnetic field [Hemi86]

$$B_r(M) = \left| \frac{A_\mu^{\rm iso} - A_k^{\rm iso}}{2(\gamma_\mu - \gamma_k)} - \frac{(A_\mu^{\rm iso})^2 - 2M(A_k^{\rm iso})^2}{2\gamma_e(A_\mu^{\rm iso} - A_k^{\rm iso})} \right| , \tag{6.11}$$

where $I^k \geq M \geq (-I^k + 1)$ and I^k is the spin of the nucleus. If the nucleus is a proton, i.e. $I^k = \frac{1}{2}$, the equation simplifies to

$$\begin{aligned} B_r &= \frac{1}{2} \left| \frac{A_\mu^{\rm iso} - A_p^{\rm iso}}{\gamma_\mu - \gamma_p} - \frac{A_\mu^{\rm iso} + A_p^{\rm iso}}{\gamma_e} \right| \\ &= \frac{1}{2} \left| \frac{\gamma_e - \gamma_\mu + \gamma_p}{\gamma_e(\gamma_\mu - \gamma_k)} A_\mu^{\rm iso} - \frac{\gamma_e + \gamma_\mu - \gamma_p}{\gamma_e(\gamma_\mu - \gamma_k)} A_p^{\rm iso} \right| . \end{aligned} \tag{6.12}$$

The width of the resonance of the ALC spectrum can be broadened and weakened by the presence of relaxation. Equations 6.9, 6.11 and 6.12 are valid for the case of isotropic coupling. In the case of axial anisotropy we have to make the replacement

$$A^{\mathrm{iso}}_{\mu,k,p} \longrightarrow A^{\mathrm{iso}}_{\mu,k,p} - D^{\perp}_{\mu,k,p}(1 - 3\cos^2\theta) \tag{6.13}$$

where the symbols have the same meaning as in Equation 6.7 on page 99.

ALC spectroscopy can be performed under the conditions of an LF experiment. However, since the time-dependence of the muon polarization is not needed, one can perform time-*integral* muon experiments. At a pulsed muon facility (see Chapter 2.2.1), where all the muons arrive at essentially the same time, there is no advantage in not measuring the time dependence. In contrast, at a continuous facility (see Chapter 2.2.2) the muon beam intensity is normally limited by the restriction to have only one muon in the sample at any time. At continuous sources there is usually a potential of at least one order of magnitude higher muon intensity [Brew94]; hence by using the time integral technique one profits from the higher count statistics at the cost of time information. We have performed such experiments at the ALC instrument of the PSI facility in Switzerland (see Chapter 6.4), where the typical rate is of the order of 4×10^6 muons/second.

6.2 Characteristics of polybutadiene

Polybutadiene (PB) has the chemical formula $(\text{–CH}_2\text{–CH=CH–CH}_2\text{–})_n$ and is a polymer without side-chains (see Figure 6.2). PB is a non-conducting polymer which contains π-bonds like conducting polymers such as polyaniline or polyacetylene [Prat97b, Prat97c]. These π-bonds are, however, separated by non-conjugated segments which inhibit long-range electron motion. These systems should thus be good reference systems to study the direct effect of polymer dynamics on the muon relaxation. As we shall see below, the dynamical effects related to the polymer motion are seen in both the diamagnetic and the paramagnetic signal in PB.

Although the dynamics of PB and other polymers has been studied intensively with a variety of methods it is not well understood [Gedd95, Rich88a]. Viscosity and chain dynamics in polymers are unique phenomena, and the behaviour is

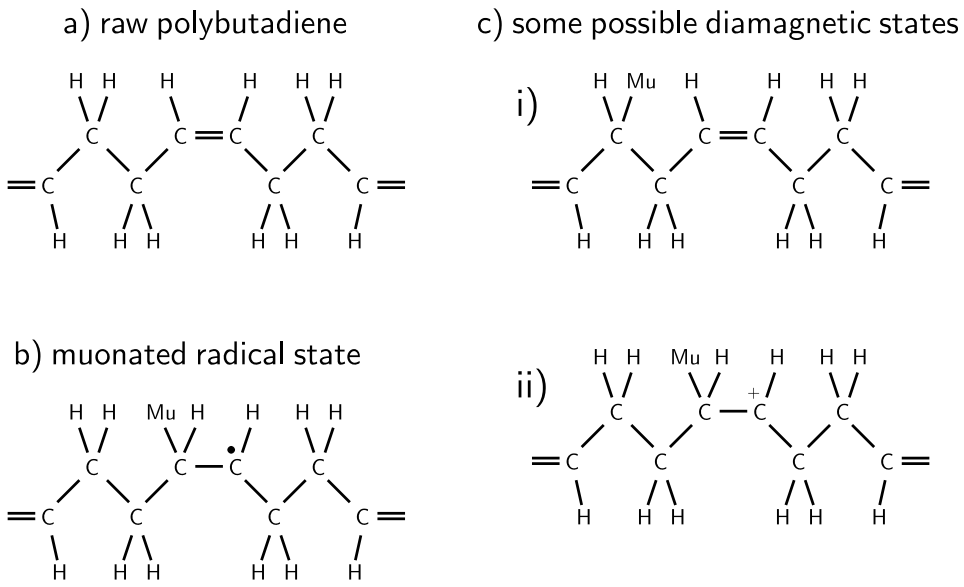

Figure 6.2: a) Structure of cis-polybutadiene b) Cis-polybutadiene with a muonium that has broken a double-bond and is attached to a carbon atom. This is the radical state. The electron is located at the adjacent carbon atom. c) Some possible diamagnetic states, where there is no unpaired electron spin density at the muon. In i) a proton is replaced by a muon. ii) is the same situation as b), with the electron removed from the nearby carbon atom.

determined by intermolecular and intramolecular interactions.

Polymers show a slowing down of dynamics with decreasing temperature. They are good glass formers as a consequence of structural irregularities. Even crystalline polymers show some amounts of amorphous regions, because they cannot be fully crystallised [Kana92]. Below the glass transition, configurations of the polymer are frozen into metastable states. These states are viewed as being separated by barriers in phase space, and there is a wide distribution of relaxation times between these states. A glass transition can be observed in PB at a temperature of $T_g = 171$ K. Variation of transition temperatures of up to ± 10 K have been reported in the literature, depending on the method used to study the glass transition and depending on the specific PB characteristics, such as the mass average molecular weight (or the chain length), and also depending on external parameters such as the cooling or heating history. The freezing process for glasses is accompanied by singularities of derivatives of thermodynamic potentials

such as specific heat, and singularities in transport properties are observed (e.g. the shear viscosity). Glassy polymers show very little segmental mobility, and conformational changes are confined to small groups of atoms [Gedd95].

The effect of relaxation processes on many properties in a glass can be described by a stretched exponential function, i.e. $\propto \exp\{(t/\tau)^{\beta}\}$ ("Kohlrausch law") [Bähr93, Aoua97]. Fast relaxation-like excitations are seen in many glasses. Low-temperature properties such as tunnelling states and specific heat and heat conduction anomalies [Phil81] are common features. Low-energy excitations have been observed, resulting from tunnelling between metastable states typical for disordered solids [Free86, Löhn86]. Stretched exponential functions can be used to fit a multitude of different physical phenomena which are related to relaxation processes.

Neutron scattering measurements on PB [Rich88b] have shown that the structure factor above T_g follows a stretched exponential law. Fast motional processes become effective already well below T_g [Rich88b]. There also seems to exist a scaling behaviour between the macroscopic viscosity relaxation and the microscopic dynamics [Rich88b]. In this context PB has become a model polymer glass system. Later work [Rich92], however, reported a decoupling of the microscopic and macroscopic time scales below around $T_c = T_g + 40$ K. Neutron data have for example been analysed with a vibration-relaxation model [Buch95]. Fast and slow modes in the melt have been assigned to the damped vibrational motion of C–C-bond torsion and local single bond rotations [Kana92]. It should be noted that these neutron scattering measurements probe the time window accessible to them, thus concentrating on fast ($10^{-13} - 10^{-9}$ s) relaxation processes [Kana91]. Motional models for chain dynamics were based on conformational changes (i.e. changes in the shape of a given molecule) which propagate along the chain, and are characterized by a correlation time. ^{13}C NMR measurements [Deje89] above the glass transition have confirmed the existence of conformational jumps, the diffusional motion of these bond orientations along the chain being only slightly damped. The correlation time of the conformational changes (the microscopic details are not completely elucidated) could be satisfactorily compared to a Williams-Landel-Ferry expression, see Equation 6.19, although the similarity to the values of PB was not as good as to those of polyisoprene.

The experiments described below were performed at the PSI and the ISIS facilities. The transverse high field experiments were performed at the GPD in-

strument (PSI), the longitudinal field experiments at the RIKEN beamline of ISIS, and the ALC experiments at the ALC instrument (PSI). A commercial sample (Aldrich) of 1,4-cis-polybutadiene (98% cis) with a mass of 100 g was used. The mass average of the molecular weight $M_W = 2 - 3 \times 10^6$ g/mol, and the temperature of the glass transition is $T_g = 171$ K (supplier's specifications).

6.3 TF measurements on PB

For the TF measurements, which were performed at the General Purpose Decay (GPD) beamline of PSI, Switzerland, the sample was mounted on a silver backing plate in a CCR. The variable degrader of the GPD instrument was set to a value where the optimum positron counting rate was obtained. With this setting most of the incoming (decay) muons lose sufficent energy in the degrader to stop in the sample and not to penetrate it. Most measurements were taken at a transverse magnetic field of 0.3 T.

In order to analyse the resulting muon spin rotation signal (for an example see Figure 6.3) it is useful to decompose it into the various oscillatory components. The obvious way to do this is a numerical Fourier Transform. The Fourier Transform of the measured data was obtained with the use of a Gaussian apodisation with a time constant of 4.4 μs. As an example, the Fourier Transform of the direct signal of Figure 6.3 b) is shown in Figure 6.4.

In order to enhance radical signals above the noise level it can be of advantage [Reid90a] to define a correlation spectrum C, which is a function of frequency. For each (hypothetical) A_μ in the frequency range a corresponding upper and lower frequency $\nu_{1,2}$ is calculated according to Equation 6.5. The Fourier powers $P(\nu_1)$ and $P(\nu_2)$ at these frequencies are then multiplied to define the correlation spectrum

$$C(A_\mu) = C(\nu_1 + \nu_2) = P(\nu_1)P(\nu_2)\,. \tag{6.14}$$

The correct A_μ will then be indicated by a peak in the correlation spectrum. However, care must be taken in the analysis of the data, since additional peaks in the Fourier spectrum (i.e. the diamagnetic signal, the cyclotron operating frequency and its harmonics etc.) might give rise to a wrong A_μ assignation. In Figure 6.5 we can see the correlation spectra of the Fourier transforms for the

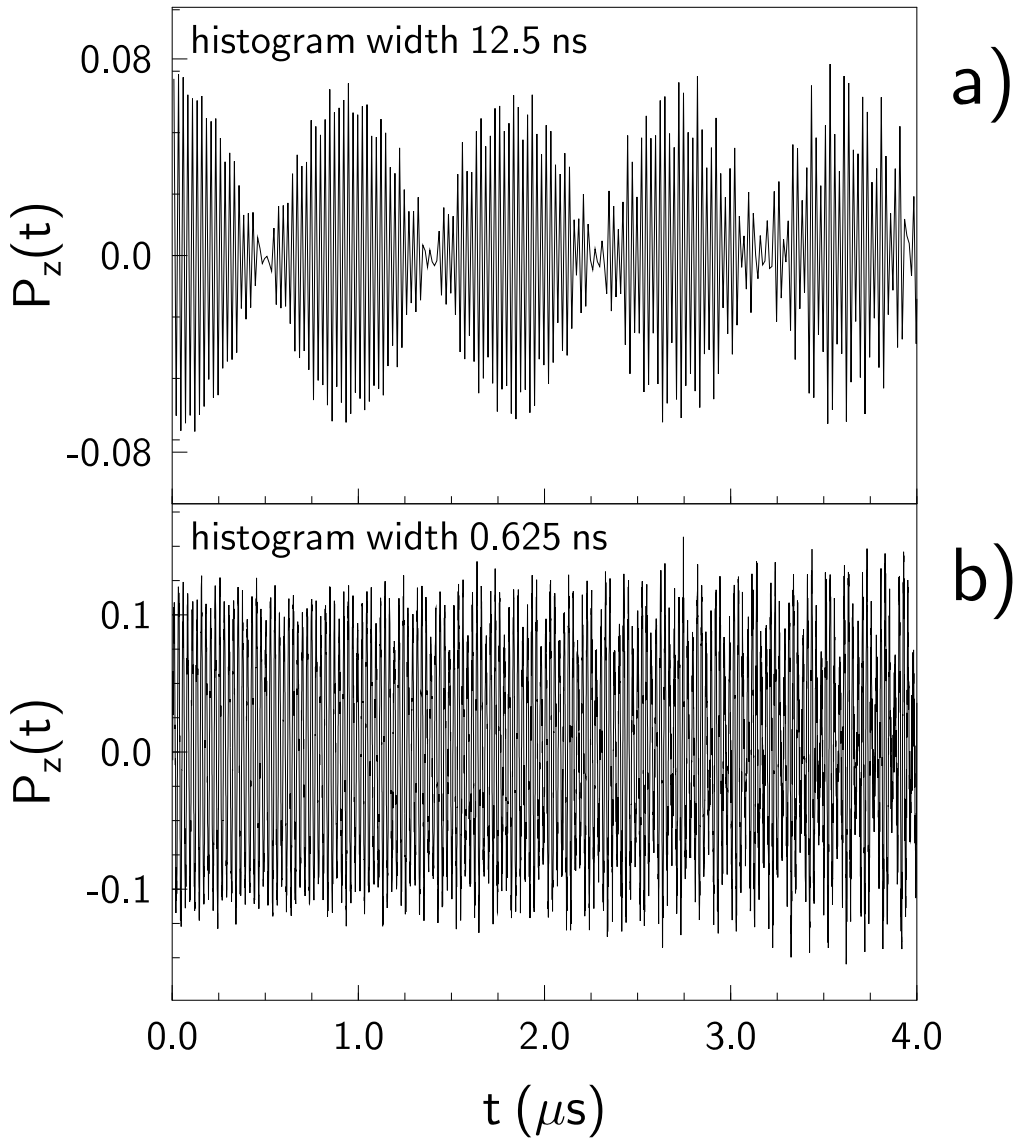

Figure 6.3: TF data in PB at a temperature of T = 338 K with two different time resolutions: a) time bin widths of 20 × 0.625 ns and b) time bin widths of 0.625 ns.

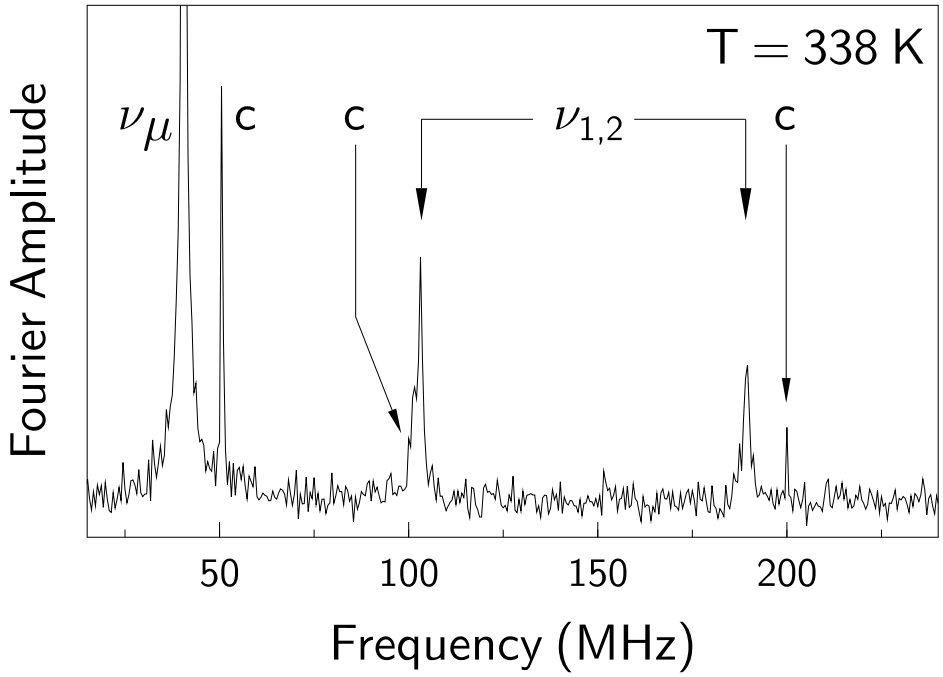

Figure 6.4: TF Fourier Transform signal in PB at a temperature of T = 338 K, see Figure 6.3 b). Note the peaks in the spectrum due to the radical signal (ν_1 and ν_2) and due to the diamagnetic signal (ν_μ). There are also narrow peaks around 50 MHz and its harmonics (c). This is due to the cyclotron operating frequency, see text.

TF 3 kG measurements. The hyperfine constant A_μ shifts to higher frequencies with decreasing temperature. Such a temperature dependence has been observed in many organic systems before [Rodu82, Flem97], and we can attribute it to a change in bond lengths and angles with temperature.

In order to model more accurately the behaviour of the hyperfine constant we fit the peaks of the correlation spectra with Lorentzians (see Figure 6.6 for an example). The resulting temperature dependence of the values obtained from the TF measurements is depicted in Figure 6.7 (open circles).

The temperature dependence of A_μ can be fitted by the empirical relation [Rodu82]

$$A_\mu(T) = A_\mu(T=\infty) + \{A_\mu(T=0) - A_\mu(T=\infty)\} \times \left\{1 - e^{-E_a/T}\right\} , \qquad (6.15)$$

where we have set $A_\mu(T=\infty) = (\mu_\mu/\mu_p)A_p = 67.21$ MHz. The underlying reason

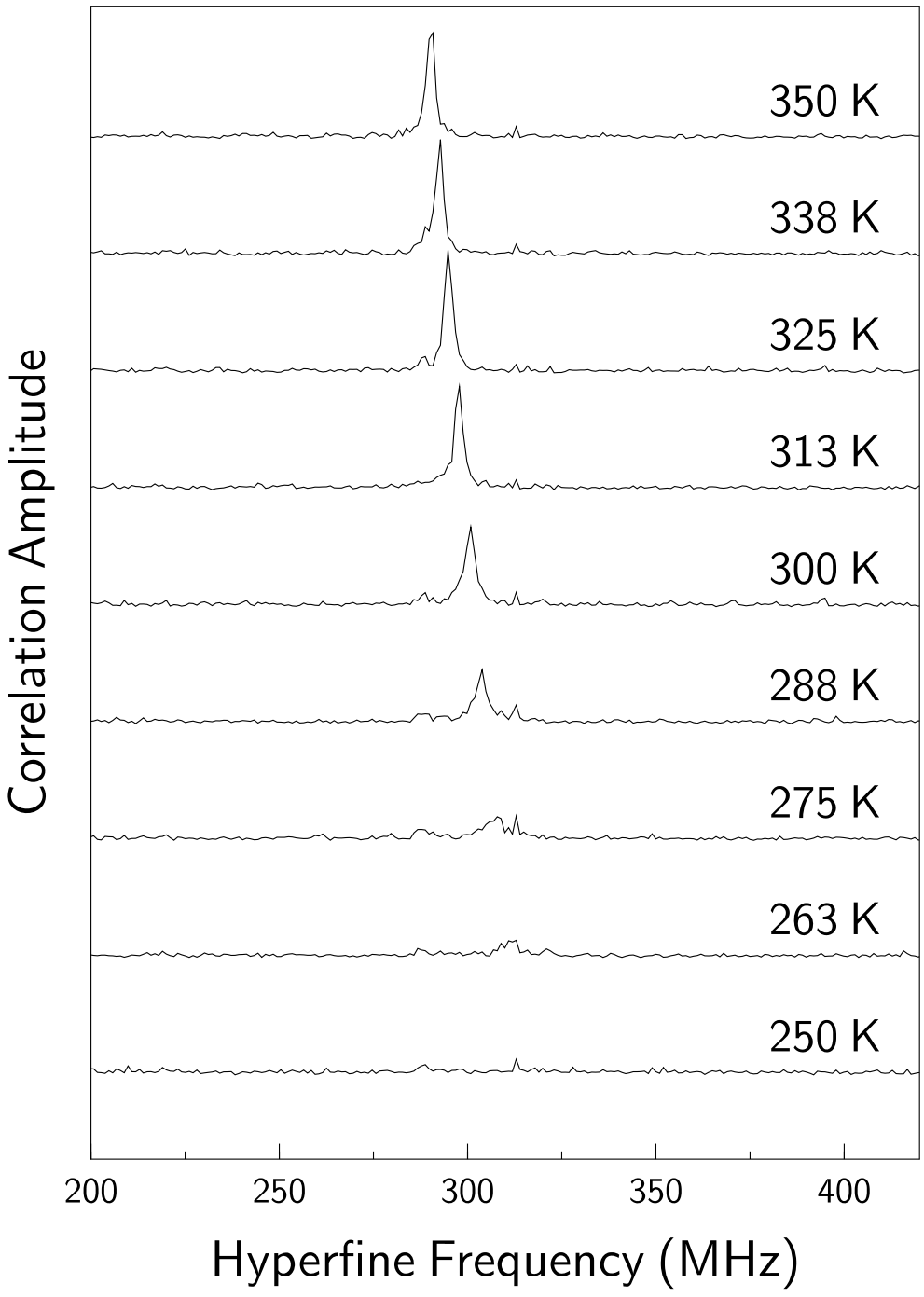

Figure 6.5: Temperature dependence of the polybutadiene correlation spectrum. The main peak in the spectrum corresponds to A_μ at the corresponding temperature. Spectra are vertically offset for clarity.

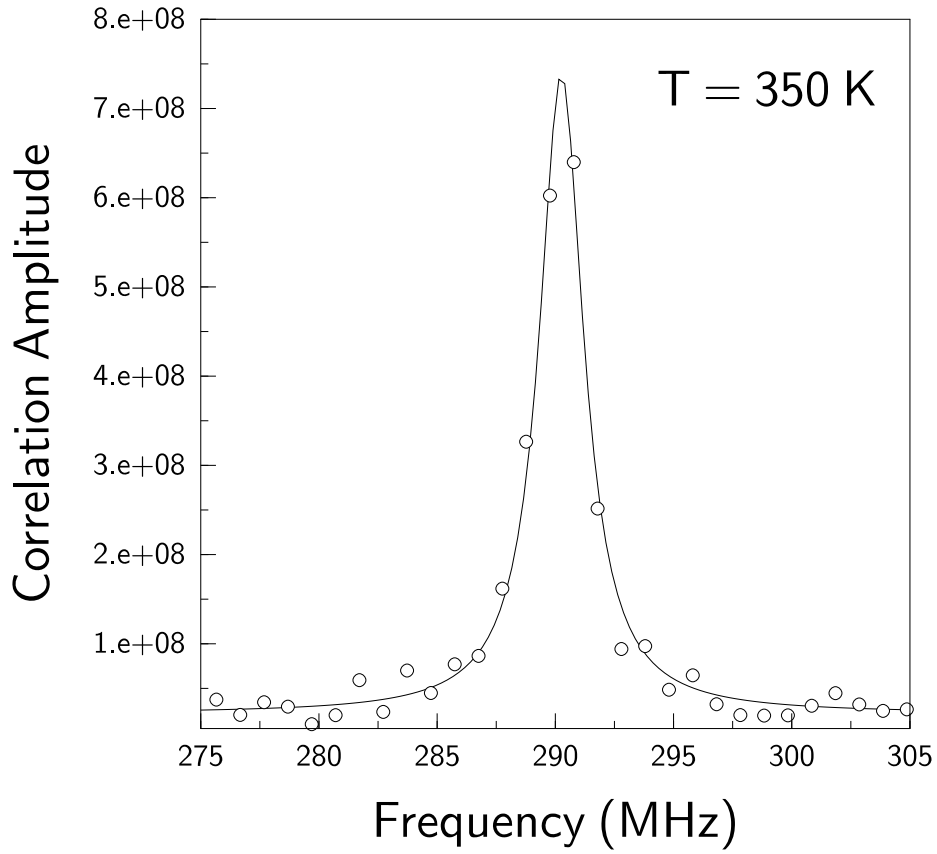

Figure 6.6: Plot of the correlation spectrum (circles) and of the Lorentzian fit (line) at the temperature T = 350 K.

for setting $A'_\mu(T = \infty) = A_p$ (see Equation 6.8) is that for infinite temperatures we expect quantum phenomena, such as the isotope effect, to become zero. The numerical value for A_p was obtained from the ALC experiment, see section 6.4. The fitted values are $A_\mu(T = 0) = 542(23)$ MHz and $E_a = 92(7)$ K, see also Figure 6.7. The relatively high uncertainty of the fitted values can be ascribed to the relatively small temperature region in which the fit was done, and which is also far away from T = 0 K. Caution must be taken in the interpretation of the data. As we mentioned in Chapter 6.1, these results are correct for an isotropic Hamiltonian. For an anisotropic Hamiltonian the situation is more complicated. Often it is sufficient to consider an axially symmetric Hamiltonian. Then the symbol A_μ in this section has to be replaced by $A_\mu^{\mathrm{iso}} + D_\mu^{\perp}(1 - \cos^2\theta)$. This is taken into consideration in the analysis in the following section.

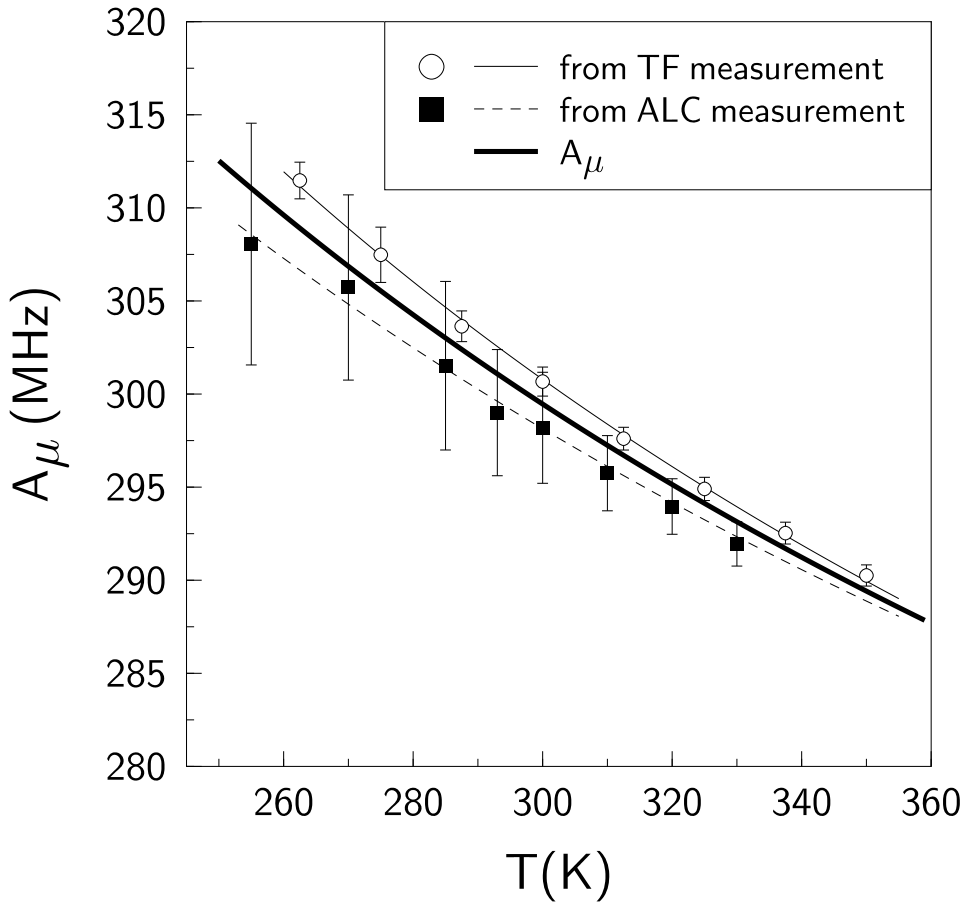

Figure 6.7: Temperature dependence of A_μ. The open circles are data extracted from the TF measurements, the full squares are data obtained from the ALC spectrum. The error bars are the widths of the Lorentzians fitted to the correlation spectra and to the ALC spectra (see section 6.4), respectively. The thin solid and dashed lines are fits of Equation 6.15. In the axially symmetric case the TF measurements give $A_\mu^{iso}+D_\mu^{\perp}(1\text{-}\cos^2\theta)$ and the ALC measurements give $A_\mu^{iso}-D_\mu^{\perp}(1\text{-}\cos^2\theta)$. Under this assumption, the thick line is the *isotropic* hyperfine interaction, A_μ^{iso} (see section 6.4, page 116).

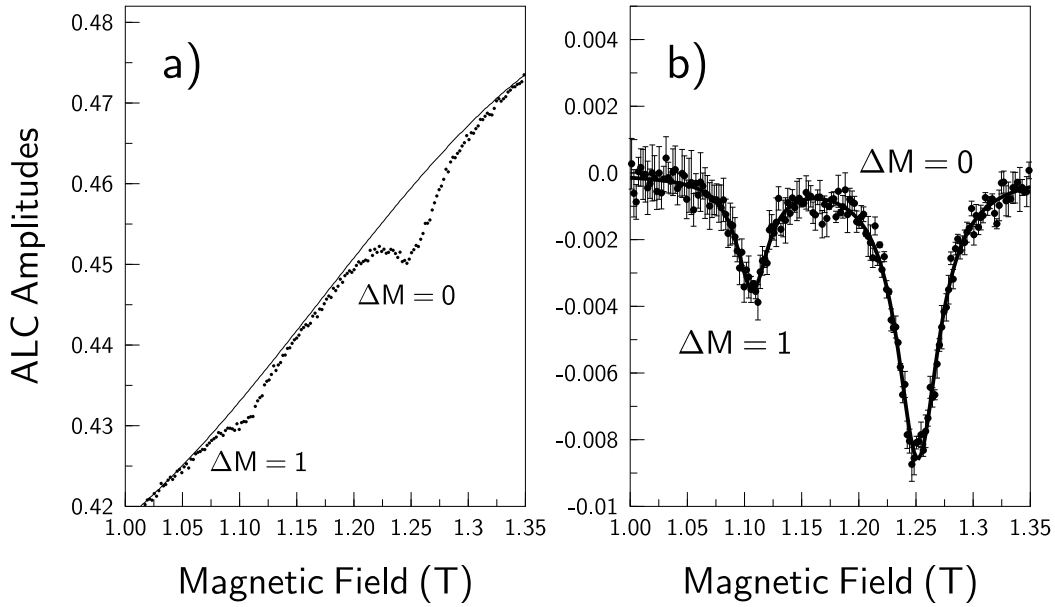

Figure 6.8: Example for an ALC background correction: a) the uncorrected data and the background (solid line) b) the data after subtraction of a cubic background. The solid line is a fit of two Lorentzians to the data.

6.4 Results of ALC measurements

For the analysis of the ALC results, a cubic background correction was subtracted from the data (see Figure 6.8).

We assume that the resonance is due to the coupling of the muon to the nearest proton, i.e. the one that binds to the same carbon (see Figure 6.2 b)) and is thus chemically equivalent. For this case, Equations 6.9 and 6.11, taken to first order, imply degeneracy of the $\Delta M = 1$ and $\Delta M = 0$ transitions *if* the hyperfine constants A_μ and A_p scale with the ratio of the muon and the proton magnetic moments, μ_p/μ_μ. As already mentioned in section 6.1.1 this is usually not the case, and therefore the separation of the resonance (see Figures 6.8 and 6.9) lines is a direct demonstration of this isotope effect. For example, the isotopic differences in vinylene carbonate have been ascribed [Rodu93] to the length of the C–Mu bond. In the model given there it is almost 5% larger than that of its equivalent C–H bond. This difference has also been ascribed to the increased alignment of the C–Mu σ-bond with the conjugated π system, caused by the change in bond orientation. In numerical simulations by R. Valladares [Vall96] it was shown for

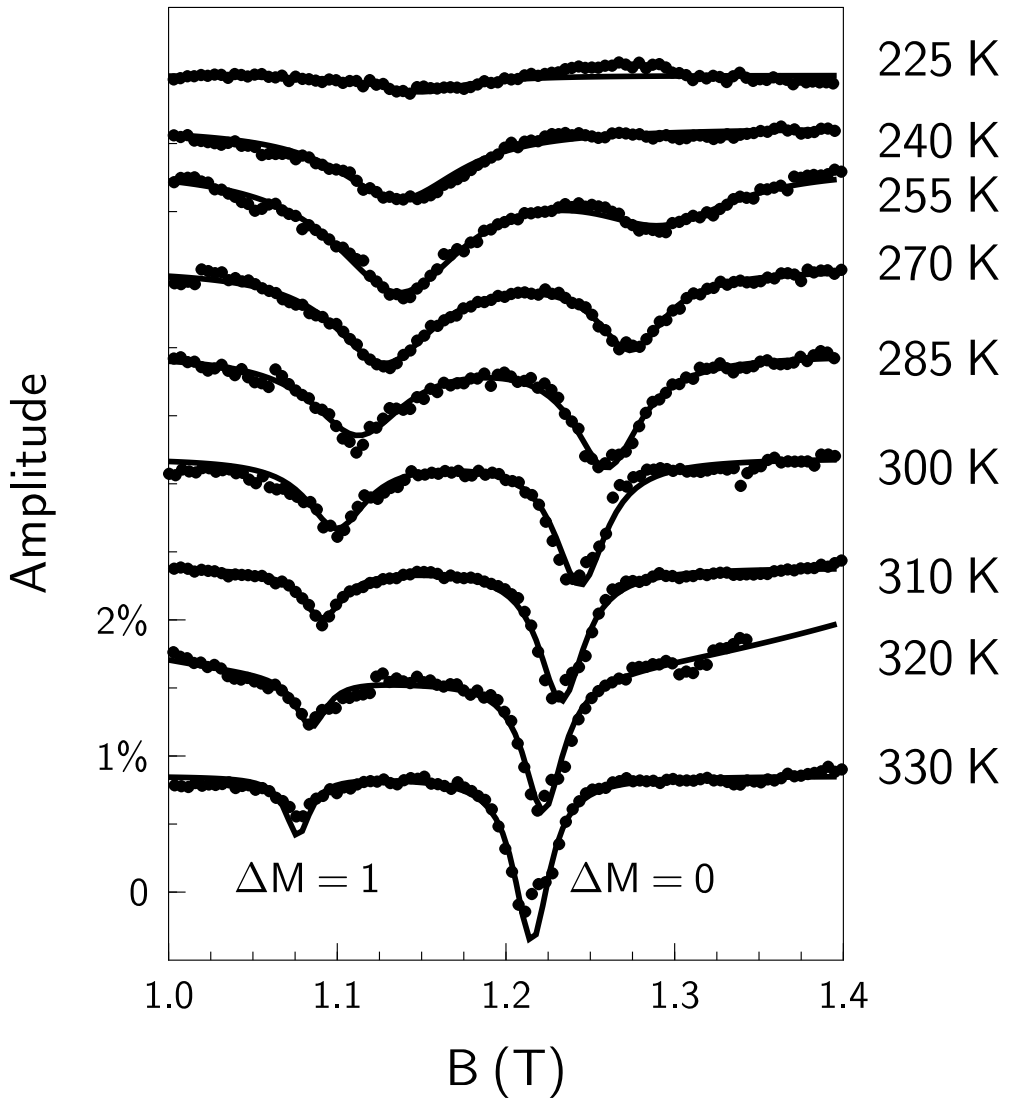

Figure 6.9: Temperature dependent ALC data for PB. The background is already subtracted (see Figure 6.8). The solid lines are a fit of two Lorentzians to the data. For clarity the data are offset for each temperature.

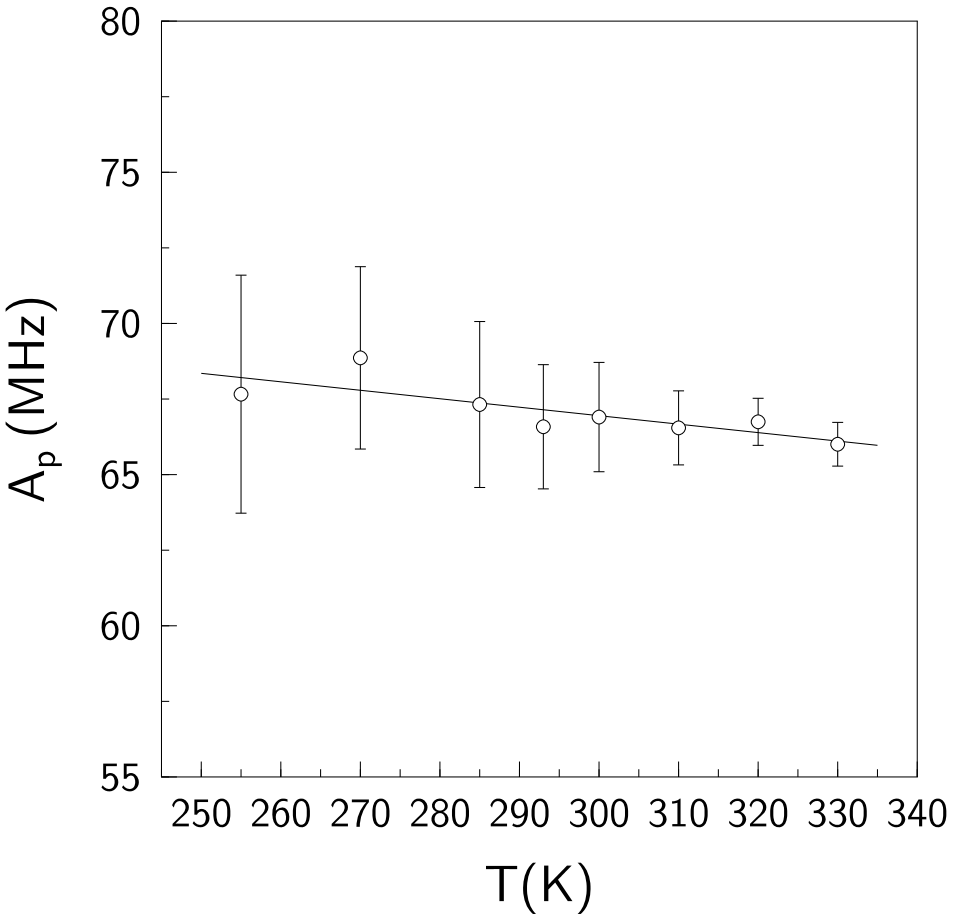

Figure 6.10: Temperature dependence of A_p. There is only a small temperature dependence of A_p apparent, with dA_p/dT = -0.028(9) MHz/K for a linear fit.

the isotope effect in benzene that both the change in bonding length and the change in bonding angle are important. A similar explanation for the isotope effect found in PB is plausible.

From the positions of the ALC resonances we can infer the hyperfine couplings A_μ (see Equation 6.9) and A_p (see Equation 6.12). The results are shown in Figures 6.7 and 6.10. The values for A_μ obtained from the ALC measurements show a similar temperature dependence as those obtained from TF measurements, but are not equal. We will elaborate on this difference in more detail below. There is only a small temperature dependence of A_p apparent in this temperature region, see Figure 6.10. For an linear fit we obtain a value of -0.028(9) MHz/K for dA_p/dT. A fit to a constant gives A_p = 67.21(32) MHz. This is not inconsistent with the picture of the differences for muon and proton presented above. Any kind of

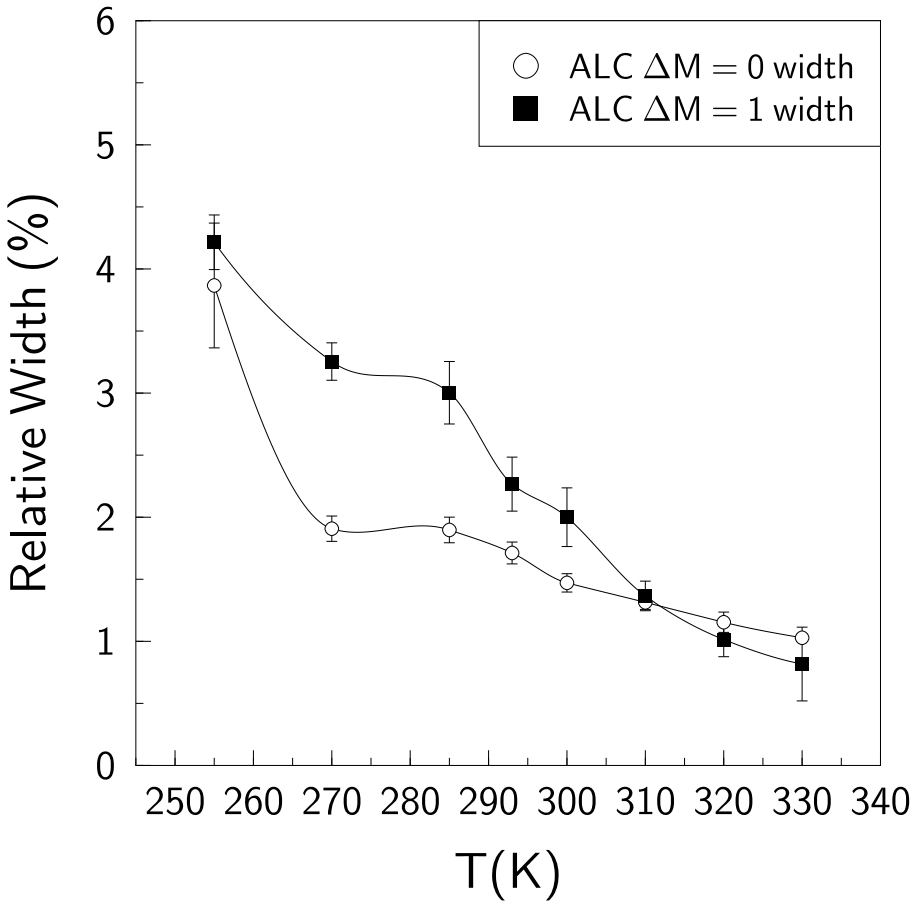

Figure 6.11: Temperature dependence of the width of the ALC resonances, as obtained from Lorentzian fits.

temperature dependence in the muon signal will be much less pronounced for the proton signal, due to the higher mass.

We now return to the features of the $\Delta M = 1$ signal in ALC and TF. The presence of the $\Delta M = 1$ resonance alone is proof for anisotropy. There is no obvious asymmetry in the shape of the $\Delta M = 1$ resonance, which would be expected for a large anisotropy [Treg96]. The ALC resonance can be seen up to the highest temperatures measured. The anisotropy $D_\mu^\perp$ might get averaged out by fast motion with a correlation time smaller than $1/D_\mu^\perp$ [Treg96], e.g. when raising the temperature. We indeed see a reduction in the $\Delta M = 1$ signal when raising the temperature. Higher temperature measurements would have to be performed to confirm this trend. The relative width of the ALC signals becomes smaller with increasing temperature (see Figure 6.11), hinting that indeed motional averaging

is taking place.

Lowering the temperature, however, we find that the resonances vanish below $\sim$ 240-250 K. This is counterintuitive. The fact that *both* signals disappear at lower temperatures is an indication that this disappearance is not related to an averaging process. From Figure 6.7 we can obtain a rough estimate of the anisotropy. In the following we again assume that certain features of the spectra can be described by an axially symmetric Hamiltonian. We note from Equation 6.5 with 6.7 compared to Equation 6.9 with 6.13 that an anisotropy should give rise to different shifts in the ALC and the TF signals. It is not unreasonable to ascribe the differences in A_μ to the anisotropy as it appears in these equations. Note that the "error bars" in Figure 6.7 are line widths of the signals, as obtained from the Lorentzian fits. The uncertainties in the peak positions are much smaller. With the above assumption we can calculate the correct A_μ (see the thick line in Figure 6.7) and consequently the expression $D_\mu^\perp(1-3\cos^2\theta)$. This is depicted in Figure 6.12. We see that the anisotropic part becomes smaller at higher temperatures, in agreement with what has been said above. This rough estimate assumes that there is some kind of orientation in the sample, otherwise the $\cos^2\theta$ term would average out the effect of the anisotropy on the position of the signals.

We now return to the vanishing of the signals at lower temperatures. Vanishing ALC signals when lowering the temperature have been observed before, see e.g. [Reid90b]. There this phenomena was ascribed to a lower radical formation rate at lower temperatures. In the absence of contradictory information a similar explanation seems plausible here. As the temperature is lowered, the motional processes in the polymer slow down, and this is accompanied by a reduction in the free volume of PB (see [Bart97]). The free volume decreases between $\sim$ 260 K and $\sim$ 220 K, and at the same time the width of the distribution of free volume units decreases. This was linked [Bart97] to the dying out of the conformational-segmental dynamics. The results might be a reduced mobility of the thermalised but yet unbonded muon and consequently the delayed formation of the radicals. The disappearance of the signal might also be ascribed to an unstable muonium radical state with transitions between the diamagnetic and the paramagnetic state. This delay can be tested by means of time-delayed radio-frequency μSR measurements. Exploratory measurements by F. L. Pratt are consistent with this explanation, but further experiments are needed.

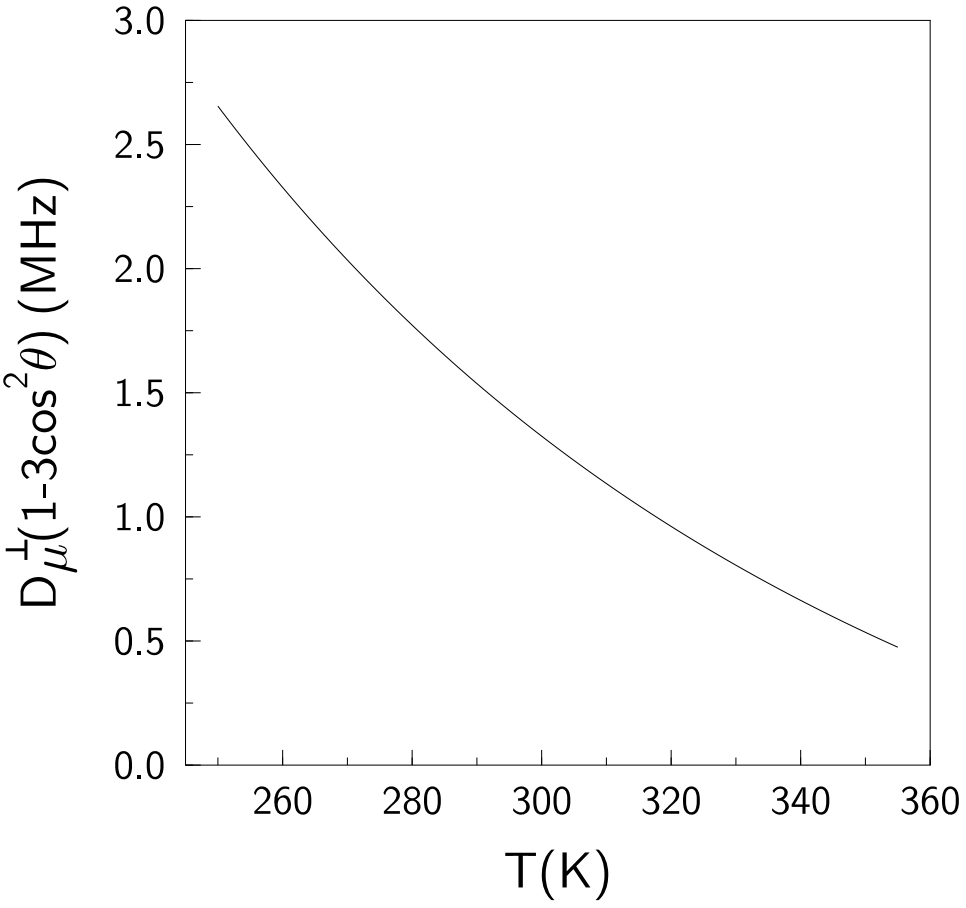

Figure 6.12: Temperature dependence of the anisotropy $D_\mu^\perp(1\text{-}3\cos^2\theta)$, see text.

6.5 Going through the glass transition: LF measurements in PB

Time differential LF experiments were performed at the RIKEN beamline of the ISIS facility. Measurements were performed at temperatures between 100 K and 300 K, and magnetic fields between 0.00 T and 0.38 T. It is noteworthy that in PB (and in glasses in general) the glass transition temperature depends on external parameters, such as the heating/cooling rate. A moderate temperature change rate of $\sim$ 1 K/min (value estimated from the ZF measurements) was applied (compare [Bähr93]) here in the vicinity of the glass transition.

The spectra obtained for the ZF and LF experiments could be fit with either a stretched exponential function (see 2.25) or to the Risch-Kehr (RK) function

[Risc92], an approximation to which is the expression

$$P_z(t) = (A_0 - A_b)\exp(\Gamma t)\,\mathrm{erfc}(\sqrt{\Gamma t}) + A_b \tag{6.16}$$

where erfc is the complementary error function and Γ is the RK relaxation parameter. A_b is the background amplitude and $(A_0 - A_b)$ is the relaxing amplitude. A stretched exponential function mirrors the spread of relaxation rates and is the equivalent of the "Kohlrausch" function. This functional form was successfully used in the analysis of many temperature dependent variations of dynamical variables (see section 6.2). On the other hand, the RK function [Risc92] is a model function for the muon depolarization for radical systems with electron spins mobile in one dimension, and it has been used before to model muon spectra in polymers [Prat97b, Prat97c, Jest97]. We have fitted the spectra with both functions. Fits by a stretched exponential with $\beta = 0.5$ (a root-exponential) give very good results. The quality of the RK fit was equally good. In the following I will present the results for the RK analysis. As was pointed out before (e.g. [Jest97]), for many practical applications the RK function and a stretched exponential will give equivalent results and the relaxation rate will follow the same trend. We have first fitted all the spectra with the root-exponential function. From these fits we obtained the initial asymmetry, which was fixed for the RK fit. A representative spectrum is depicted in Figure 6.13.

We could fit the dependence of the initial asymmetry with the function

$$P_z(B, t=0) = \frac{q/2 + (\gamma_e + \gamma_\mu)B/A_\mu}{1 + (\gamma_e + \gamma_\mu)B/A_\mu} \tag{6.17}$$

with

$$q = \frac{1/3 + (\gamma_e + \gamma_\mu)B/D_\mu^{\|}}{1 + (\gamma_e + \gamma_\mu)B/D_\mu^{\|}}\ . \tag{6.18}$$

This expression is an approximation to the repolarization one expects for a Hamiltonian with axial anisotropy [Prat97a]. It has been used to model the field dependent inital asymmetry in various polymers [Pratt93, Vall96]. Fits without an anisotropy $D_\mu^{\|}$ (see Equation 2.26) were not satisfactory for PB.

The fits to Equation 6.17 yield very good results, see Figure 6.14 . However, the extracted hyperfine interactions are higher than those obtained by the TF

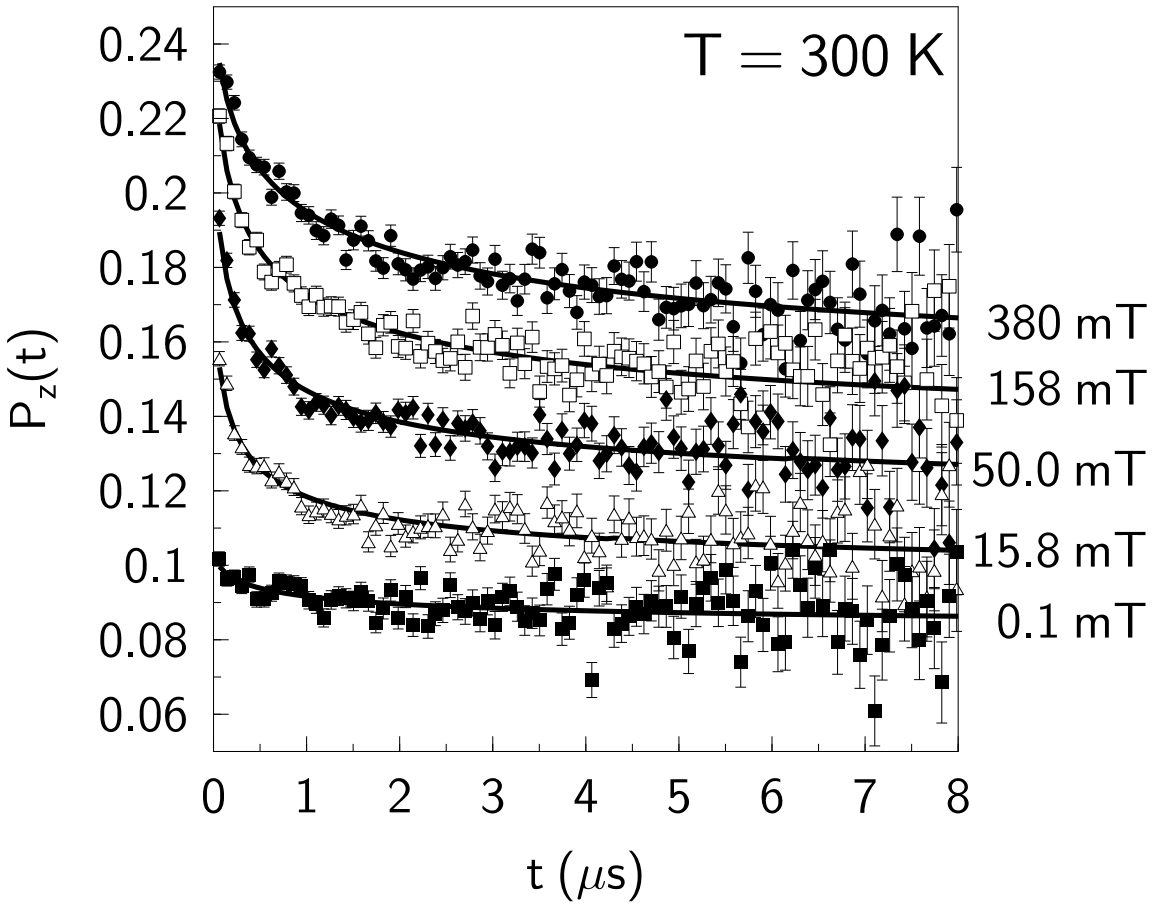

Figure 6.13: Raw data of μSR spectra at T = 300 K in the LF set up. Lines through the spectra are fits to the RK function, see Equation 6.16.

and ALC measurements. Equation 6.17 describes the repolarization for a static scenario, whereas we have seen that dynamics is important in our case. Therefore the values obtained for the fits should be considered only as an upper limit to the true values. The parameters are listed in Table 6.2. The repolarization shows the presence of the hyperfine interactions down to 100 K, whereas it is visible in the TF and the ALC signal only down to $T \sim 250\ K$. We can ascribe this discrepancy to the fact that repolarization measurements will be less susceptible to a spread in the hyperfine constants felt by the muon, whereas in TF measurements coherence of the muon spin rotation is necessary. This might indicate that the above interpretation of diamagnetic/paramagnetic cycles (or delayed radical formation) is valid. In a sufficiently large longitudinal magnetic field the diamagnetic/paramagnetic cycles should not influence the repolarization data of the

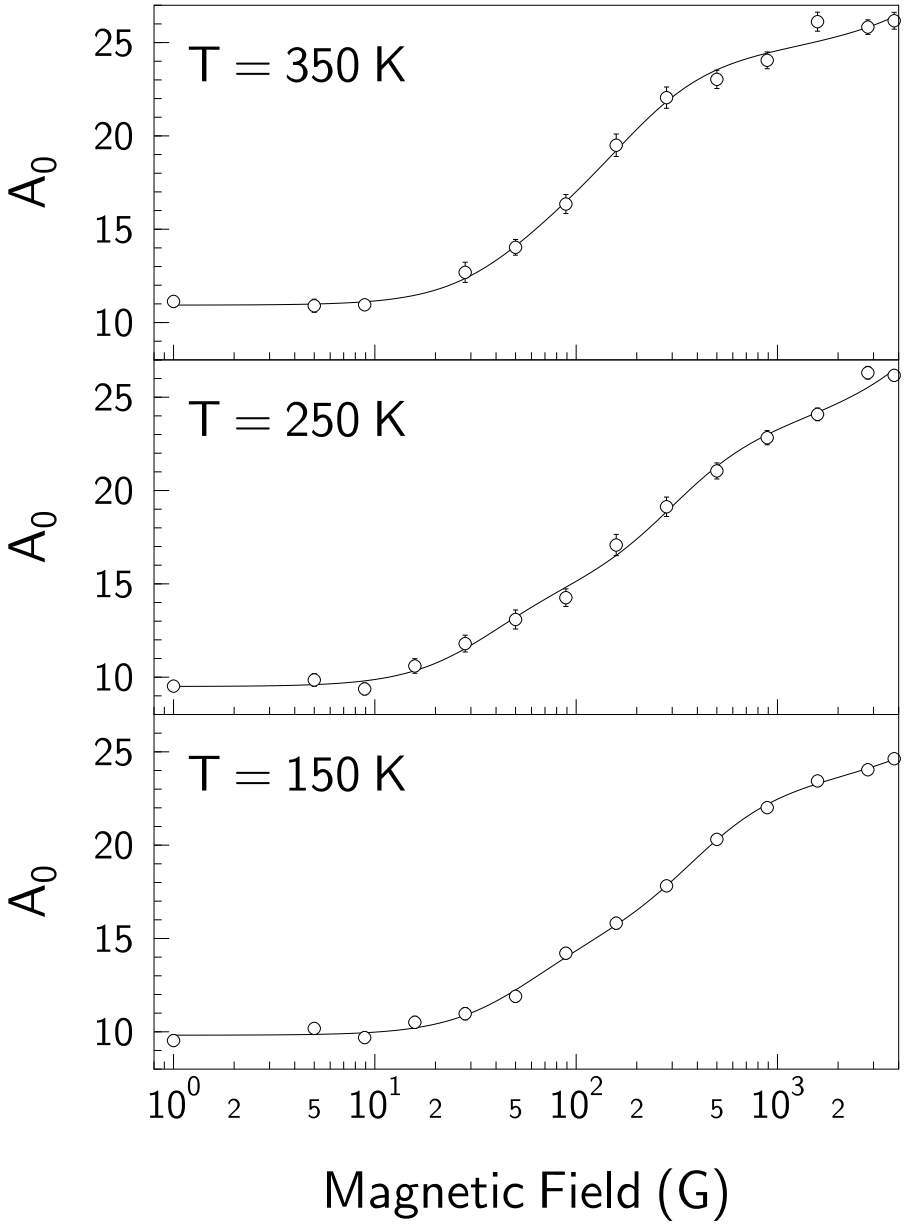

Figure 6.14: Repolarization curves for various temperatures in PB. The lines are fits to Equation 6.17.

	100 K	150 K	200 K	250 K
A_μ (LF)	647(95)	1072(88)	1326(180)	844(140)
A_μ (ALC/TF)	-	-	-	-
$\lvert D_\mu^{\parallel}\rvert$ (LF)	244(46)	166(14)	126(15)	108(18)
$\lvert D_\mu^{\parallel}(1-\cos^2\theta)\rvert$ (ALC/TF)	-	-	-	-

	275 K	300 K	325 K	350 K
A_μ (LF)	659(120)	527(100)	591(98)	525(87)
A_μ (ALC/TF)	305.7	299.6	294.3	289.4
$\lvert D_\mu^{\parallel}\rvert$ (LF)	88(20)	107(28)	153(30)	148(27)
$\lvert D_\mu^{\parallel}(1-\cos^2\theta)\rvert$ (ALC/TF)	3.8	2.7	1.8	0.9

Table 6.2: Hyperfine constants (in MHz) obtained from LF repolarization curves (see Figure 6.14) and from the ALC/TF measurements. The ALC/TF measurements are more precise, and the estimates from the repolarization curves should be taken as an upper limit.

initial asymmetry, since in both states the Zeeman states are the eigenstates of the system.

I now describe the general behaviour of the relaxation rate as a function of temperature and magnetic field. At low fields the relaxation rates seem to be rather scattered over intermediate values. At a typical field of 150 G we see a maximum in the relaxation rate, and for higher fields it falls off consistently, obeying a power law $\Gamma \propto B^{-n}$, where n varies with temperature, but is always close to 0.7. We can ascribe the low field relaxation to random coupling to nuclei. For intermediate fields the interaction with the nuclear spins will be decoupled, and the muon relaxation is dominated by other effects such as the electron spin relaxation and possible temporal variations of the hyperfine interaction due to changes in distances etc. To investigate this effect in more detail, we now follow the temperature variation of the relaxation rate at a fixed magnetic field of 0.3 T. At this field strength, coupling to surrounding nuclei should be suppressed and changes between paramagnetic and diamagnetic states should not lead to enhanced relaxation (see above).

This temperature dependence is shown in Figure 6.15. For decreasing temperature the relaxation decreases, until just below the glass transition temperature T_g. Here there is a drastic change in the temperature dependence and it remains

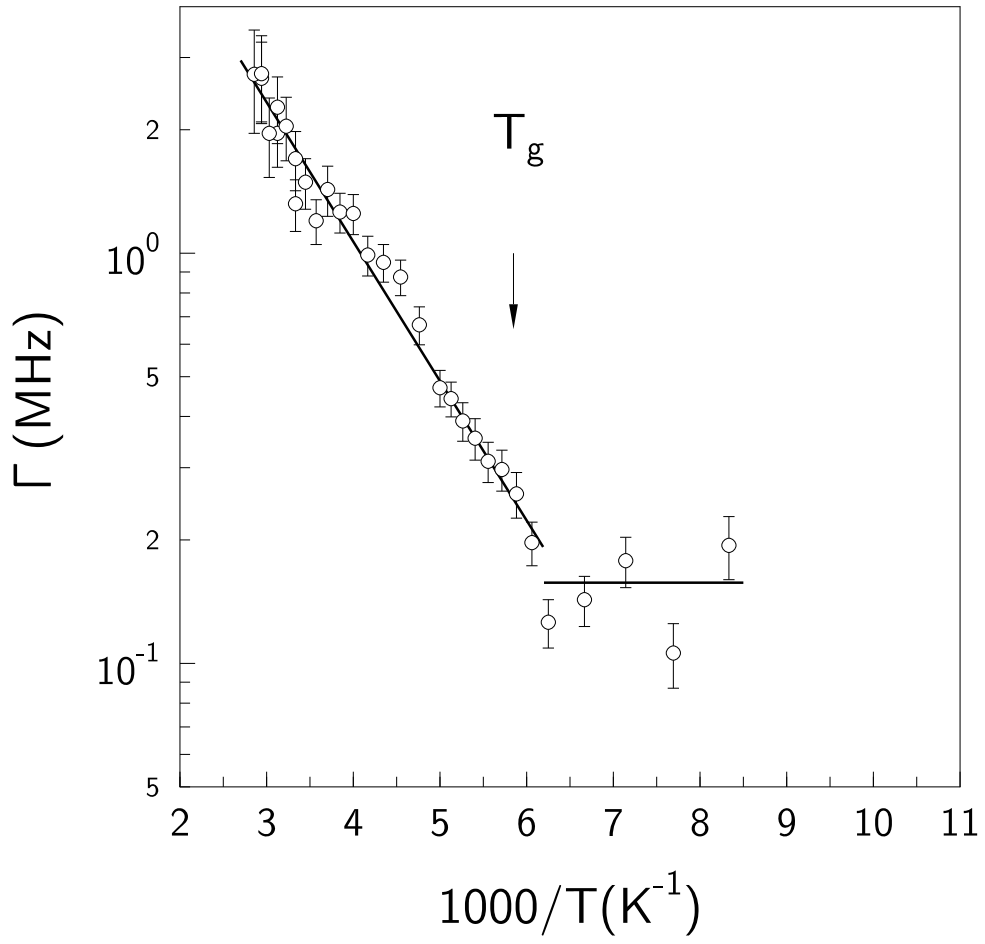

Figure 6.15: LF relaxation rate data for PB at B = 0.3 T. Note that the y-axis is on a logarithmic scale. The data is well fitted by an Arrhenius law above T_g. Below the glass transition the relaxation remains constant.

constant. Clearly, the behaviour of the relaxation can be linked to the glass transition. In view of what was said above, this behaviour is consistent with an (indirect) coupling of the muon spin to the conformal changes along the polymer chain that take place above T_g but freeze out in the glass state. Also shown in Figure 6.15 is a fit of the relaxation parameter to an Arrhenius law.

We can fit the temperature dependence of the relaxation rate to the Williams-Landel-Ferry (WLF) law, which was originally used to describe viscoelastic relaxation and was first derived from the free volume theory [Cohe59]. We adopt the

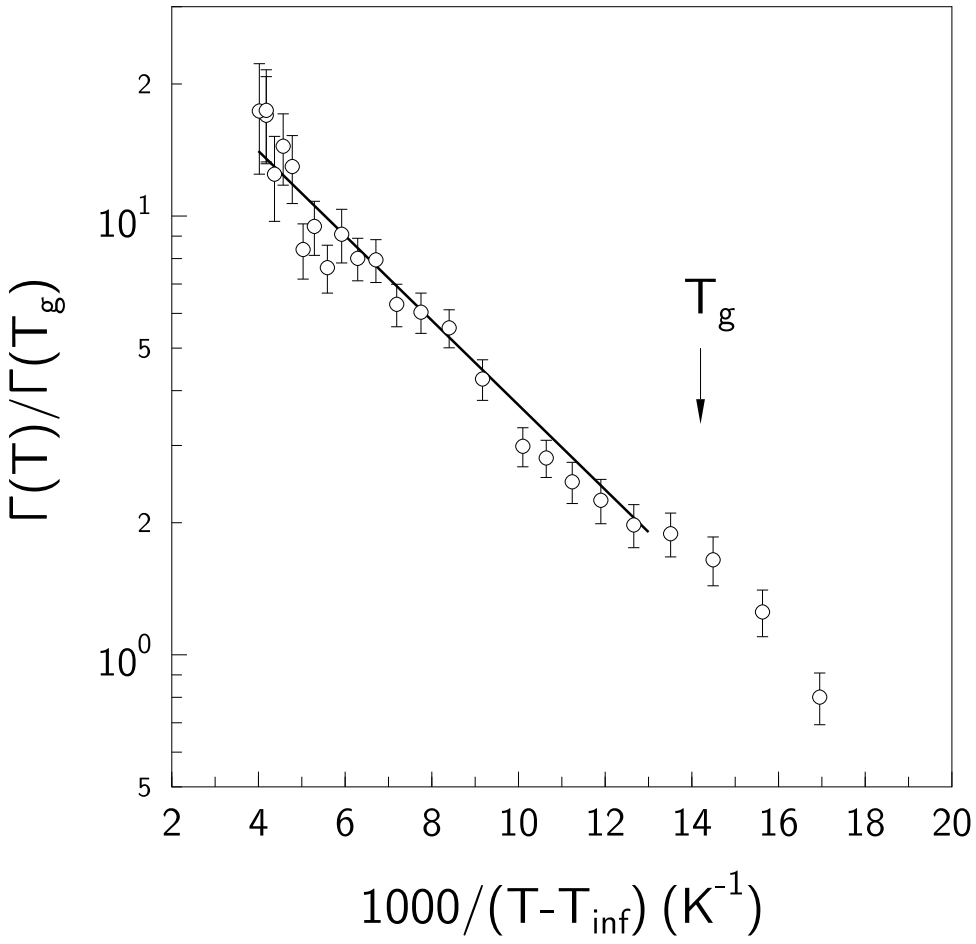

Figure 6.16: WLF fit (see Equation 6.19) to data for PB at B = 0.3 T. The y-axis is on a logarithmic scale. The data is well fitted by the WLF law.

expression given in [Deje89] and arrive at

$$\ln\left\{\frac{\Gamma(T)}{\Gamma(T_g)}\right\} = C_1 - \frac{C_1 C_2}{T - (T_g - C_2)} \tag{6.19}$$

where C_1 and C_2 are parameters characteristic of a particular polymer. We obtain $C_1 = 3.532(72)$ and $C_2 = 62.9(26)$ K. The value of C_2 is very close to that obtained from other measurements [Ferr80], $C_2 = 59.6$ K, see also [Deje89]. This might underline, as pointed out before (e.g. in [Ye97]), that C_2 is an inherent parameter of the glass transition of a specific material. On the other hand, the value obtained for C_1 (or C_1C_2) is smaller by a factor of 3.21 than values found in the literature. This might indicate that the relaxation mechanism of the muon spin is not fully coupled to the motion of PB on the macroscopic scale. Viscosity

measurements involve the measurement of large scale motions and the breaking of bonds between molecules. μSR on the other hand should be susceptible to smaller scale motions, and the corresponding activation energy should be smaller, as seen here. This, however, is a speculative suggestion, and comparing the two fits by an Arrhenius law (Figure 6.15) and by a WLF expression (Figure 6.16) does not give a conclusive answer. Measurements on other glass formers might help to promote the understanding of the trends seen here.

The results obtained here may be compared to μSR measurements on conducting polymers like trans-polyacetylene (PA) and polyaniline (PANI) [Ishi85, Prat97b, Prat97c, Prat99]. In these systems the *mobile* electron diffuses along the polymer chain, and the diffusion constant can be estimated by μSR experiments under certain assumptions. As the electron diffuses, electron spin flips can occur due to spin-lattice relaxation and interaction with magnetic impurities. When the electron is close to the muon the hyperfine interaction will be non-negligible, while it is small for the case when the electron has diffused far away. For diffusional motion the probability of return of the electron to the muon is non-zero. The resulting time-varying hyperfine interaction gives rise to muon-spin relaxation and allows estimates of the temperature dependent diffusion constant to be made [Risc92].

The general behaviour of the relaxation rates in these experiments looks similar to the behaviour in PB. For increasing applied magnetic fields the relaxation decreases, and as the temperature is lowered the relaxation rate Γ at a fixed magnetic field decreases and eventually remains constant at low temperatures. The functional expressions which are applied to describe the behaviour of the relaxation rates with temperature are similar for PB and PANI. However, it appears that the relaxation rate in the conducting polymers is much smaller than that seen in PB. For example, at 300 K in an applied field of 1 kG the relaxation rate in PANI is ~ 4.15 kHz whereas in PB it is ~ 1.8 MHz (see Figure 6.15).

PANI and PB are two limiting cases: PANI exhibits considerable electron diffusion [Prat97b, Prat97c, Prat99] whereas in PB the radical electron is localized. In intermediate cases, where the electron diffuses, but stays in the vicinity of the muon long enough to allow motional processes to influence the muon spin relaxation, it might be difficult to disentangle these two effects.

6.6 Concluding remarks

In this chapter I have presented work on polybutadiene, a glass forming polymer. We have seen how the simple structure of PB leads to the occurrence of only one hyperfine constant. The presence of the $\Delta M = 1$ resonance in the ALC spectrum is proof that there is some non-zero anisotropy in the hyperfine interaction in this system. Possible future experiments could include measurements at higher temperatures to confirm or contradict the conjecture of an averaging out of the anisotropy with motional speeding up. The vanishing of both resonances (and also of the TF signal) at lower temperatures was ascribed to a delayed formation of the radical state or interchanging diamagnetic/paramagnetic states. Time-delayed RF measurements should be able to shed light on this conjecture.

The LF experiments, performed above and below the glass transition of PB, have shown a behaviour of the muon spin relaxation consistent with other measurements, including macroscopic experiments. The microscopic mechanism of the depolarization was related to segmental motion of the polymers. It will be interesting to perform further experiments on other glass formers to explore whether this is a trend that is universal.

Appendix A

Calculations

Contents

A.1 Time-dependent muon polarization of muonium

To arrive at Equation 2.9

$$P_z(t) = \frac{1 + 2(B/B_0)^2}{2\{1 + (B/B_0)^2\}} + \frac{1}{2\{1 + (B/B_0)^2\}} \cos(\omega_{24} t) \tag{A.1}$$

we start by defining the spin operators $\sigma_i = 2S_i/\hbar$, where $i = x, y, z$ and S_i is the i-th Cartesian component of the muon spin-operator S_μ. The state vector $|\Psi(t)\rangle$ at a time t can be written as an composition of the eigenstates of Table 2.4, including time evolution:

$$|\Psi(t)\rangle = \sum_{j=1}^{4} c_j e^{-\imath E_i t/\hbar} |\Psi_i\rangle \ , \tag{A.2}$$

where $\imath^2 = -1$. The polarization $\mathbf{P}(t)$ at time t is given by the expectation value of the Cartesian components,

$$P_i(t) = \langle\Psi(t)| \sigma_i |\Psi(t)\rangle = \sum_{j,k=1}^{4} c_k^* c_j e^{-\imath\omega_{jk} t} \langle\Psi_k| \sigma_i |\Psi_j\rangle \ , \tag{A.3}$$

where $\omega_{jk} = (E_j - E_k)/\hbar$. We get

$$P_z(t) = \sum_{j,k=1}^{4} c_k^* c_j e^{-\imath\omega_{jk} t} \langle\Psi_k| \sigma_z |\Psi_j\rangle \tag{A.4}$$

Recall that $\sigma_z \{|\uparrow_\mu\rangle \otimes |\chi_e\rangle\} = |\uparrow_\mu\rangle \otimes |\chi_e\rangle$ and $\sigma_z \{|\downarrow_\mu\rangle \otimes |\chi_e\rangle\} = -|\downarrow_\mu\rangle \otimes |\chi_e\rangle$. The four constants c_j, $j = 1, 2, 3, 4$, are given by the initial condition of the muon polarization,

$$\mathbf{P}(t = 0) = (0, 0, 1) \ . \tag{A.5}$$

A now straightforward calculation finally yields Equation A.1.

Bibliography

Chapter 1

[Aege97] C. M. Aegerter and S. L. Lee, *Appl. Magn. Reson.* **13**, 75 (1997)

[Bewl99] R. Bewley, S. J. Blundell, B. W. Lovett, Th. Jestädt, F. L. Pratt, K. H. Chow, W. Hayes, P. D. Battle, M. A. Green, J. E. Millburn, M. J. Rosseinsky, L. E. Spring and J. F. Vente, submitted to *Phys. Rev. B*

[Blun99] S. J. Blundell, *Contemp. Phys.*, in press

[Cox87] S. F. J. Cox, *J. Phys. C* **20**, 3187 (1987)

[Garw57] R. L. Garwin, L. M. Lederman and M. Weinrich, *Phys. Rev.* **105**, 1415 (1957)

[Jest98] Th. Jestädt, R. I. Bewley, S. J. Blundell, W. Hayes, B. W. Lovett, F. L. Pratt and R. C. C. Ward, *J. Phys.: Condens. Matter* **10**, L259 (1998)

[Jest99] Th. Jestädt, K. H. Chow, S. J. Blundell, W. Hayes, F. L. Pratt, B. W. Lovett, M. A. Green, J. E. Millburn and M. J. Rosseinsky, *Phys. Rev. B* **59**, 3775 (1999)

[Patt88] B. D. Patterson, *Rev. Mod. Phys.* **60**, 69 (1988)

[Prat98] Francis L. Pratt, *WiMDA* (Windows Muon Data Analysis) program, version 1.00 – 1.54, ©1998

[Rodu93] E. Roduner, *Chem. Soc. Rev.* **32**, 337 (1993)

[Sche85] A. Schenck, *Muon Spin Rotation Spectroscopy*, Bristol (1985)

[Sche95] A. Schenck and F. N. Gygax, *Magnetic Materials Studied by Muon Spin Rotation Spectroscopy*, in: K. H. J. Buschow (ed.): *Handbook of Magnetic Materials* **9**, Amsterdam (1995)

[Uemu88] Y. J. Uemura, V. J. Emery, A. R. Moodenbaugh, M. Suenaga, D. C. Johnston, A. J. Jacobson, J. T. Lewandowski, J. H. Brewer, R. F. Kiefl, S. R. Kreitzmann, G. M. Luke, T. Riseman, C. E. Stronach, W. J. Kossler, J. R. Kempton, X. H. Yu, D. Opie and H. E. Schone,

Phys. Rev. B **38**, 909 (1988)

Chapter 2

[Chap84] J. Chappert, *Principles of the μSR Technique*, in: J. Chappert and R. I. Grynszpan (eds.): *Muons and Pions in Materials Research*, Amsterdam (1987)

[Cox87] S. F. J. Cox, *J. Phys. C* **20**, 3187 (1987)

[deRe97] P D. Reotier and A. Yaouanc, *J. Phys.: Condens. Matter* **9**, 9113 (1997)

[Eato98] G. H. Eaton, Technical Report RAL-TR-1998-019, Council for the Central Laboratory of the Research Councils, April 1998

[Haya79] R. S. Hayano, Y. J. Uemura, J. Imazato, N. Nishida, T. Yamazaki and R. Kubo, *Phys. Rev. B* **20**, 850 (1979)

[Prat93] F. L. Pratt, W. Hayes, G. R. Mitchell, B. Rossi, M. S. Kiani, B. D. Malhotra, S. S. Pandey, A. Milton and A. P. Monkman, *Synth. Met.* **55**, 677 (1993)

[Prat97a] F. L. Pratt, *Phil. Mag.* **75**, 371 (1997)

[Part96] Review of Particle Physics, *Phys. Rev. D* **54** (1996)

[Sche85] A. Schenck, *Muon Spin Rotation Spectroscopy*, Bristol (1985)

[Sche95] A. Schenck and F. N. Gygax, *Magnetic Materials Studied by Muon Spin Rotation Spectroscopy*, in: K. H. J. Buschow (ed.): *Handbook of Magnetic Materials* **9**, Amsterdam (1995)

[Smil94] V. P. Smilga and Yu. M. Belousov, *The Muon Method in Science*, New York (1994)

[Uemu85] Y. J. Uemura, T. Yamazaki, D. R. Harshman, M. Senba and E.J. Ansaldo, *Phys. Rev. B* **31**, 546 (1985)

[User94] PSI data: *User's Guide*, H. C. Walter (head of editorial committe), Paul Scherrer Institut, Villigen, CH, 2nd edition (1994); additional data: Alex Amato (PSI), private communucation (GPS), Ivan Reid (PSI), private communication (GPD); MuSR and EMU data: Philip King (ISIS), private communication; RIKEN data: Francis Pratt (RIKEN), private communication

Chapter 3

[Aepp88] G. Aeppli and D. J. Buttrey, *Phys. Rev. Lett.* **61**, 203 (1988)

[Bedn86] J. G. Bednorz and K. A. Müller, *Z. Phys. B* **64**, 189 (1986)

[Boek86] C. Boekema, R. L. Lichti, K. C. B. Chan, V. A. M. Brabers, A. B. Denison, D. W. Cooke, R. H. Heffner, R. L. Hutson and M. E. Schillaci, *Phys. Rev. B* **33**, 210 (1986)

[Bors95] F. Borsa, P. Carretta, J. H. Cho, F. C. Chou, Q. Hu, D. C. Johnston, A. Lascialfari, D. R. Torgenson, R. J. Gooding, N. M. Salem and K. J. E. Vos, *Phys. Rev. B* **52**, 7334 (1995)

[Cava91] R. J. Cava, B. Batlogg, T. T. Palstra, J. J. Krajewski, W. F. Peck, A. P. Ramirez and L. W. Rupp, *Phys. Rev. B* **43**, 1229 (1991) and references therein.

[Bram93] S. T. Bramwell and P.C.W. Holdsworth, *J. Phys.: Condens. Matter* **5**, L53 (1993)

[Chen93] C. H. Chen, S-W. Cheong and A. S. Cooper, *Phys. Rev. Lett.* **71**, 2461 (1993)

[Cheo91] S.-W. Cheong, G. Aeppli, T. E. Mason, H. Mook, S. M. Hayden, P. C. Canfield, Z. Fisk, K. N. Clausen and J. L. Martinez, *Phys. Rev. Lett.* **67**, 1791 (1991)

[Cheo94] S-W. Cheong, H. Y. Hwang, C. H. Chen, B. Batlogg, L. W. Rupp, Jr., and S. A. Carter, *Phys. Rev. B* **49**, 7088 (1994)

[Chow96a] K. H. Chow, P. A. Pattenden, S. J. Blundell, W. Hayes, F. L. Pratt, Th. Jestädt, M. A. Green, J. E. Millburn, M. J. Rosseinsky, B. Hitti, S. R. Dunsiger, R. F. Kiefl, C. Chen and A. J. S. Chowdhury, *Phys. Rev. B* **53**, R14725 (1996)

[Chow96b] K. H. Chow, Th. Jestädt, S. J. Blundell, S. R. Dunsiger, W. Hayes, B. Hitti, M. A. Green, R. F. Kiefl, J. E. Millburn, P. A. Pattenden, F. L. Pratt and M. J. Rosseinsky, *Hyp. Int.* **104**, 55 (1997)

[CRC95] *CRC Handbook of Chemistry and Physics, 76th edition* (Ed.: D. R. Lide), CRC Press, Boca Raton (1995)

[Dago94] E. Dagotto, *Rev. Mod. Phys.* **66**, 763 (1994)

[Daws90] W. K. Dawson *et al.*, *Hyp. Int.* **63**, 219 (1990)

[deJo74] L. J. de Jongh and A. R. Miedema, *Adv. Phys.* **23**, 1 (1974)

[Frel91] T. Freltoft, D. J. Buttrey, G. Aeppli, D. Vaknin and G. Shirane, *Phys. Rev. B* , **44**, 5046 (1991)

[Furu96] Y. Furukawa and S. Wada, *J. Phys.: Condens. Matter* **6**, 852 (1996)

[Gopa92] P. Gopalan, M. W. McElfresh, Z. Kakol, J. Spalek and J. M. Honig, *Phys. Rev. B* **45**, 249 (1992)

[Hars88] D. R. Harshman, G. Aeppli, G. P. Espinosa, A. S. Cooper, J. P. Remeika, E. J. Ansaldo, T. M. Riseman, D. L. Williams, D. R. Noakes, B. Ellman and T. F. Rosenbaum, *Phys. Rev. B* **38**, 852 (1988)

[Hayd92] S. M. Hayden, G. H. Lander, J. Zarestky, P. J. Brown, C. Stassis, P. Metcalf and J. M. Honig, *Phys. Rev. Lett.* **68**, 1061 (1992)

[Hean98] P. J. Heaney, A. Mehta, G. Sarosi, V. E. Lamberti and A. Navrotsky, *Phys. Rev. B* **57**, 10370 (1998)

[Holz81] E. Holzschuh *et al.*, *Hyp. Int.* **8**, 615 (1981)

[Jest99] Th. Jestädt, K. H. Chow, S. J. Blundell, W. Hayes, F. L. Pratt, B. W. Lovett, M. A. Green, J. E. Millburn and M. J. Rosseinsky, *Phys. Rev. B* **59**, 3775 (1999)

[Kere94] A. Keren, *Phys. Rev. B* **50**, 10039 (1994)

[Land91] G. H. Lander, P. J. Brown, C. Stassis, P. Gopalan, J. Spalek and G. Honig, *Phys. Rev. B* **43**, 448 (1991)

[Le90] L. P. Le, G. M. Luke, B. J. Sternlieb, Y. J. Uemura, J. H. Brewer, T. M. Riseman, D. C. Johnston, L. L. Miller, Y. Hidaka and H. Murakami, *Hyp. Int.* **63**, 279 (1990)

[Lee97] S.-H. Lee and S.-W. Cheong, *Phys. Rev. Lett.* **79**, 2514 (1997)

[Ma76] Sheng-Keng Ma, *Modern Theory of Critical Phenomena* (Benjamin, New York, 1976)

[Mart92] B. Martínez, X. Obradors, E. J. Ansaldo, C. Niedermayer, D. R. Noakes, M. J. Sayagués, M. Vallet and J. González-Calbet, *J. Mag. Magn. Mat.* **104-107**, 941 (1992)

[Naka97] K. Nakajima, Y. Endoh, S. Hosoya, J. Wada, D. Welz, H. M. Mayer, H. A. Graf and M. Steiner, *J. Phys. Soc. Japan* **66**, 809 (1997)

[Nish90] N. Nishida *et al.*, *Hyp. Int.* **63**, 183 (1990)

[Sach95] V. Sachan, D. J. Buttrey, J. M. Tranquada, J. E. Lorenzo and G. Shirane *Phys. Rev. B* **51**, 12742 (1995)

[Stra91] Th. Strangfeld, K. Westerholt and H. Bach, *Physica C* **183**, 1 (1991)

[Tavi91] G. Tavizón, E. Orgaz and R. Escudero, *Physica C* , **185-189**, 517 (1991)

[Thur89] T. R. Thurston, R. J. Birgeneau, M. A. Kastner, N. W. Preyer, G. Shirane, Y. Fujii, K. Yamada, Y. Endoh, K. Kaurai, M. Matsuda, Y. Hidaka and T. Murakami, *Phys. Rev. B* **40**, 4585 (1989)

[Tran93] J. M. Tranquada, D. J. Buttrey and D. E. Rice, *Phys. Rev. Lett.* **70**, 445 (1993)

[Tran94a] J. M. Tranquada, J. E. Lorenzo, D. J. Buttrey and V. Sachan, *Phys. Rev. Lett.* **73**, 1003 (1994)

[Tran94b] J. M. Tranquada, Y. Kong, J. E. Lorenzo, D. J. Buttrey, D. E. Rice and V. Sachan, Phys. Rev. B **50**, 6340 (1994)

[Tran95a] J. M. Tranquada, J. E. Lorenzo, D. J. Buttrey and V. Sachan, *Phys. Rev. B* **52**, 3581 (1995)

[Tran95b] J. M. Tranquada, B. J. Sternlieb, J. D. Axe, Y. Nakamura and S. Uchida, *Nature* **35**, 561 (1995)

[Tran96] J. M. Tranquada, D. J. Buttrey and V. Sachan, *Phys. Rev. B* **54**, 12318 (1996)

[Tran97a] J. M. Tranquada, P. Wochner, A. R. Moodenbaugh and D. J. Buttrey, *Phys. Rev. B* **55**, R6113 (1997)

[Tran97b] J. M. Tranquada, P. Wochner and D. J. Buttrey, *Phys. Rev. Lett.* **79**, 2133 (1997)

[Uemu85] Y. J. Uemura, T. Yamazaki, D. R. Harshman, M. Senba and E. J. Ansaldo, *Phys. Rev. B* **31**, 546 (1985)

[Webe90] M. Weber *et al.*, *Hyp. Int.* **63**, 207 (1990)

[Yama94] K. Yamada, T. Omata, K. Nakajima and Y. Endoh, *Physica C* **221**, 335 (1994)

Chapter 4

[Ande55] P. W. Anderson, *Phys. Rev.* **100**, 675 (1955)

[Batt96a] P. D. Battle, S. J. Blundell, M. A. Green, W. Hayes, M. Honold, A. K. Klehe, N. S. Laskey, J. E. Millburn, L. Murphy, M. J. Rosseinsky, N. A. Samarin, J. Singleton, N. E. Sluchanko, S. P. Sullivan and J. F. Vente, *J. Phys.: Condens. Matter* **8**, L427 (1996)

[Batt96b] P. D. Battle, M. A. Green, N. S. Laskey, J. E. Millburn, P. G. Radaelli, M. J. Rosseinsky, S. P. Sullivan and J. F. Vente, *Phys. Rev. B* **54**, 15967 (1996)

[Batt97a] P. D. Battle, M. A. Green, N. S. Laskey, N. Kasmir, J. E. Millburn, L. E. Spring, S. P. Sullivan, M. J. Rosseinsky and J. F. Vente, *J. Mater. Chem.* **7**, 977 (1997)

[Batt97b] P. D. Battle, M. A. Green, N. S. Laskey, J. E. Millburn, L. Murphy, M. J. Rosseinsky, S. P. Sullivan and J. F. Vente, *Chem. Mater.* **9**, 552 (1997)

[Batt97c] P. D. Battle, J. E. Millburn, M. J. Rosseinsky, L. E. Spring and J. F. Vente, *Chem. Mater.* **9**, 3136 (1997)

[Bewl99] R. Bewley, S. J. Blundell, B. W. Lovett, Th. Jestädt, F. L. Pratt, K. H. Chow, W. Hayes, P. D. Battle, M. A. Green, J. E. Millburn, M. J. Rosseinsky, L. E. Spring and J. F. Vente, submitted to *Phys. Rev. B*

[Camp94] I. A. Campbell, A. Schenck, D. Herlach, F. N. Gygax, A. Amato, R. Cywinski and S. H. Kilcoyne, *Phys. Rev. Lett.* **72**, 1291 (1994)

[CRC95] *CRC Handbook of Chemistry and Physics, 76th edition* (Ed.: D. R. Lide), CRC Press, Boca Raton (1995)

[deGe60] P. G. deGennes, *Phys. Rev.* **118**, 141 (1960)

[Heff96] R. H. Heffner, L. P. Le, M. F. Hundley, J. J. Neumeier, G. M. Luke, K. Kojima, B. Nachumi, Y. J. Uemura, D. E. MacLaughlin and S.-W. Cheong, *Phys. Rev. Lett.* **77**, 1869 (1996)

[Heff97] R. H. Heffner, L. P. Le, D. E. MacLaughlin, G. M. Luke, K. Kojima, B. Nachumi, Y. J. Uemura, G. J. Nieuwenhuys and S.-W. Cheong, *Physica B* **230-232**, 759 (1997)

[Heff98] R. H. Heffner, D. E. MacLaughlin, G. J. Nieuwenhuys, T. Kimura, G. M. Luke, Y. Tokura and Y. J. Uemura, *Phys. Rev. Lett.* **81** 1706 (1998)

[Helm93] R. von Helmholt, J. Wecker, B. Holzapfel, L. Schultz and K. Samwer, *Phys. Rev. Lett.* **71**, 2331 (1993)

[Kust89] R. M. Kusters, J. Singleton, D. A. Keen, R. McGreevy, and W. Hayes, *Physica B* **155**, 362 (1989)

[Le90] L. P. Le, G. M. Luke, B. J. Sternlieb, Y. J. Uemura, J. H. Brewer, T. M. Riseman, D. C. Johnston, L. L. Miller, Y. Hidaka and H. Murakami, *Hyp. Int.* **63**, 279 (1990)

[Maig95] A. Maignan, C. Simon, V. Caignaert and B. Raveau, *Sol. Stat. Commun.* **96**, 623 (1995)

[Mill95] A. J. Millis, P. B. Littlewood and B. I. Shraiman, *Phys. Rev. Lett.* **74**, 5144 (1995)

[Mill96] A. J. Millis, B. I. Shraiman and R. Mueller, *Phys. Rev. Lett.* **77**, 175 (1996)

[Mori96] Y. Moritomo, A. Asamitsu, H. Kuwahara and Y. Tokura, *Nature* **380**, 141 (1996)

[Nach98] B. Nachumi, Y. Fudamoto, A. Keren, K. M. Kojima, M. Larkin, N. Ichikawa, M. Goto, H. Takagi, S. Uchida, M. K. Crawford, E. M. McCarron, D. E. MacLaughlin and R. H. Heffner, *Phys. Rev. B* **58**, 8760 (1998)

[Ogie85] A. T. Ogielski, *Phys. Rev. B* **32**, 7384 (1985)

[Rami97] A. P. Ramirez, *J. Phys.: Condens. Matter* **9**, 8171 (1997)

[Röde96] H. Röder, J. Zang and A. R. Bishop, *Phys. Rev. Lett.* **76**, 1356 (1996)

[Sesh96] R. Seshardi, C. Martin, A. Maignan, M. Hervieu, B. Raveau and C. N. R. Rao, *J. Mater. Chem.* **6**, 1585 (1996)

[Shen97] L. Sheng, D. Y. Xing, D. N. Sheng and C. S. Ting, *Phys. Rev. Lett.* **79**, 1710 (1997)

[Rudd58] S. N. Ruddlesden and P. Popper, *Acta Cryst.* **11**, 541 (1958)

[Shan76] R. D. Shannon, *Acta Cryst. A* **32**, 751 (1976)

[Tere97] J. M. De Teresa, C. Ritter, M. R. Ibarra, P. A. Algarabel, J. L. García-Muñoz, J. Blasco, J. García and C. Marquina, *Phys. Rev. B* **56**, 3317 (1997)

[Uemu85] Y. J. Uemura, T. Yamazaki, D. R. Harshman, M. Senba and E.J. Ansaldo, *Phys. Rev. B* **31**, 546 (1985)

[Zene51] C. Zener, *Phys. Rev.* **82**, 403 (1951)

Chapter 5

[Albr96a] M. Albrecht and F. Mila, *Phys. Rev. B* **53**, R2945 (1996)

[Albr96b] M. Albrecht, F. Mila and D. Poilblanc, *Phys. Rev. B* **54**, 15856 (1996)

[Azum94] M. Azuma, Z. Hiroi, H. Takano, K. Ishida and Y. Kitaoka, *Phys. Rev. Lett.* **73**, 3463 (1994);

[Barn94] T. Barnes and J. Riera, *Phys. Rev. B* **50**, 6817 (1994);

[Blun97] S. J. Blundell, F. L. Pratt, P. A. Pattenden, M. Kurmoo, K. H. Chow, S. Takagi, Th. Jestädt and W. Hayes, *J. Phys.: Condens. Matter* **9**, L119 (1997)

[Bose97] I. Bose and A. Ghosh, *Phys. Rev. B* **56**, 3149 (1997)

[Boul73] J. C. Bouloux and J. Galy, *Acta Cryst. B* **29**, 1335 (1973)

[Bray75] J. W. Bray, H. R. Hart, L. V. Interrante, I. S. Jacobs, J. S. Kasper, G. D. Watkins, S. H. Wee and J. C. Bonner, *Phys. Rev. Lett.* **35**, 744 (1975)

[Bray83] J. W. Bray, L. W. Interrante, I. S. Jacobs and J. C. Bonner, *Extended Linear Chain Compounds*, Vol. 3, p. 353, New Tork, 1983

[CRC95] *CRC Handbook of Chemistry and Physics, 76th edition* (Ed.: D. R. Lide), CRC Press, Boca Raton (1995)

[Dago95] E. Dagotto and T. M. Rice, *Science* **271**, 619 (1995)

[Eccl94] R. S. Eccleston, T. Barnes, J. Brody and J. W. Johnson, *Phys. Rev. Lett.* **73**, 2626 (1994);

[Fuko97] Y. Fukomoto, *J. Phys. Soc. Japan* **66**, 2178 (1997)

[Fuko98] Y. Fukomoto and A. Oguchi, *J. Phys. Soc. Japan* **67**, 2205 (1998)

[Garc95] J. L. García-Muñoz, M. Suaadi and B. Martínez, *Phys. Rev. B* **52**, 4288 (1995)

[Gelf96] M. P. Gelfand, Z. Weihong, R. R. P. Singh, J. Oitmaa and C. J. Hamer, *Phys. Rev. Lett.* **77**, 2794 (1996)

[Haya79] R. S. Hayano, Y. J. Uemura, J. Imazato, N. Nishida, T. Tamazaki and R. Kubo, *Phys. Rev. B* **20**, 850 (1979)

[Ishi94] K. Ishida, Y. Kitaoka, K. Asayama, M. Azuma, Z. Hiroi and M. Takano, *J. Phys. Soc. Japan* **63**, 3222 (1994);

[Itoh95] M. Itoh, S. Hirashima and K. Motoya, *Phys. Rev. B* **52**, 3410 (1995)

[Ivan97] N. B. Ivanov and J. Richter, *Phys. Lett. A* **232**, 308 (1997)

[Jest98] Th. Jestädt, R. I. Bewley, S. J. Blundell, W. Hayes, B. W. Lovett, F. L. Pratt and R. C. C. Ward, *J. Phys.: Condens. Matter* **10**, L259 (1998)

[Kato95] N. Katoh and M. Imada, *J. Phys. Soc. Japan* **64**, 4105 (1995)

[Koda96] K. Kodama, H. Harashina, S. Shamoto, S. Taniguchi, M. Sato, K. Kakurai and M. Nishi, *J. Phys. Soc. Japan* **65**, 1941 (1996)

[Koda97] K. Kodama, H. Harashina, H. Sasaku, Y. Kobayashi, M. Kasai, S. Taniguchi, Y. Yasui, M. Sato, K. Kakurai, T. Mori and M. Nishi, *J. Phys. Soc. Japan* **66**, 793 (1997)

[Koji97] K. M. Kojima, *Appl. Mag. Res.* **13**, 111 (1997)

[Mesh96] S. V. Meshkov and D. Foerster, *J. Phys.: Condens. Matter* **8**, 7917 (1996)

[Miya96] T. Miyazaki and D. Yoshioka, *J. Phys. Soc. Japan* **65**, 2370 (1996)

[Oham97] T. Ohama, H. Yasuoka, M. Isobe and Y. Ueda, *J. Phys. Soc. Japan* **66**, 23 (1997)

[Pick97] W. E. Pickett, *Phys. Rev. Lett.* **79**, 1746 (1997)

[Sach96] S. Sachdev and N. Read, *Phys. Rev. Lett.* **77**, 4800 (1996)

[Sano96] K. Sano and K. Takano, *J. Phys. Soc. Japan* **65**, 46 (1996)

[Smit76] L. S. Smith, E. Ehrenfreund, A. J. Heeger, L. V. Interrante, J. W. Bray, J. R. Hart Jr. and I. S. Jacobs, *Sol. Stat. Commun.* **19**, 377 (1976)

[Star96] O. A. Starykh, M. E. Zhutomirsky, D. I. Khomskii, R. R. P. Singgh and K. Ueda, *Phys. Rev. Lett.* **77**, 2558 (1996)

[Tani95] S. Taniguchi, N. Takashi, Y. Yasui, Y. Kobayashi, M. Sato, T. Nishioka, M. Kontani and K. Sano, *J. Phys. Soc. Japan* **64**, 2758 (1995)

[Troy96] M. Troyer, H. Kontani and K. Ueda, *Phys. Rev. Lett.* **76**, 3822 (1996)

[Ueda96] K. Ueda and H. Kontani, *Phys. Rev. Lett.* **76**, 1932 (1996)

[Uemu85] Y. J. Uemura, T. Yamazaki, D. R. Harshman, M. Senba and E. J. Ansaldo, *Phys. Rev. B* **31**, 546 (1985)

[Weih97] Z. Weihong, M. P. Gelfand, R. R. P. Singh, J. Oitmaa and C. J. Hamer, *Phys. Rev. B* **55**, 11377 (1997)

[Weih98] Z. Weihong, J. Oitmaa and C. J. Hamer, *Phys. Rev. B* **58**, 14147 (1998)

[Whit96] S. R. White, *Phys. Rev. Lett.* **77**, 3633 (1996)

Chapter 6

[Aoua97] A. Aouadi, M. J. Lebon, C. Dreyfus, B. Strube, W. Steffen, A. Patkowski and R. M. Pick, *J. Phys.: Condens. Matter* **9**, 3803 (1997)

[Bähr93] M. Bähr, F. Schreier, J. Wosnitza, H. V. Löhneysen, Cager Zhu, Xiaokui Qin, Hong Chen, Xiao Liu and Xiang Wu, *Europhys. Lett.* **22**, 443 (1993)

[Bart97] J. Bartŏs, P. Bandžuch, O. Šauša, K. Krištiaková J. Krištiak, T. Kanaya and W. Jenninger, *Macromolecules* **30**, 6906 (1997)

[Brew94] J. H. Brewer, *Encyclopedia of Applied Physics* **11**, pp. 23-53, New York (1994)

[Buch95] U. Buchenau, *Phil. Mag. B* **71**, 793 (1995)

[Cohe59] M. H. Cohen and D. Turnbull, *J. Chem. Phys.* **31**, 1164 (1959)

[Deje89] R. Dejean de la Batie, F. Lauprêtre and L. Monnerie, *Macromolecules* **22**, 122 (1989)

[Ferr80] J. D. Ferry, *Viscoelastic Properties of Polymers*, 3rd edition, New York (1980)

[Flem97] D. G. Fleming, D. J. Arseneau, J. (Jun) Pan, M. Y. Shelley, M. Senba and P. W. Percival, *Appl. Magn. Reson.* **13**, 181 (1997)

[Free86] J. J. Freeman, J. X. Mack and A. C. Anderson in *Phonon Scattering in Condensed Matter V*, A. C. Anderson and J. P. Wolfe (Eds.), Berlin (1986)

[Gedd95] U. W. Gedde, *Polymer Physics*, London (1995)

[Haye95] W. Hayes, *Phil. Trans. Roy. Soc. Lond. A* **350**, 249 (1995)

[Hemi86] M. Heming, E. Roduner, B. D. Patterson, W. Odermatt, J. Schneider, H. Maumeler and H. Keller, *Chem. Phys. Lett.* **128**, 100 (1986)

[Jest97] Th. Jestädt, D. S. Sivia and S. F. J. Cox, *Hyp. Int.* **106**, 45 (1997)

[Ishi85] K. Ishida, K. Nagamine, T. Matsuzaki, Y. Kuno, T. Yamazaki, E. Torikai, H. Shirakawa and J. H. Brewer, *Phys. Rev. Lett.* **55**, 2009 (1985)

[Kana91] T. Kanaya, K. Kaji and K. Inoue, *Macromolecules* **24**, 1826 (1991)

[Kana92] T. Kanaya, T. Kawaguchi and K. Kaji, *Physica B* **182**, 403 (1992)

[Kief86] R. F. Kiefl, *Hyp. Int.* **32**, 707 (1986)

[Löhn86] H. V. Löhneysen, E. Ratai and U. Buchenau in *Phonon Scattering in Condensed Matter V*, A. C. Anderson and J. P. Wolfe (Eds.), Berlin (1986)

[Morg71] R. J. Morgan, L. E. Nielsen and R. Buchdahl, *J. Appl. Phys.* **42**, 4653 (1971)

[Naga84] K. Nagamine, K. Ishida, T. Matsuzaki, K. Nishiyama, Y. Kuno and T. Yamazaki, *Phys. Rev. Lett.* **53**, 1763 (1984)

[Phil81] W. A. Phillips (Ed.), *Amorphous Solids: Low Temperature Properties*, Berlin (1981)

[Pratt93] F. L. Pratt, W. Hayes, G. R. Mitchell, B. Rossi, M. S. Kiani, B. D. Malhotra, S. S. Pandey, A. Milton and A. P. Monkman, *Synth. Met.* **55**, 677 (1993)

[Prat97a] F. L. Pratt, *Phil. Mag.* **75**, 371 (1997)

[Prat97b] F. L. Pratt, K. Ishida, K. Nagamine, P. A. Pattenden, Th. Jestädt, K. H. Chow, S. J. Blundell, W. Hayes and A. P. Monkman, *Synth. Met.* **84**, 943 (1997)

[Prat97c] F. L. Pratt, S. J. Blundell, W. Hayes, K. Nagamine, K. Ishida and A. P. Monkman, *Phys. Rev. Lett.* **79**, 2855 (1997)

[Prat99] F. L. Pratt, B. W. Lovett, S. J. Blundell, K. Nagamine, K. Ishida, W. Hayes, Th. Jestädt and A. P. Monkman, *Anisotropic polaron motion in conducting polymers studied by muon spin relaxation*, to be published in *Synth. Met.* (1999)

[Reid90a] I. D. Reid and E. Roduner, *Hyp. Int.* **65**, 891 (1990)

[Reid90b] I. D. Reid, T. Azuma and E. Roduner, *Nature* **345**, 328 (1990)

[Rich88a] D. Richter and T. Springer (Eds.), *Polymer Motion in Dense Systems*, Berlin (1988)

[Rich88b] D. Richter, B. Frick and B. Farago, *Phys. Rev. Lett.* **61**, 2465 (1988)

[Rich92] D. Richter, R. Zorn, B. Farago, B. Frick and L. J. Fetters, *Phys. Rev. Lett.* **68** 71 (1992)

[Risc92] R. Risch and K. W. Kehr, *Phys. Rev. B* **46**, 5246 (1992)

[Rodu81] E. Roduner and H. Fischer, *Chem. Phys.* **54**, 261 (1981)

[Rodu82] E. Roduner, W. Strub, P. Burkhard, J. Hochmann, P. W. Percival and H. Fischer, *Chem. Phys.* **67**, 275 (1982)

[Rodu93] E. Roduner, *Chem. Soc. Rev.* **32**, 337 (1993)

[Rodu97] E. Roduner, *Appl. Magn. Reson.* **13**, 1 (1997)

[Vall96] Renela Valladares, *Computational and experimental studies of organic systems*, D. Phil. Thesis, Oxford University (4^{th} of July 1996)

[Treg96] P. L. W. Tregenna-Piggott, E. Roduner and S. Santos, *Chem. Phys.* **203**, 317 (1996)

[Ye97] J. Y. Ye, T. Hattori, H. Nakatsuka, Y. Maruyama and M. Ishikawa, *Phys. Rev. B* **56**, 5286 (1997)

End

[Bibl611] Jeremiah [51,63], King James Bible (1611)

List of Publications

- Muon-spin rotation studies of magnetic order in heavily doped $La_{2-x}Sr_xNiO_{4+\delta}$, K. H. Chow, P. A. Pattenden, S. J. Blundell, W. Hayes, F. L. Pratt, Th. Jestädt, M. A. Green, J. E. Millburn, M. J. Rosseinsky, B. Hitti, S. R. Dunsiger, R. F. Kiefl, C. Chen and A. J. S. Chowdhury, *Phys. Rev. B* **53**, 14725 (1996)

- Magnetic properties of DCNQI salts studied using μSR, F. L. Pratt, P. A. Pattenden, S. J. Blundell, K. H. Chow, Th. Jestädt, W. Hayes, R. Kato, M. Tamura, H. Sawa and Y. Kashimura, *Synth. Met.* **85**, 1747 (1997)

- Muon studies of spin dynamics in polyaniline, F. L. Pratt, K. Ishida, K. Nagamine, P. A. Pattenden, Th. Jestädt, K. H. Chow, S. J. Blundell, W. Hayes and A. P. Monkman, *Synth. Met.* **84**, 943 (1997)

- Magnetoconductance of 60% PANI-CSA films, K. H. Chow, Th. Jestädt, P. J. Gee, S. J. Blundell, J. Singleton, W. Hayes and A. P. Monkman, *Synth. Met.* **84**, 817 (1997)

- Spin dynamics in the organic spin-Peierls system $MEM(TCNQ)_2$ studied using muon-spin relaxation, S. J. Blundell, F. L. Pratt, P. A. Pattenden, M. Kurmoo, K. H. Chow, Th. Jestädt and W. Hayes, *J. Phys.: Condens. Matter* **9**, L119 (1997)

- Probing magnetic order in heavily doped $La_{2-x}Sr_xNiO_{4+\delta}$ with muon spin relaxation, K. H. Chow, Th. Jestädt, S. J. Blundell, S. R. Dunsiger, W. Hayes, B. Hitti, M. A. Green, R. F. Kiefl, J. E. Millburn, P. A. Pattenden, F. L. Pratt and M. J. Rosseinsky, *Hyp. Int.* **104**, 55 (1997)

- Zero-field μSR and QLCR in the molecular metal system $(DMe\text{-}DCNQI)_2Cu$, F. L. Pratt, P. A. Pattenden, S. J. Blundell, Th. Jestädt, K. H. Chow, W. Hayes, R. Kato, M. Tamura, H. Sawa and S. Aonuma, *Hyp. Int.* **104**, 357 (1997)

- Muon spin relaxation by electronic excitations moving in one dimension, Th. Jestädt, D. S. Sivia and S. F. J. Cox, *Hyp. Int.* **106**, 45 (1997)

- Spin dynamics in the spin-gap system CaV_4O_9 studied using muon-spin relaxation, Th. Jestädt, R. I. Bewley, S. J. Blundell, W. Hayes, B. W. Lovett, F. L. Pratt and R. C. C. Ward, *J. Phys.: Condens. Matter* **10**, L259 (1998)

- Physical Properties of the n=3 Ruddlesden-Popper compound $Ca_4Mn_3O_{10}$, A. I. Mihut, L. E. Spring, R. I. Bewley, S. J. Blundell, W. Hayes, Th. Jestädt, B. W. Lovett, R. McDonald, F. L. Pratt and J. Singleton, *J. Phys.: Condens. Matter* **10**, L727 (1998)

- Temperature and doping level dependence of Magnetic order in $La_{2-x}Sr_xNiO_{4+\delta}$ studied by μSR, Th. Jestädt, K. H. Chow, S. J. Blundell, W. Hayes, F. L. Pratt, B. W. Lovett, M. A. Green, J. E. Millburn and M. J. Rosseinsky, *Phys. Rev. B* **59**, 3775 (1999)

- Layered transition metal molecular magnets studied with implanted muons, Th. Jestädt, M. Kurmoo, S. J. Blundell, B. W. Lovett, F. L. Pratt and W. Hayes, to appear in *Synth. Met.*

- Anisotropic polaron motion in conducting polymers studied by muon spin relaxation, F. L. Pratt, S. J. Blundell, B. W. Lovett, K. Nagamine, K. Ishida, W. Hayes, Th. Jestädt and A. P. Monkman, to appear in *Synth. Met.*

- Muon Study of the Spin Dynamics in the Organic Spin-Peierls Compound $MEM(TCNQ)_2$, B. W. Lovett, S. J. Blundell, Th. Jestädt, F. L. Pratt, M. Kurmoo, S. Tagaki and W. Hayes, to appear in *Synth. Met.*

- Stability of the vortex lattice in ET superconductors studied by μSR, S. J. Blundell, S. L. Lee, F. L. Pratt, C. M. Aegerter, Th. Jestädt, B. W. Lovett, C. Ager, T. Sasaki, V. N. Laukhin, E. M. Forgan and W. Hayes, to appear in *Synth. Met.*

- Aminoxyl Radicals and their Complexes, T. Sugano, S. J. Blundell, F. L. Pratt, Th. Jestädt, B. W. Lovett, W. Hayes and P. Day, to appear in *Mol. Cryst. Liq. Cryst.*

- Spin fluctuations in the spin-Peierls compound $MEM(TCNQ)_2$ studied using μSR, B. W. Lovett, S. J. Blundell, F. L. Pratt, Th. Jestädt, W. Hayes, S. Tagaki and M. Kurmoo, submitted to *Phys. Rev. B*

- μSR studies of magnetic order and dynamics of the n = 2 Ruddlesden-Popper phases $Sr_2LnMn_2O_7$, where Ln = Pr, Nd, Sm, Eu, Gd, Tb, Dy and Ho, R. Bewley, S. J. Blundell, B. I. Lovett, Th. Jestädt, F. L. Pratt, K. H. Chow, W. Hayes, P. D. Battle, M. A. Green, J. E. Millburn, M. J. Rosseinsky, L. E. Spring and J. F. Vente, submitted to *Phys. Rev. B*

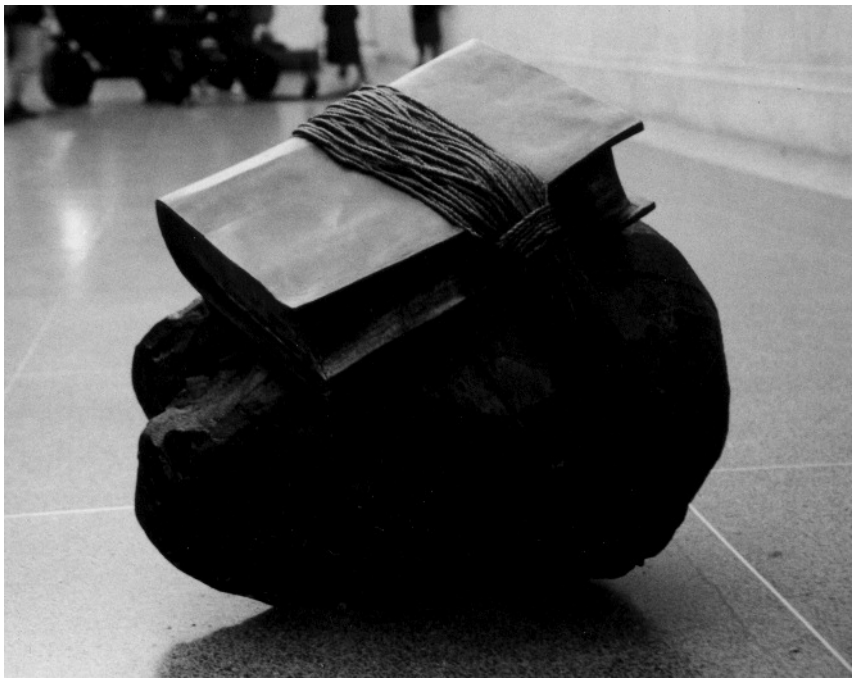

"And it shall be, when thou hast made an end of reading this book, that thou shalt bind a stone to it, and cast it into the midst of Euphrates" [Bibl611]

Index